NUMERICAL AND EXPERIMENTAL ANALYSIS

OF STRESS BEHAVIOR OF

PLASMA-SPRAYED BIOGLASS® ON TITANIUM

Hyuen Me (Mia) Park
B.S., University of Florida, 1994

A thesis presented to the faculty of the
Oregon Graduate Institute of Science & Technology
in partial fulfillment of the
requirements for the degree
Master of Science
in
Materials Science and Engineering

October 1996

The thesis "Finite Element Analysis of Stress Behavior of Plasma-Sprayed Bioglass® on Titanium" by Mia Park has been examined and approved by the following Examination Committee:

Lemmy Meekisho, PhD
Associate Professor
Thesis Research Advisor
Oregon Graduate Institute

David Atteridge, PhD
Professor
Oregon Graduate Institute

Milt Scholl, PhD
Assistant Professor
Oregon Graduate Institute

Donna Wheeler, PhD
Assistant Professor
Oregon Health Sciences University
Division of Orthopaedics

DEDICATION

To my soul mate and partner for life, Sean Caraway, and my dear family who have been behind me for the entire "ride".

ACKNOWLEDGMENTS

I would like to thank Donna Wheeler, PhD for providing me with the opportunity of working on this study. Without Donna, I would never have made it to the Oregon Graduate Institute. Special thanks go out to Lemmy Meekisho, PhD for the endless amounts of support, encouragement, and guidance. The Finite Element Analysis was only possible with his patience and teachings. I must also extend a special thanks to Kevin Searles who sacrificed hours of his time to help and teach me the workings of the Instron and mechanical test specimen preparation. My regards to John Anderton for guiding me through the ultrasonic testing. David Christilaw also donated much of his busy time to educate me on the SEM machine as well as the specimen preparation...thank you. Thank you Vivek Dikshit for your advise on statistics, sample preparation, and life in general. Various other OGI members were also a great help in this study: Andy Villenuve, Kristen Terry, Nong Jin, Youping Gao, Hui Su, Leo Chen, Wen Wei, and Jun Ding.

Thanks to the strong support from David Atteridge,Ph D and Bill Wood, PhD my funding was re-established long enough for me to finish my thesis. Much appreciation goes out to Vivek Dixit, PhD, Milt Scholl, PhD, and Jack McCarthy, PhD who were willing to the take time to provide me with advice about this study.

I must credit those who supplied me with the necessities: Roxanne Metzger for supplies, Rolf Klein of Thortex for manufacturing test specimens, David Greenspan, PhD and Guy LaTorre of USBiomaterials for their participation in providing Bioglass® and advice.

Contents

List of Tables

List of Figures

Abstract

Numerical and Experimental Analysis of Stress Behavior of Plasma-Sprayed Bioglass® on Titanium

Hyuen Me (Mia) Park

Oregon Graduate Institute of Science & Technology, 1996

Supervising Professor: Lemmy Meekisho, PhD

Due to the constantly growing number of total joint arthroplasty patients, the demand for improvements in the design of implant fixation has become more apparent. One method of implant fixation involves the use of a porous metal prosthetic that has been coated with a bioactive ceramic such as Bioglass®. This ceramic coating acts to initiate early bone infiltration into the porous surface provided by the implant. Once osseointegration has occurred, the implant is securely fixed within the host bone of the patient.

Analysis of the integrity of the plasma-sprayed bioceramic on a titanium alloy (Ti-6Al-4V) was the focus of this study. Both numerical and experimental components were used to investigate the bond strength of Bioglass®-coatings on Ti-6Al-4V.

The physical specimen consisted of a Ti-6Al-4V cylinder which was plasma-sprayed with Bioglass® (BG) on one of its flat surfaces. This BG surface was adhered to another Co-Cr-Mo mushroom cap with an epoxy adhesive. The titanium alloy cylinder was 25.4mm in diameter and 12.7mm in length. A 150μm thick coating was applied onto the flat surface of the titanium cylinder. The test samples were pulled in tension at a rate of 0.1in/min until complete failure occurred.

Finite element analysis (FEA), being a widely accepted method of analyzing or

simulating a variety of engineering stress, strain, and failure problems, was used in this study. Specifically, two-dimensional (2D) and three-dimensional (3D) FEA models were developed to evaluate the stress/strain distributions at a bimaterial interface of a tensile test specimen.

Dimensions of the FEA models (Ansys5.2 [1]) were identical to those of the experimental specimens. The heights of the Ti-6Al-4V pieces, however, were reduced strategically to minimize the overall problem size in order to focus on detail analysis of the domain in the neighborhood of the interface. Elements capable of linear strain were used in the models. A linear-elastic solution was chosen with the knowledge that BG does not exhibit plastic deformation. The material properties of interest were Young's modulus (E) and Poisson's ratio (υ) [2-9]. Necessary and sufficient boundary conditions were applied in the FEA model so as to accurately represent the physical problem. Specifically, the boundary conditions would simulate appropriate lateral shrinkage of the specimen as it elongates under the action of the applied tensile load. The tensile load was applied as a uniform tensile pressure. While various pressure loads were applied, only results obtained from a pressure level of 30MPa will be presented. This is for purposes of consistency with data reported in the literature.

The tensile tests showed that weaker bond strengths exist with the porous specimens. Bond strengths for both porous and smooth samples were inversely proportional to the BG coating. The maximum bond strength was observed with the smooth coupon group having the lowest BG thickness.

The FEA models yielded a singular stress field at the free-edge interface corners of the bimaterial. These high stresses suggest that the corners could be the location of failure initiation. That the singular stress fields were found to be at the free edge interface corners was consistent with expectation. The equivalent von Mises stress was used in assessing the stress-strain response of the specimen since it gives an overall more realistic picture of the state of deformation [10]. The von Mises stresses for the FEA study revealed slightly higher stresses along the interface in comparison to the rest of the model. In addition, the equivalent stresses resulted in having 45° "wings" of high stresses which protrude from the free edge into the titanium blocks. These high stress wings were oriented along the slip directions for metal [10, 11] subjected to a tensile load.

The highest strains appeared in the center region of the BG layer which was expected since BG has the lower value of Young's modulus. The deformation fields observed were in accordance with expectations, namely the longitudinal elongation and lateral shrinkage of the specimen.

Chern Lin et al [6] performed a similar study where plasma-sprayed BG coatings were subjected to tension for delamination. Fractures were observed to occur within the coatings and only some of the coating was separated from the substrate while the majority still remained tightly bonded to the substrate. Since most of the failures occurred within the coatings themselves, the actual bond strengths should be higher than those measured.

The von Mises stresses show that failure would occur initially at the free-edge interface and propagate along the Ti-6Al-4V/BG interface. This differs from the experimental observations in that the BG did not completely delaminate from the

substrate. Many areas on the substrate surface were still covered by BG. The FEA evaluation was made on the assumptions that the materials were isotropic, homogeneous, and free of microvoids. The 45° stress zones are generally observed in metals due to their ductility and corresponding slip system characteristics. These oblique stress zones may be interpreted as resolved shear stresses which developed during the lateral contraction of the specimen experienced under tensile loading [11].

CHAPTER 1

INTRODUCTION

The hip joint is of a ball-and-socket configuration which allows for the most freedom of motion. Figure 1.1 shows the anatomy of the hip joint [12-15]. The acetabulum serves as the "socket" which houses the femoral head ("ball"). Hyaline cartilage line both the acetabulum and the femoral head. During motion, synovial fluid is released for adequate lubrication between the articular surfaces. The hip joint, in particular, bears enormous loads, up to eight times ones body weight, during everyday activities such as walking and running [2, 16, 17].

Prolonged disease, ie. osteoarthritis, osteoporosis, and rheumatoid arthritis, may lead to irrecoverable damage to the joints. In fact, the literature cites that 16 million people in the United States are inflicted with osteoarthritis, which causes joint degeneration at the hyaline cartilage which then alters the stress distribution across the articular surfaces, and therefore, further depletion of the cartilage occurs [16]. This causes the rubbing of bone on bone which causes pain and discomfort for the patient. A typical solution to this painful situation is to substitute the acetabulum and femoral head with a total hip arthroplasty (THA) (Figure 1.2).

Annually, two to three million people in the United States alone undergo surgery for the implantation of prosthetics [18]. The THA has an overall success rate of about 90% over a period of ten years in elderly patients. Unfortunately, patients in the range of

16 to 24 years of age, who are generally more active, usually require a second operation for revision within three years of the initial surgery [12]. Although less than 50% of youths require THA, methods to improve the longevity of the implant is constantly pursued. John Charnley [2, 3, 16, 20] developed the "bone cement" (polymethlymethacrylate-PMMA) which served as a grouting material between implant and bone to create a tight and sturdy fit for the prosthetic. This viscoelastic polymer functioned well as a shock absorber and permitted loads to be uniformly transmitted between the implant and bone which in turn reduced high-contact stress [16]. PMMA provided initial fixation, however over time, cracks occurred between the implant-cement-bone interface which caused the loosening of the implant, thus, revision surgery was usually required [2, 16, 17, 21].

The THA underwent design modifications to improve the long term fixation. For instance, biological fixation techniques included rough, meshed, or porous implant surfaces. These types of porosity were accomplished by means of plasma-spray, sintering of wire, and sintering of beads, respectively (Figure 1.3) [16, 22]. The application of the porous coating on Ti-6Al-4V decreases the cyclic fatigue strength of uncoated Ti-6Al-4V by 66% [23]. Dziedzic et al [24] investigated a bone chamber implant that provided a porous surface along its inner walls for osteoconduction. The objective of the nonuniform implant surface was to allow for new bony ingrowth into the crevices provided by the implant and as a result creating a strong fixation. This biological fixation method appeared to be promising, however, the patients experienced pain that may have been due to the high hoop stresses that resulted from the tight fit of the implant when pressed into the cavity of the femur [2, 25-32].

In addition to biological fixation, chemical fixation has been implemented into the design process of the metal implants. The porous surface of the implant is coated with a bioceramic such as hydroxyapatite (HA), which is similar in content to that of bone mineral [2, 33]. This ceramic coating aids or stimulates the initiation of bony ingrowth into the pores of the implant. Keller states that studies show that HA-coated implants work well initially, however, diminishes after three weeks in a canine femur (Figure 1.4)

[2]. The use of ceramic coatings on implant material appears to have potential, yet much improvement in the composition and coating technique must be established to provide optimum implant fixation.

During recent studies, other bioceramics have entered the realm of chemical fixation of metal implants. The term "bioactivity" refers to the surface-reactivity of an implant in forming strong bonds with host tissue. A bioactive ceramic known as Bioglass® was discovered by Hench [34-36] during the late sixties. Strong adherence between a bioactive coating and its substrate has been a crucial issue in the effectiveness of an implant to be optimally suitable for osteoconduction. Bioactive coatings have been noted to form bonds with living tissues, thus, creating a firmly fixed implant [35]. If the BG coating delaminates prematurely from the implant, the necessary duration over which initial tissue bonding may occur is reduced and can result in fixation failure [37]. Early delamination of bioactive ceramics can be attributed to poor coating techniques that lead to microcracks within the coating or along the ceramometallic interface. These microcracks may occur due to the high cooling rate associated with the plasma-spraying technique [6, 20]. Eliminating delamination of the ceramic coatings could improve osteoconduction and increase the longevity of the implant.

Mechanical tests have been devised in several modes to explore the bond strength of ceramic and porous coatings on substrates. Pull-out, shear, lap shear, torsion, tensile, and three-point flexure tests have been conducted previously and yielded varying ceramic-on-metal bond strengths depending on the mode of testing [6, 23, 38-41]. The bond strength of BG is often compared with that of Hydroxyapatite (HA). BG may generate higher levels of bioactivity than HA but yields a weaker bond strength when plasma-sprayed to a substrate [6]. Fracture mechanics have also played a role in the investigation of coating-substrate bond strength. The dental industry commonly performs fracture toughness measurements of adhesives to determine the interfacial bond strength. Crack initiation and propagation energies are not easily differentiated as such, the J integral which is measured experimentally is then compared with the theoretical stress intensity factor, K_{IC} [42-45].

The mechanical tests are typically followed by calculations to determine primary and secondary parameters that are pertinent to the mechanical tests. Such results are then generally used as input data for more detailed analyses of behavior and response to loads in Finite Element Methods (FEM). Stress distribution analyses have been conducted on the ceramometallic three-point flexure specimens [40]. Studying the resulting stresses along a bimaterial interface may reveal the site(s) of crack initiation and the manner in which the crack propagates to complete failure of the interface. Failure predictions of porous-coated total hip replacements have also been studied with the use of FEA [46]. Two-dimensional modeling of the tensile failure at a bimaterial interface was accomplished with nonlinear fracture mechanics [47]. FEA offers a controlled environmental setup in which to run simulations of experimental tests. Once a test has been successfully completed, with its results representative of an experimental setup, confidence to introduce complexities of loading and geometry can be sought. This thus offers a powerful analytical research tool for simulating a wide variety of geometries and loads that would otherwise be difficult, even impossible, to establish experimentally and/or in closed form analysis.

The objective of this study was to investigate the viability of predicting, numerically, the bond strength of a plasma-sprayed bioactive ceramic on a titanium substrate. The properties of the materials of interest was determined experimentally and used as input data for the finite element analysis. The numerical results will be compared with experimental results. Optical and Scanning Electron Microscopy was used to study the failure surface morphologies. The aim of this was to establish the qualitative features of the bonding of BG on Ti-6Al-4V. Failure surface characteristics eg. presence of shear lips or indication of the extent of brittle failure of the interface was established. This aspect of the study was also help in establishing the possible occurrence of spontaneous surface delamination of the interface, given the significant difference in material properties across the interface.

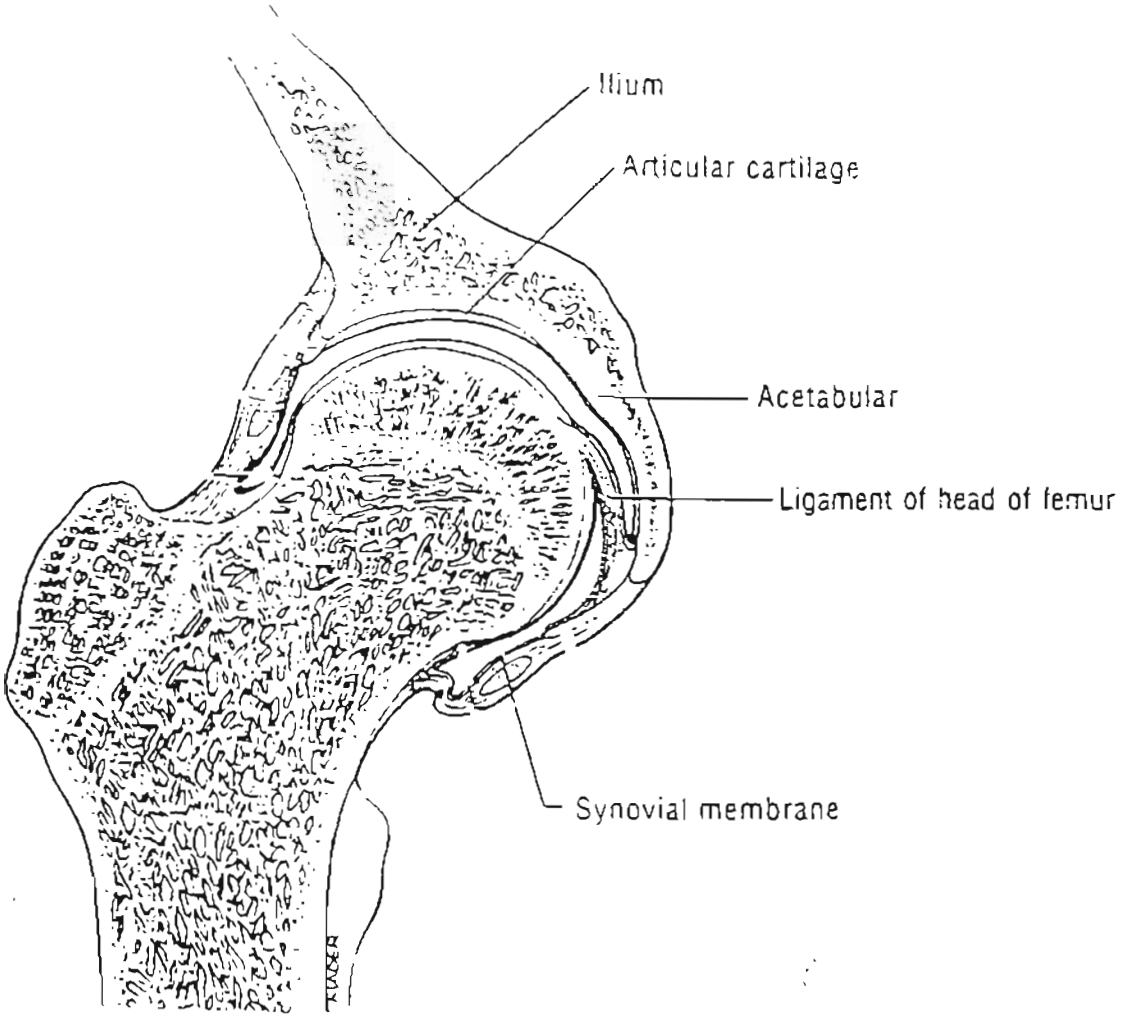

Figure 1.1 Cross-sectional view of the hip joint. [12]

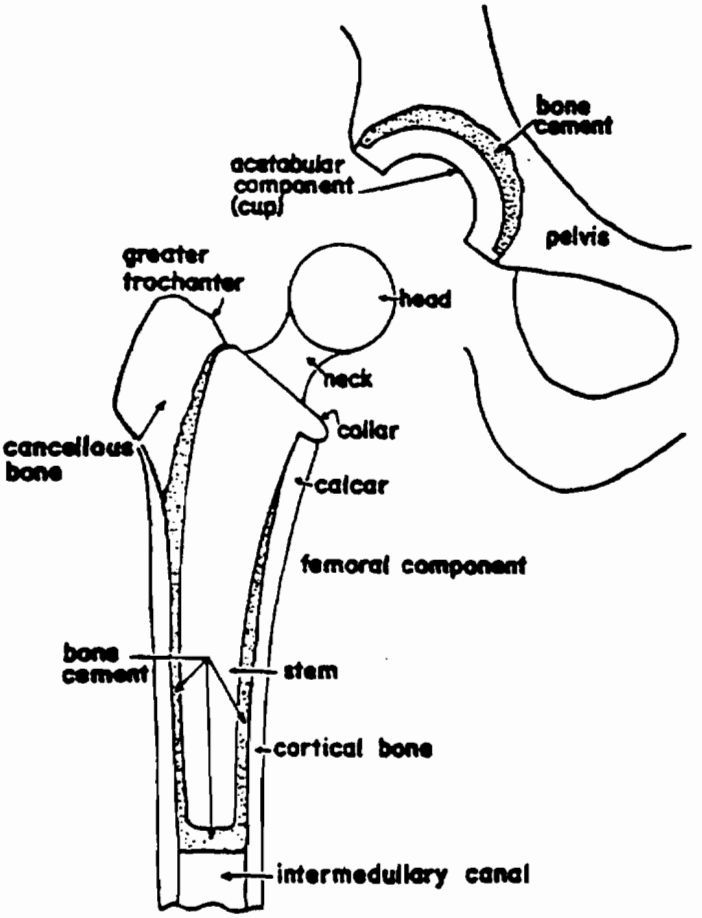

Figure 1.2 Schematic of the total hip replacement. [116]

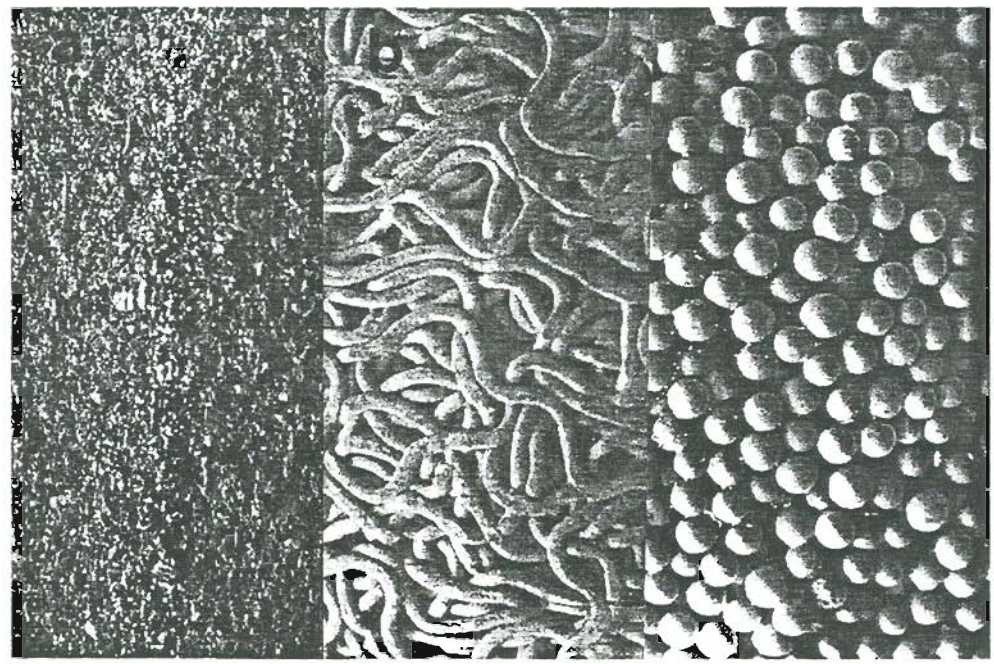

Figure 1.3 Scanning electron micrographs of (a) plasma-sprayed, (b) sintered wire, and (c) sintered beads. [16]

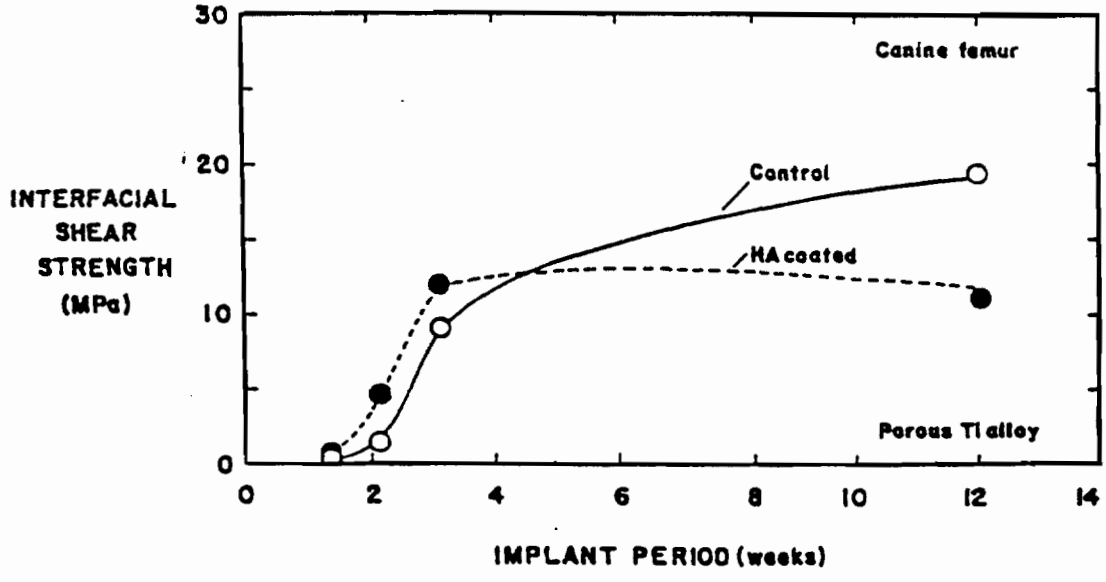

Figure 1.4 Interfacial shear strength between bone and HA-coated porous implant and between bone and uncoated porous implant when implanted into the cortices of canine femora. [2]

CHAPTER 2

BACKGROUND

2.1 Bone

Bone is a highly active material of living tissue with many components. Living hard tissue is constantly remodeling with the aid of a family of bone cells. Osteoblast cells continually deposit new bone while osteoclast cells absorb bone. There are two main purposes for bone remodelling: 1) Maintenance of Ca^{2+} and PO_4^{3-} concentrations in the body fluid and 2) Response to the changes in compressive mechanical stress [12, 16, 48]. A mature bone cell is referred to as an osteocyte. Figure 2.1 shows the structure of bone with its osteocyte. Also shown, is the cortical bone which forms the outer hard shell of bone. Cortical bone consists of an outer lamellar shell with a Haversian system inside of the lamellae. Inside of the cortical bone exists a spongy bone known as trabecular or cancellous bone.

The long bones found in the limbs consist of a general structure involving a shaft and two extremities. The long shaft of the bone is called the diaphysis. The inner hollow core of the diaphysis is referred to the medullary canal. The epiphyses are the regions at the end of the bone (Figure 2.2). The epiphyses have more spongy bone than the shaft and are covered with a thin layer of cortical bone. The epiphyses are broader in geometry for purposes of articulation. The epiphyses are lined with cartilage for articulation at the joints. In adults, an epiphyseal line, which is the remnant of the epiphyseal plate, exists

between the epiphysis and diaphysis. This
epiphyseal plate is actually a disk of hyaline cartilage that provides growth to lengthen the bone during childhood.

2.2 Total Hip Arthroplasty

Bone grafts have been conducted with bone from another region of the patient's body (autograft), from another patient (allograft), from another species (xenograft), or with synthetic material. The most successful method remains to be the autograft, however, there are limitations to the supply of one's own tissues before morbidity occurs within the donor site. Infection risks create a problematic scenario for the allograft method. The question of biocompatiblity with xenografts gives rise to difficult scientific situations. Synthetic materials provide a viable option for safe and successful soft and hard tissue repair/replacement.

A prime example of synthetic-material implants is the total hip arthroplasty (THA) (Figure 1.2). The role of a THA is to restore an adequate range of motion at the hip joint while transferring loads from the acetabulum [49]. This implant was designed to resemble the configuration of the femur and acetabulum. The femoral segment substitutes the head and neck of the proximal femur with its stem extending into the intramedullary canal of the diaphysis. The acetabulum is replaced with a synthetic-material acetabular cup. This cup receives a synthetic-material femoral head to maintain the ball-and-socket form.

Some of the metals that were explored by Baron Joseph Lister, in the 1860's, for the use of joint prosthetics include platinum, gold, silver, lead, zinc, aluminum, copper, and magnesium. These metals, however, were found to be excessively malleable. Further experimentation led to the introduction of stainless steels in 1926, cobalt-chromium-molybdenum-carbon alloys in 1936, then tantalum in the 1950's, and finally to titanium and titanium alloys during the 1960's [3, 16]. The titanium alloy, Ti-6Al-4V, was chosen for this study based on several factors. First, a study performed by Hirschhorn and Reynolds [3], revealed that a porous cobalt-chromium-molybdenum implant had an elastic modulus closer to that of bone, but porosity diminished the strength enough that it was incapable

of supporting the needed load. A mechanical and histological study using macrotextured Co-Cr alloy with plasma-sprayed HA proved to be ineffective for biological fixation [38]. Titanium is as strong as steel and yet is almost 50% lighter [3]. Due to its high strength-to-weight ratio, titanium and its alloys were very appealing to the aerospace industry which would also attract the medical industry for obvious reasons. The stiffness of titanium closely resembles that of bone which could be beneficial with regard to movement and loading (Figure 2.3). Previous studies have used Ti-6Al-4V specimens for multiaxial fatigue testing to develop a measure for making conservative predictions of the life expectancy of a Ti-6Al-4V implant [50, 51]. Titanium or titanium alloys are highly resistant to corrosion [3]. Easy fabrication of titanium also plays an important role in its choice as a suitable implant material.

Choosing the appropriate metal to serve as a THA is crucial not only for biocompatibility but also for prevention of stress shielding. This problem of stress shielding occurs when the stiffness or modulus of elasticity is much higher than that of the bone. Stress shielding prevents proper loading of the bone, thus leading to bone resorption [49, 52]. Table 2.1 shows the modulus of elasticity and yield strength for various metals in addition to properties of bone.

For many years now, studies have been conducted to improve materials used as bone substitutes. This study employs a titanium alloy (specifically Ti-6Al-4V) which was not introduced into the medical field until the 1960's [3]. When using a smoothly polished implant, a bone cement (polymethlymethacrylate-PMMA) must be used to create a tight and sturdy fit within the bone, however, the use of bone cement proved to be less than optimum. This PMMA grouting agent provided initial fixation. With time, however, cracks appeared in the cement mantle which eventually led to the loosening of the implant. In addition, the release of a monomer caused hypotension and the exothermic polymerization reaction caused necrosis of the surrounding bone [16, 35]. In order to exclude this bone cement, other means of designing tight-fitting implants were investigated. These studies resulted in the development of porous implants which have beads of the same metal sintered onto the surface of the substrate. By doing so, the

implant now has a porous surface which the bone is expected to grow into. Often these metal implants are coated with a surface-active ceramic to enhance bone ingrowth.

After the failure of the PMMA bone cement, the method of sintering metal beads, microns in diameter, was used to provide a porous surface in which tissue can grow into and still maintain adequate blood supply. Titanium and cobalt-chromium alloys are a few of the metals that demonstrate adequate corrosion resistance to be used as porous implants [18]. Previous studies suggested that soft connective tissue is capable of growing into pores of diameters greater than 50μm. It has also been established that bone will grow into pores of more than 100μm in diameter [16, 31]. A serious question remains unanswered regarding bone maturing into mineralized tissue when subjected to micromovements that are inevitable with load-bearing implants. These movements can transfer stress to the bone resulting in bone resorption [16, 18].

2.3 Ceramics/Glasses

By definition, ceramics are nonmetallic minerals that are typically produced by baking or firing powdered materials pressed or formed into solid forms. A glass is a hard, amorphous, brittle, and inorganic material which is made by fusing silicates with particular basic oxides and then cooled rapidly to prohibit crystallization. Borates and phosphates are sometimes used in place of silicates [53]. Due to the significant differences between ceramics and traditional metallic materials, methods for characterizing the behavior of ceramics are unique and summarized as follows.

2.3.1 Crystal Structure

The thermal conductivity of ceramics is governed by the nature of their crystalline structure. Ceramics with a close-packed structure accompanied by a low bulk density exhibit high thermal conductivities. Crystalline ceramics, typically, possess higher conductivities than the glassy-amorphous ceramics because of less scattering of phonons associated with this. As well, thermal conductivity decreases with increasing porosity.

Crystalline silica (SiO_2) is formed by four covalent bonds on the silicon atom with four oxygen atoms. This creates a tetrahedral structure that serves as the fundamental building block in which other complex silicate structures are composed of. Any ionic bonds that occur in ceramics must have the ionic charges balanced throughout. When the charges of the anion and cation are equal, the coordination number for each ion is the same in order to maintain the balance of charges. If the cation had a charge of +1 whereas the anion had a charge of -2, then the coordination number of the anion must be twice that of the cation for a balance of charges [11].

The coordination number is also dependent upon the ratio of the ionic radii of the anion and the cation. The radius of the central ion can be equal to or slightly larger than that of the space in which it lies, pushing the neighboring ions apart. The interstitial spaces are occupied by the proper number of cations and anions to maintain a balance of charges or to satisfy the requirements for covalent bonding. Interstitial atoms with a coordination number of eight fit into simple cubic structures, however, interstitials with coordination numbers of six in octahedral sites and coordination numbers of four in tetrahedral sites occur in other unit cells [11].

Imperfections such as point defects and surface defects may occur in ceramic materials. Point defects include substitutional and interstitial solid solutions. Orthosilicates, $(Mg,Fe)_2SiO_4$, may undergo substitutional solubility where the Mg^{2+} ions take up the positions of the Fe^{2+} ions and vice versa. Interstitial solid solutions are not common due to the fact that the interstitial sites are already occupied. For instances where the balanced charge is disrupted, the ceramic accommodates in several ways. If an Al^{3+} ion is replaced by a Mg^{2+} ion, the clay platelet overcomes its net negative charge by absorbing a positively charged ion, Na^+ or Ca^{2+}, onto its surface. Another remedy for an unbalanced charge is to develop vacancies within the lattice. Finer grain sizes can improve the mechanical behavior of ceramics over coarse grained ceramics. The finer grains aid in the reduction of stresses at the grain boundaries due to anisotropic expansion and contraction [11].

2.3.2 Processing/Forming

Ceramic raw materials must first be mined from the large deposits in the earth's crust by a method referred to as strip-mining or open-pit mining. The deposits are removed using the standard earth-moving equipment or by washing them out hydraulically. For mineral deposits that are far below the earth's surface, vertical shafts are driven into the deposit for drilling or blasting [54].

Upon mining, the raw material is then crushed or ground between plates of hardened steel (Figure 2.4). These "lumps" of material are crushed further into particles about 0.1 inch or less in diameter. Hammers or impact mills are commonly used in this secondary crushing of the hard and brittle material. A tertiary crushing is necessary in cases where a very fine particle size is required, for instance, in the cement industry. This third grinding is carried out in a tumbling mill which consist of large rotating cylinders filled with a dense ceramic grinding media. The resulting particle may be 50μm or less in diameter [54].

The crushed fragments are then separated into the specific particle size range needed by the industry. This task is accomplished with the use of screens which may eliminate coarse or fine particles. The selected particles are purified then mixed with appropriate proportions of various raw materials [54].

After mixing is completed, the raw material is shaped and formed. Unlike metals, ceramics are seldom formed by methods of casting or mechanical working. Instead, hydroplastic forming of solids is a more common procedure for shaping ceramics. Material properties of the ceramics usually dictate the method of forming. Hydroplastic forming can be applied to ceramic raw materials that consist of layered structures since they exist as paste with a low initial shear strength. For products requiring a uniform cross-section, extrusion is the method of choice. Products that require circular geometry undergo the jiggering technique which uses a rotating mold to form one surface of the piece. The other surface is formed with the rotation of the product under a contoured tool [55].

Regulating the yield strength of this paste-like material is important in the forming

process. Yield strength enables the product to maintain its shape during the handling and drying processes. The yield strength can be modified by the water content. Yield strength of ceramics is inversely proportional to the liquid content, thus, higher liquid content lowers the yield strength. Any air pockets that may exist in the paste become compressed under the pressures developed from the forming process. When the pressures are released, however, the voids reopen which results in internal fissures which act as stress raisers. These air pockets must be eliminated by reducing the pressure during extrusion or applying a vacuum in the dry pressing operations. Entrapments of air or other substances create surface blemishes or residual stresses. The residual stresses may be remedied by annealing which is common practice upon the completion of the firing where thermal stresses are induced [55].

Slip-casting allows for complex forms to be created with ceramic raw materials. Slip-casting involves a colloidal suspension which is dehydrated by a porous mold which may contain intricate contours. A shell deposit results and the rest of the slip is drained while the remaining shell is drained further and then removed as a mold. This mold has the consistency of a low-water colloidal paste. Slip-casting is an economical method of forming under limited production requirements and is a preferred operation amongst ceramic artists [55].

Vitreous shaping procedures involve: pressing, drawing, blowing, and sagging. Parameters for vitreous shaping include the selection of the temperature, pressure, and time depending on the composition of the glass. Temperature governs the viscosity of the glass and the pressure controls the rate of deformation [11, 55].

Viscosities of 10^6 to 10^7 Poise are necessary for the pressing operations to take place because external pressure is applied to the glass. The application of pressure comes from a carbon-coated, cast-iron mold of the preferred shape.

Long and continuous shapes of glass, ie. sheet glass, glass tubing, or glass fibers, are created by the drawing the heated material through orifices. A balance must be accomplished between the flow rate through the orifice and the rate of drawing of the viscous glass from the bushing.

Mechanical blowing of glass is achieved with the help of cast iron molds which are filled with a particular amount of semi-viscous glass. Sufficient air pressure is applied to the internal cavity in order to eradicate the surface energies of the glass and allow for flow to occur [11, 55].

Cementation joins ceramic raw materials using a liquid binder, such as sodium silicate, to initiate chemical reactions that join the particles together. Cemented ceramic materials have high porosity and permeability and are therefore, used as ceramic filters or as molds for metal castings. The porous molds allow for the escape of gases during casting to inhibit gas defects that may occur otherwise [11].

2.3.3 Physical Characteristics

During the manufacturing process, ceramics often experience shrinkage. The shape, however, remains intact with minimal warpage. After the product has been formed, the drying procedure begins where the grains are drawn closer to each other until they make contact. The greater the water content, the greater the shrinkage during the drying process. Further shrinkage occurs as the dried product undergoes the firing process which in turn reduces, or even eliminates, the pores. The shrinkage along each dimension is of more concern than the overall volumetric shrinkage. Careful study of both drying and firing shrinkages will reveal the proper amount of oversizing necessary to produce a final product of adequate dimensions [54].

The porosity of a ceramic needs to be carefully controlled due to the potential damage that may occur with excess infiltration of liquids and vapors into the material. For instance, an overly porous brick may suffer damage from freeze-thaw cycles and water penetration. On the contrary, thermal insulators demand high porosity with rigid stipulations on the quantity and size of the pores.

The normally high melting point of ceramics depends on the structure of the phases. A low atomic packing factor yields voids which in turn, decreases the thermal expansion, increasing the melting point. The melting point can usually be predicted by the value of Young's modulus. Large values of Young's modulus normally result in a high

melting temperature [11, 55].

Ceramics are also unique in that six different types of volumes are computed depending on the level of porosity. Pores that may be continuous with the surface are known as open pores (Figure 2.5). The total volume of these open pores is referred to as the open pore volume (V_{op}). Pores that are completely closed off within the body of the material are called closed pores, and have a closed pore volume (V_{cp}). Regions of the ceramic that are free of pores have a volume known as the true volume of the body (V_t). The sum of the closed pore volume and true volume is referred to as the apparent volume (V_a). The bulk volume (V_b) is computed for the solid portions in addition to all of the pores. The following equations depict the relationships between the various volumes found for a ceramic:

$$V_{op}=V_b-V_a \tag{2.1}$$

$$V_b=V_t+V_{op}+V_{cp}=\frac{W_s-W_{ss}}{\rho_L} \tag{2.2}$$

$$V_a=V_t+V_{cp}=V_b-V_{op} \tag{2.4}$$

$$V_t=V_a-V_{cp} \tag{2.3}$$

$$V_{cp}=V_b-V_t-V_{op}=V_a-V_t \tag{2.5}$$

where W_D represents unsaturated or dry weight, W_s is the saturated weight in which all of the pores are filled with water, W_{ss} is the weight of the saturated ceramic while submerged in water, and ρ_L represents the density of the saturated and submerged sample.

Bulk density (ρ_b) is a common parameter reported amongst all ceramics. The computation of ρ_b includes the bulk volume:

$$\rho_b = \frac{W_D}{V_b} = \frac{W_D X \rho_L}{W_s - W_{ss}} \tag{2.6}$$

The apparent density (ρ_a) is also commonly measured for ceramic materials and is calculated as follows:

$$\rho_a = \frac{W_D}{V_a} = \frac{W_D X \rho_L}{W_D - W_{ss}} \tag{2.7}$$

The true density (ρ_t) involves the true volume and can be computed using the equation below:

$$\rho_t = \frac{W_D}{V_t} \tag{2.8}$$

2.3.4 Characteristic Mechanical Behavior

Ceramics, in general, have excellent properties under compressive loading, however, their brittle nature makes them virtually useless for coping with tensile loads. The compression test requires more specimen preparation. Two faces of the sample must be perfectly flat and parallel in order for the compressive load to be distributed evenly otherwise, the ceramic would fail prematurely (Figure 2.6) [54, 56].

Tensile tests are not commonly performed on ceramic materials due to considerable costs of manufacturing the samples. Interests in the tensile strength of ceramics are limited because they are quite weak under tension.

As a whole, ceramics exhibit higher moduli of elasticity than most other materials, typically, 70 to 414 GPa [54, 55]. The most common method of determining Young's modulus is with sonic resonance [54, 57]. The dynamic modulus of elasticity is calculated using the following equation.

$$E=0.9465(mf_f^2/b)(L^3/t^3)T_1 \quad (2.9)$$

Young's modulus is represented by E, m is the mass of the specimen (kg), f_f is equal to the fundamental resonant frequency of the sample in bending (Hz), b is the width, L is the length, t is the thickness, and T_1 is the correction factor for the bending mode which takes into account the finite thickness of the sample and Poisson's ratio [57]. Sonic resonance testing can also be used to determine the relative thermal shock resistance of porous ceramics [54].

The modulus of rupture (MOR) depicts the fracture strength of the ceramic while subjected to a flexural load. The sample may have a rectangular or cylindrical cross-section and placed under a three- or four-point bend apparatus (Figure 2.7). Fracture always occurs on the tensile surface of the specimen. Under a three-point bend, failure must occur in the center of the sample length, whereas, failure can result anywhere between the inner two loading points in a four-point bend [54]. The MOR of a three-point bend for a rectangular specimen can be computed as follows:

$$MOR=3PL/2bd^2 \quad (2.10)$$

where P equals the load at failure, L is the span between the two supports, b is the width of the specimen, and d is the thickness of the bar [54, 55]. For cylindrical specimens under a three-point bend, the MOR is determined by:

$$MOR=8PL/\pi D^3 \quad (2.11)$$

where D is the diameter of the sample. The MOR of a four-point bend, rectangular specimen if given by:

$$MOR=\frac{3P(L-a)}{2bd^2} \quad (2.12)$$

where a is the span of the inner two loading points. The MOR for a cylindrical specimen under four-point bend is calculated by [54]:

$$MOR=\frac{8P(L-a)}{\pi D^3} \tag{2.13}$$

An empirical formula was developed to draw a relationship with the application of specimen cross sections to stress-strain curves from both tension and compression tests. As a result, the MOR was found to be a multiple of the ultimate tensile strength (UTS): ie. MOR = 2*UTS for cast iron, MOR = 3*UTS for sandstone, MOR = 2.2*UTS for concrete, and MOR = 2.3*UTS for green wood [58].

2.4 Bioactive Ceramics

Industries take advantage of the wide variety of applications that ceramics can be utilized. Aside from the obvious applications of ceramics, engineering has adapted these materials for many state-of-the-art purposes. A Ceramic Applications In Turbine Engines (CATE) project was developed to study the possibility of ceramic components enabling a gas turbine engine to operate at higher temperatures [119]. The literature cites studies in which ceramics were used in metal-cutting applications [120]. The phase characteristics of ceramics and their high thermal conductivities at higher temperatures serve important purposes in the electronics technology [121]. On the other hand, at lower temperatures, the energy gap is too large for the electrons to reach the excited conduction band and therefore serve as good insulating materials [11]. Recently, the development of bioactive ceramics has resulted in medical applications for improving the stability of implants.

2.4.1 Biodegradable Ceramics

For a ceramic to be considered a bioceramic, the composition must meet or exceed those in Table 2.2 [56]. Synthetic biodegradable or resorbable ceramics were introduced as bone substitutes in 1969 [56]. The term "resorbable" refers to the degradation of the

ceramic upon implantation in the host. Calcium phosphates such as Biocoral, Plaster of Paris, hydroxyapatite (HA), and tri-calcium phosphate (TCP) have been used in various forms as artificial bone. Calcium phosphate ceramics vary widely in mechanical properties due to their dependence on porosity [59]. HA has excellent biocompatibility and forms direct chemical bonds with hard tissues [17, 56, 60-63]. In fact, HA [$Ca_{10}(PO_4)_6(OH)_2$] has been known to bond with bone within 4-8 weeks of implantation [56, 64]. Geesink et al [17] observed osseointegration as soon as three weeks with plasma-sprayed HA on Ti implants [17]. Osseointegration refers to the direct contact between bone and implant. A study where HA was implanted in the center of the medullary cavity of the proximal tibia of Japanese adult rabbits showed that 28% of the HA was covered by new bone after 24 weeks. However, HA implanted transcortically had 68% of its surface covered by new bone by 8 weeks [21]. Spector et al [65] showed that increased crystallinity of HA and removing impurity phases from a plasma-sprayed HA coating had no affect on the rate of bone bonding nor the bone density. Plasma-sprayed HA coated Ti-6Al-4V plugs were implanted into the femurs of dogs and resulted in an accelerated rate of osteoconduction than uncoated implants [66].

2.4.2 Bioactive Glass

A bioactive ceramic known as Bioglass® was discovered during the late sixties by Hench [34-36, 56]. Through both *in vivo* and *in vitro* tests, BG has been found to be biocompatible. Glasses or glass-ceramics used *in vivo* possess the ability for bonding chemically with living tissues due to controlled rates of surface reactions with the surrounding body fluids. "Bone bonding" refers to an interface that develops between Bioglass® and bone. This interface becomes continuous on the Angstrom level [35, 36, 67-69]. These surface-active ceramics are, referred to as bioactive ceramics, composed of varying weight-percents of Na_2O-CaO-P_2O_5-SiO_2. Depending on the crystallinity of the material, the glass may be called a Bioglass-ceramic, surface-reactive glass-ceramic, or a bioactive glass-ceramic [18, 35]. Other surface reactive materials, soda-calcia-phospho-silicate glasses, glass-ceramics, and dense hydroxyapatite, also undergo chemical reactions

with the physiological surroundings which eventually lead to bond formation between tissue and implant [18]. Surface reactive ceramics allows for stabilization of the interface by initiating osteocon-duction, however, ceramics are typically brittle and therefore must be applied as a coating on a stronger material.

The composition dictates the level of biological reactions that may occur at the interface between Bioglass and tissue. Figure 2.8 shows a compositional range chart of Bioglass. Surface-active ceramics tend to create an interface with bone that is actually stronger than either the bone or even the implant [68]. Mechanical tests have shown that failure almost always occurs within the bone itself [18, 68]. Region A encompasses the appropriate compositions for tissue bonding which has been noted to occur as early as two to four weeks in the tibiae of rats [35]. Region B indicates the compositions of Bioglass that may exist as inert materials while invoking the formation of fibrous capsules. Glasses that fall within region B contain higher amounts of SiO_2 and are therefore less soluble or less bioreactive. Region C includes glasses with less CaO but more Na_2O making them more soluble. Bioglasses in region C resorb into the tissue and are expelled with no adverse affects [35, 56, 67, 68] Area D depicts the materials that bond with bone but are no longer considered to be a glass because of the lower content of SiO_2 [36, 56]. Bioglasses that bond with bone experience a dramatic increase in surface area once enveloped in body fluid. Ultrapores of about 3-30 nm in size begin to form as an active silica-rich layer and hydroxyapatite crystals develop on the surface. The hydroxyapatite allows the incorporation of collagen, glycoproteins, and mucopolysaccharides into the surface-active layer. The hydroxyapatite and silica-rich layers are crucial in the mechanism of tissue bonding [35]. This organic-inorganic interface, found with glasses in region A, provides a strong bond. Glasses from region B, however, do not form an adequate hydroxylapatite surface. Region C has glasses that are too reactive, causing them to breakdown prematurely [35, 67].

A composition ratio of network former to network modifier, was developed to modify the rate of bond formation and level of reactivity [36, 70].

$$\frac{SiO_2}{CaO+Na_2O+K_2O} \qquad (2.14)$$

The higher the value of Equation 2.14, the solubility decreases, thus, the slower bone-bonding rate. On the contrary, the lower the value, the higher the reactivity as well as the rate of bonding.

2.4.3 Material Properties

The use of bioactive ceramic coatings was to replace the use of a PMMA bone cement which served as a grouting material between implant and host bone. Previous *in vivo* investigations using BG coatings on orthopaedic implants for the sake of replacing the PMMA fixative showed an increase in the resilience of the implant [18, 62]. Table 2.3 compares typical material properties of calcium phosphates, BG and PMMA.

2.4.4 Bioceramics as Coatings

Bioceramics initiate early bone formation but their brittleness requires the incorporation into a composite system with a stronger material such as a metal alloy [18]. Hydroxyapatite (HA) coatings have been applied to the surface of porous implants by the plasma arc spraying method. HA has been reported to be the most stable form of $CaPO_4$ and is considered the most biocompatible ceramic. The monolithic form of HA has a low tensile strength and low resistance to fatigue [19]. The purpose of the application of HA onto metal implants is to combine the strength of the metal as well as the biological responses of HA. HA appears to stimulate osteoblasts during the first four weeks of implantation [3]. HA-coated metal implants were not load bearing, for example, de Putter et al [18] used HA as transmucosal implants that yielded natural gingival tissue responses, therefore, the action of chewing caused the implant to fail due to fatigue. Therefore, de Putter concluded that HA would be of no use in the clinical world when faced with forces other than compression. A group of researchers from the Netherlands [18] believe that prestressed HA implants may fair well under cyclic loads.

The purpose of the Bioglass is to initiate fixation between implant and tissue. Muscle as well as other soft connective tissue will bond with the implant if it is immobilized. The prevention of micromotion is necessary at the implant/bone interface for this process to occur. If motion occurs too early, for instance, the mineralization of bone is prohibited and a fibrous capsule forms or wear may develop loose BG particulates that are disposed of by the body without harmful effects [35]. Bone bonding has been seen as early as ten days to eight weeks post-operatively in rat femora [18, 35]. Piotrowski et al [72] showed that a plasma-sprayed Bioglass-coated 316L stainless steel partial hip prosthetic exhibited low structural strength which was attributed to the low resistance to fatigue of the BG and partial resorption of the glass coating. Bioactive glass coatings may reduce metallic corrosion and possibly wear, although, these concepts must be further explored [18, 68, 73, 74].

Substrates like stainless steel, vitallium, titanium, and high density alumina ceramic have been flame-spray-coated with BG [18]. Although the literature cites the consequences of inadvertently introducing other substances to the glass. For example, aluminum has an inhibitory effect on the bonding capabilities of the glass [18]. Also, certain oxides especially zirconia, tantalum oxides, and titania, disrupt the osteoblast metabolism and collagen deposition [18].

Greenspan and Hench [36] devised a method of coating Al_2O_3-ceramic with bioglass. They observed that two applications of coatings of bioglass were preferred due to the lack of bone-bonding capability brought on by the diffusion of Al into the bioglass. The first layer allows for the diffusion of Al while the second layer of bioglass retains its original composition. Gross et al [36] also found that Al_2O_3 tends to reduce the extent and effectiveness of bonding between bone and BG.

2.4.5 Methods of Coating

One of the conventional methods of coating orthopaedic metal implants with ceramics is plasma arc spraying (Figure 2.9). This procedure was first introduced to the medical field in the early 1980's by Biomet, Inc [62, 73]. Plasma spraying involves a

plasma arc generator as a thermal and kinetic energy source to spray molten material onto a substrate. Upon deposition, these droplets of molten ceramic quench and become the coating structure. A thermal plasma is usually composed of inert gases such as Helium or Argon which are injected into an arc chamber where a DC arc induces the ionization process and the temperature surpasses 15,000°C. Then powder ceramic is injected into the gun where it becomes molten and sprayed onto the substrate [17, 62, 63, 73, 75-77]. The spray parameters play a significant role in the biological properties of the ceramic since the composition and phase of the spray material may be altered during the high temperature process [19, 62, 63, 74, 76, 78, 79]. Bioceramics are commonly applied to porous surfaces in order to induce both phsyiochemical bonding as well as mechanical interlocking which would increase the resistance of the implant under shear and tensile loads at the interface [34].

In addition to plasma arc spraying, bioglass may be applied to a substrate by the dipping method which begins with the oxidation of the metal. This oxide layer is necessary for a continuous transition at the interface between glass and metal. The second step is annealing of the oxide. This procedure permits the substrate to have similar total shrinkage rate to glass during the cooling from annealing to room temperature. Then the substrate is dipped into molten glass (1350°C) and removed for the final step of annealing (525°C). This final annealing process with controlled cooling relieves any excessive internal stresses that may exist within the bioglass [36]. Campbell et al [80] investigated new techniques, Void Metal Composite and Surface Induced Mineralization, to apply calcium phosphate coatings on metal substrates.

2.4.6 Bone-Bonding Mechanism

The mechanism responsible for the bonding of bioactive-glasses to tissue involve both physicochemical and ultrastructural reactions [18, 81]. Microscopy reveals that an obvious interface exists between glass and bone but there exists a compositional gradient in the interfacial layer.

Once the glass is submerged in distilled water at 37°C for an hour, alkali ions

leach out and form a silicon-rich layer with which a Ca-P rich layer forms (Figure 2.10) on top as an amorphous structure but crystallizes into hydroxyl-carbonate apatite after 7 to 10 days [36, 77, 82-85]. The rate in which hydroxylapatite bonds with the Ca-P layer depends on the composition of the glass. These reaction layers are imperative for bone-bonding to occur. A Ca-P layer has been observed without bone-bonding in past studies. The rate of bone-bonding is dependent on glass composition: lesser SiO_2 content increases the rate of bonding, however, higher rates of bonding promotes increased solubility [36]. Collagen fibers that may exist in the same solution with the Ca-P-rich layer eventually become integrated with the apatite crystals. Chondroitin sulfate D, a muco-polysaccharide, amplifies the interaction between the apatite layer and the collagen. An 80-100nm thick amorphous region is present between the collagen fibers and the glass. This region may contain mucopolysaccharides, glycoproteins, and nectins, and can be mineralized [18]. Then osteoblasts lay new bone by providing collagen and a matrix of vesicles in which mineralization can occur [18, 86].

Resorbable materials degrade as calcium and phosphate salts which are metabolized within hard tissues [18]. Resorbable bioactive ceramics, such as tricalcium phosphate and calcium-aluminate-phosphate offer great potential for participating in bone replacement, however, significant research is required to establish an appropriate degradation rate which will maintain the strength of implant-tissue interface [72, 87, 88]. The degradation rate is crucial for strong fixation of an implant. If the ceramic coating were to resorb too quickly, the mechanical strength of the implant/bone interface is compromised and may fail over time. Therefore, the rate in which the coating degrades must be long enough to allow for adequate bone formation.

2.5 Finite Element Analysis (FEA)

In 1960, Clough [89] coined the phrase "finite element method" when studying problems of plane elasticity. Years before the method was defined as finite element analysis (FEA), mathematicians, physicist, and engineers employed this technique to serve

there own purposes. The mathematicians were interested in continuum mechanics; the physicist studied piecewise approximate functions; and engineers strove to improve aerospace structures. Today, FEA has become an increasingly popular method of simulating or predicting the outcome of experimental research in various disciplines. FEA offers a controlled, numerical research medium where a number of slight variations in the model or the parameters may be implemented with relative ease. The use of FEA may reduce the number and subsequently the cost of animal experimentation for medical research.

The finite difference method [58, 89, 90] has generated several approximate numerical methods. This includes pointwise approximation for the governing equations. The model is solved with difference equations for an array of grid points. The outer limits of the model are approximated by a sequence of horizontal and vertical lines that are often referred to as the "stair steps" (Figure 2.11). The more points present in the model, the more accurate the results. Finite difference schemes are not sufficient for solving models of complex geometries. The finite element method, however, is more robust and can handle complex geometries. Instead of treating the model as an array of grid points, the finite element method, divides the model into small regions or elements. These elements can be placed within various intricate geometries. The outer boundaries of the model need not be approximated as is the case for the finite difference method, since the boundaries are represented by the straight edges of the elements. Curved boundaries are split into smaller element edges to accommodate for this curvature. The finite element method uses the piecewise approximation for the governing equations.

When beginning an FEA, one must decide on an appropriate element type. Numerous varieties of element types are available for a variety of applications. Examples of two-dimensional element shapes include triangular and quadrilateral elements with anywhere from three to nine nodes per element. Typically, a node exists at the corners of an element or with the serendipity family [1, 91], at the midpoint along each edge of an element. For the Lagragian family, a node is present in the center of an element. The nodes define the shape function which are collectively applied to the global matrix, or the

system of equations, during the solution process. Not only does the dimensionality of the model dictate the chosen element type but also the type of analysis plays a role. For instance, element types for structural, thermal, electromagnetic, etc. analyses exist with a variety of shapes and number of nodes for both two- and three-dimension models. An intriguing element type is the contact element which is actually a fictitious element that is applied along two surfaces that may be loaded in such a way as to create normal contact or shear.

One advantage that finite element method has over other numerical methods is that it is capable of computing the equilibrium characteristics equations for the solution phase for each element before it compiles the global equilibrium. Finite element methods present three approaches to solving models: direct approach, variational approach, and weighted residuals approach [89]. The direct approach is the simplest in which there exists the same number of unknowns as equations and the exact solution is computed in a closed form manner. The variational approach, however, is more complex and is based upon the calculus of variations and extremization of functionals. The weighted residual approach [89] is more flexible than the variational approach. This method uses the governing equations to compute solutions without the need for a variational statement. The weighted residuals approach may be used in problems where no functional exists. Energy and momentum transfer problems, such as heat transfer and computational fluid mechanics, commonly take advantage of the weighted residuals approach.

After one generates a model by defining its domain and given a specific element type, the areas or volumes must be discretized or meshed into smaller regions of elements. One model may contain two or more different element types depending on the needs of the investigation.

The issue of material properties is handled with various degrees of sophistication in today's FEA codes. Depending upon the needs of the model, properties may be assigned variance with location, or variance with orientation in the case of orthotropic materials. As well, in cases involving significant temperature changes, material properties will need to be specified as a function of temperature. Nonlinear material behavior such as

hyperelasticity, plasticity, or viscoelasticity need to be appropriately submitted as data and used with the appropriate nonlinear parameters at the solution stage.

Depending on the type of analysis, different types of boundary conditions are applied to the model. Structural analysis permits the application of active loads along an edge, on certain nodes, and on surfaces. Heat transfer problems could have applied heating or cooling systems or even convection flows anywhere in the model. The decision on where to place constraints is crucial for representative solutions. One who is solely interested in heat transfer, for instance, need not be concerned with constraining the model for purposes of holding it in place. Structural problems, on the other hand, must have adequate constraints to eliminate zero energy nodes in the model.

The solution process can be applied in several ways with load stepping, time stepping, or a single load step. Load stepping allows the active load to be applied incrementally whereas a single load step applies the force all at once. Time stepping offers the freedom to select sub-steps between load steps. Load stepping is common for finite strain problems or for cases where a material exhibits nonlinear behavior. Load stepping or time stepping in transient problems, is a critical process with regards to obtaining a solution and reliability of this solution. Stepping has to be adequate to avoid solution oscillation yet ensure an accurate solution. Stepping is also directly reflected in solution times, hence the cost of obtaining the solution.

Post-processing is a very important phase of FEA. With it one can readily extract key information about the model from vast amounts of data. Such information can be in the form of plots or contours with which trends over the model become easier to see. Results can be viewed based on the elements or nodes. As well, results can be plotted along paths of interest through the model or characteristics at individual nodes as a function of time. Plot control manipulations have become quite sophisticated, allowing for magnification of a region, rotation of solids, and slicing of solid models along any defined cutting plane to reveal hidden or interior details in the model. Structural response parameters such as stress, strain, and displacement of the continuum can be examined through the post-processor.

The most important aspects of FEA technology have been completed to date [89], however, much work is needed to improve and understand broader applications and multidisiplinary relationships in solid mechanics. Fundamental pursuits of the robustness of FEA such as convergence rates, stability, and accuracy in the linear and nonlinear regimes continue. The acceptance of FEA as a design and analytical tool has continued to grow. With this growth, pressure on code developers has resulted in a continuous improvement in the user friendliness of FEA codes. In fact, the medical field has acquired an increasing interest into numerical modeling where predictions of healing and mechanical behavior of implants are studied before surgical implantation. FEA modeling of interfaces controlled microstructurally was performed for post-solution stress-strain testing of animal implants. Long-term results are sought via FEA with a comparison of experimental results [18, 23, 39, 41, 46, 47, 49, 71, 92-111]. One must always realize that FEA cannot completely replace experimental work, however, it can be used as an effective tool to test the effect of material property, geometry, and boundary condition variations upon experimental models.

Table 2.1 Material properties of given implantable metals and bone [11,20,73,102,105,166,178].

Material	Modulus of Elasticity (MPa)	Ultimate Tensile Test (MPa)
Ti-6Al-4V	110X103	900
Co-Cr-Mo	248X103	660
Cortical bone	13700	N/A
90% cancellous bone	7930	N/A
10% cancellous bone	508	N/A
Femur (long axis)	17	130
Spongy bone	0.1	2

Table 2.2 Composition of standard bioceramics.

Chemical	weight percent
Al_2O_3	99.6
SiO_2	0.12
Fe_2O_3	0.03
Na_2O	0.04

Table 2.3 Chosen material properties of various bioceramics [2, 17, 52, 56, 59, 71].

Property	Calcium Phosphate	BG (45S5)	PMMA
Young's modulus (MPa)	400 - 117000 (HA = 85MPa)	~35000	2200±60
compressive strength (MPa)	294 (HA = 650MPa)	N/A	91.7±2.5
bending strength (MPa)	147	~77	N/A
Hardness	3.43 (Vickers, Ga)	450 (Hv)	N/A
Poisson's ratio	0.27	0.33	N/A
tensile strength (MPa)	(HA = 250MPa)	N/A	1.10-1.23

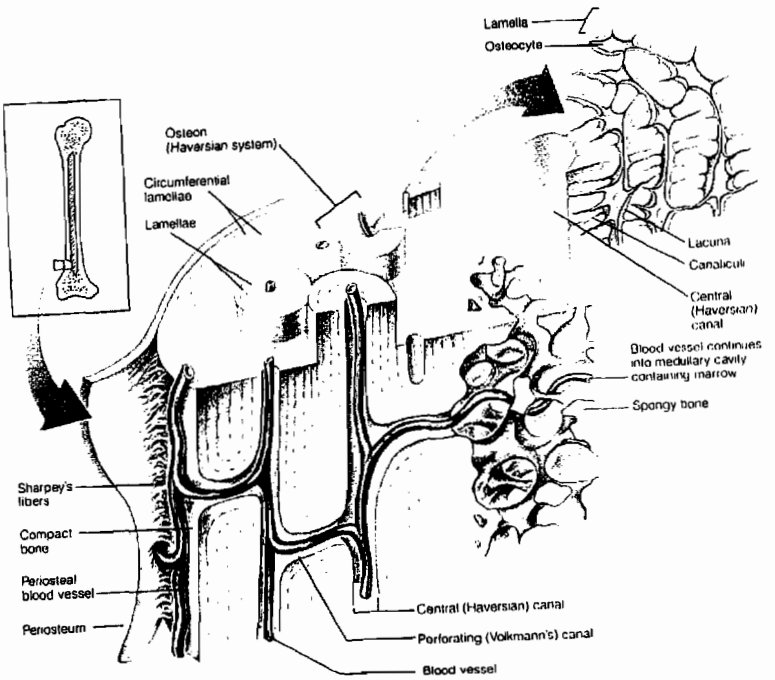

Figure 2.1 Sectioned view of the Haversian system, lamellae, cancellous and cortical bone, and osteocyte. [12]

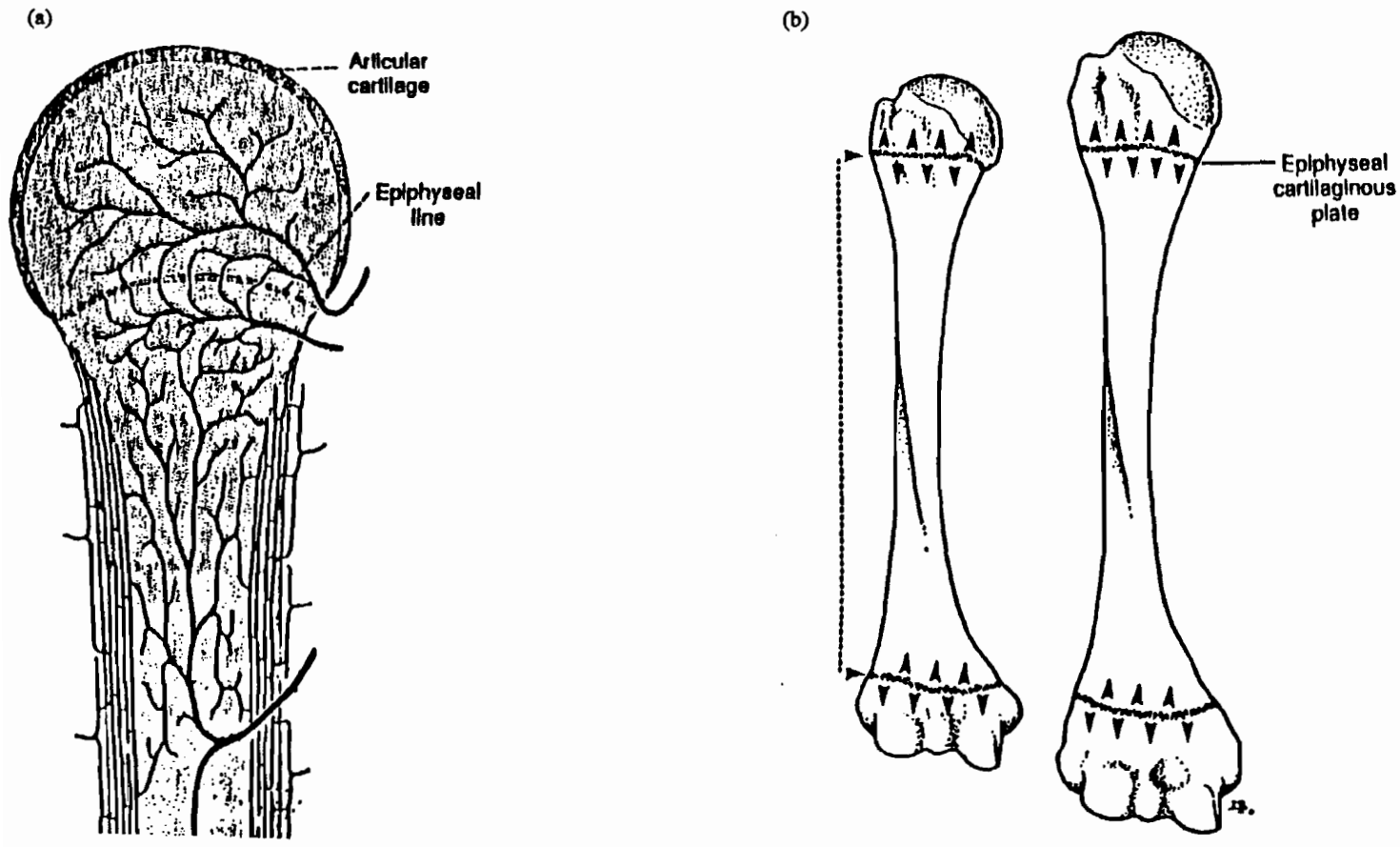

Figure 2.2 (a) cross-section of bone showing articular cartilage and epiphyseal plate, (b) bones with epiphyses, diaphysis, and epiphyseal plate. [12]

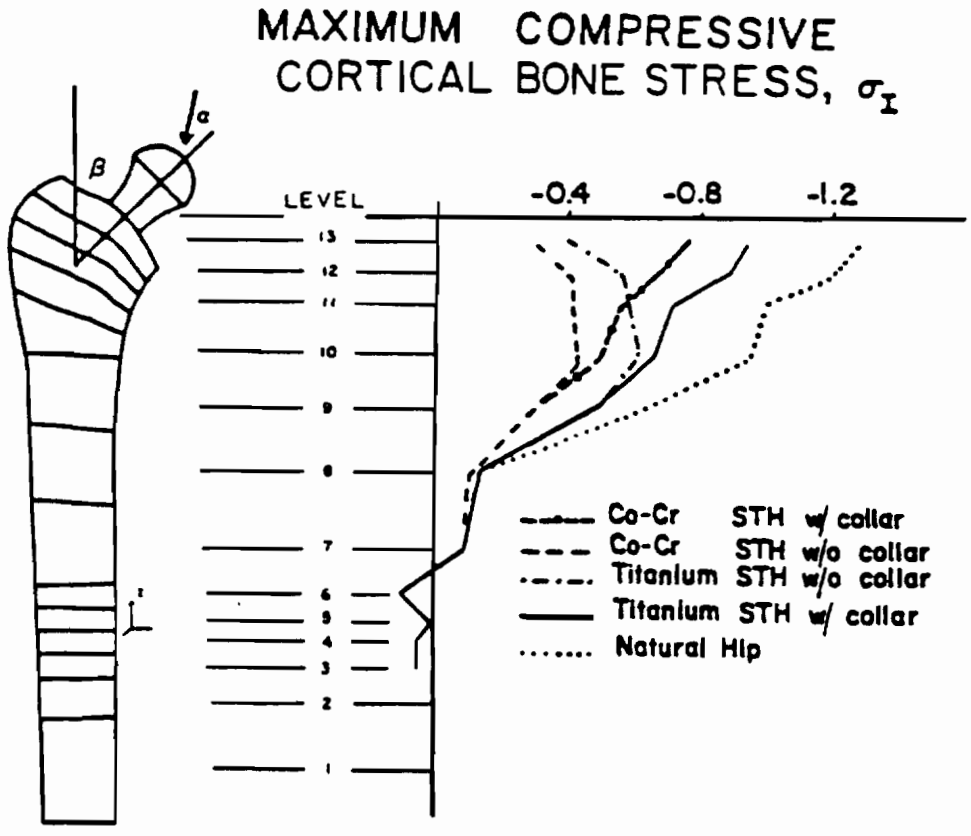

Figure 2.3 Graph of compressive stresses experienced by Co-Cr implants with and without implant collar, Ti with and without implant collar, and by natural bone. [14]

(a)

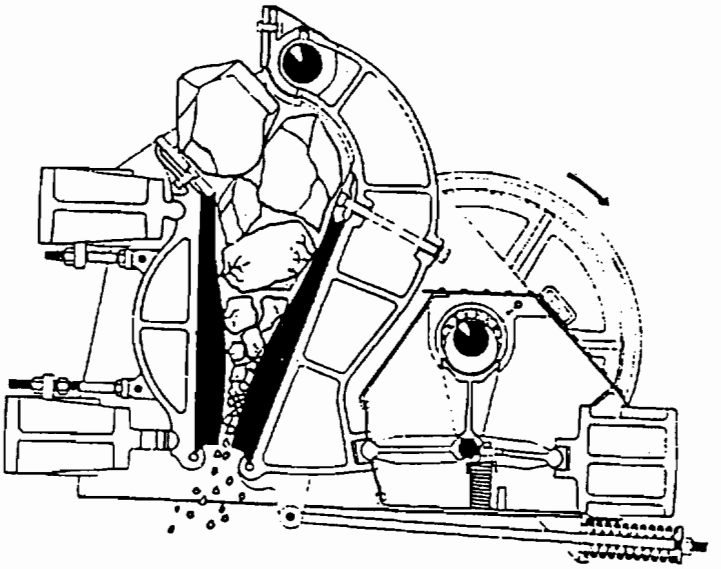

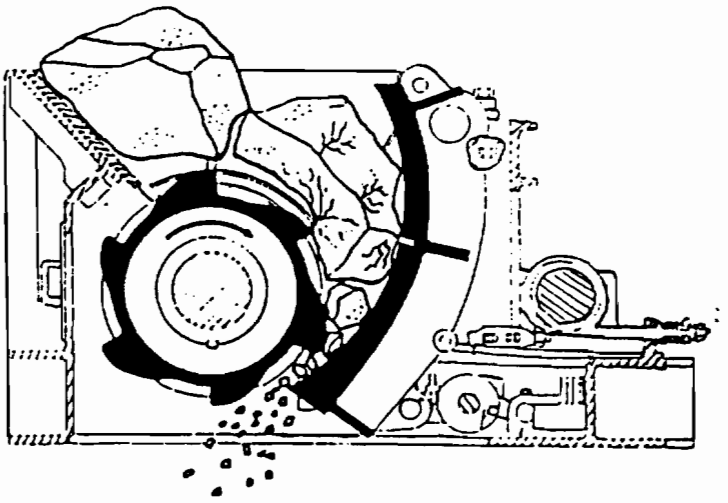

(b)

Figure 2.4 (a) Grinding raw ceramic material between metal jaws, (b) Grinding of raw ceramic material with toothed crusher and plate. [54]

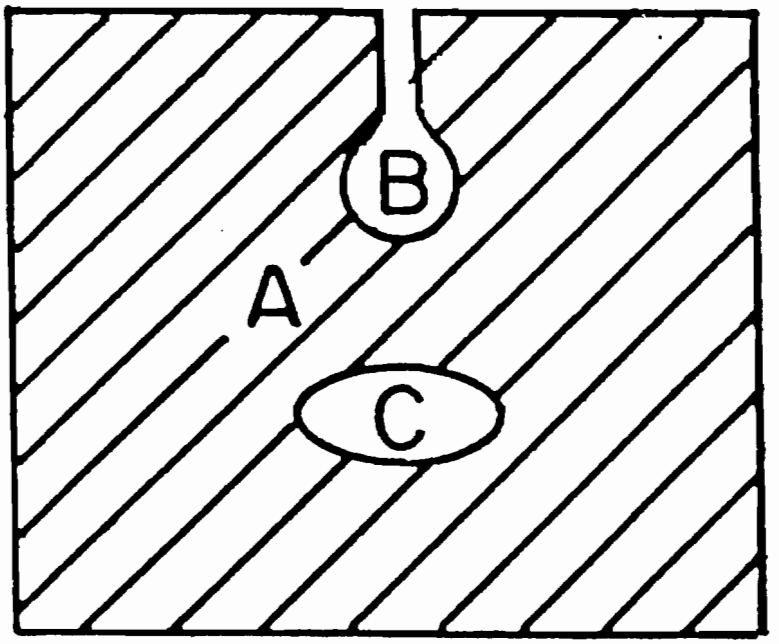

Figure 2.5 Model of ceramic: A=solid volume, B=open pore, and C=closed pore.

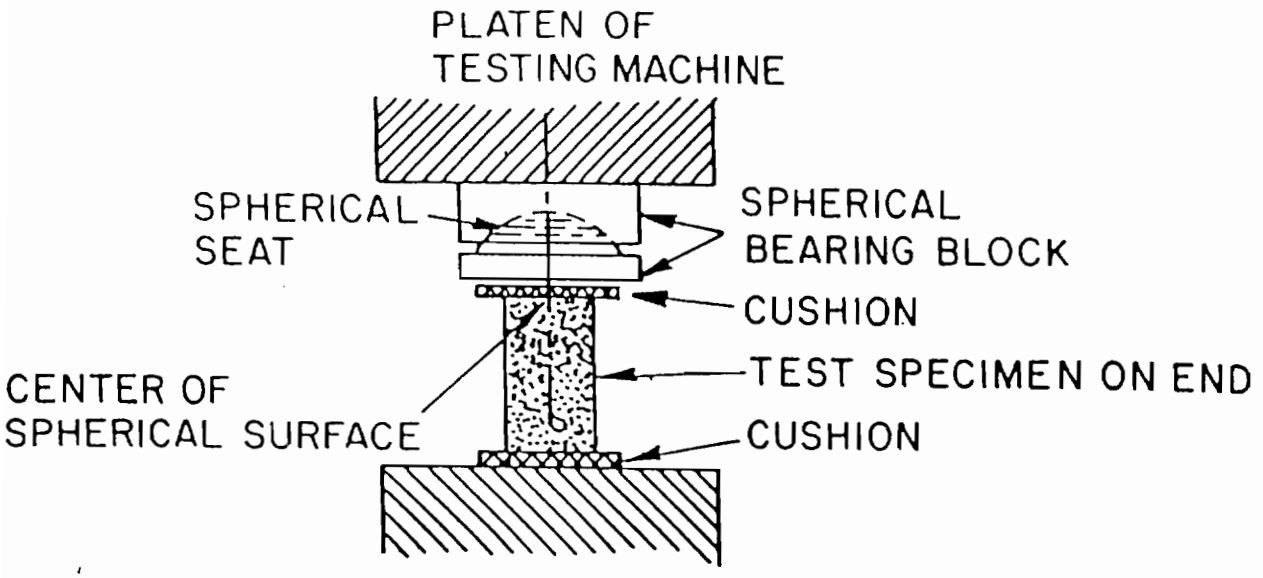

Figure 2.6 Compressive test configuration for ceramics. [54]

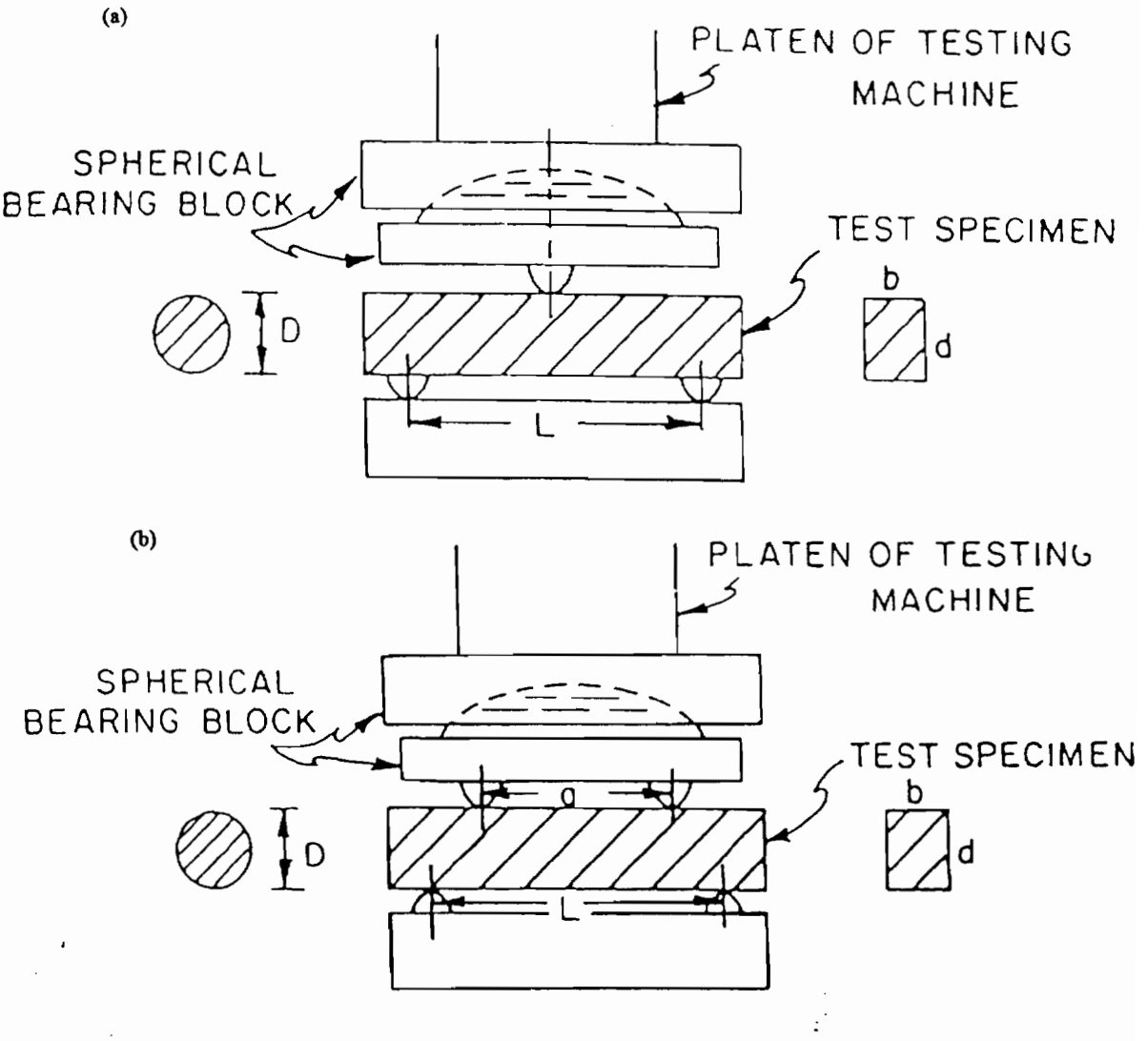

Figure 2.7 (a) Three-point bend test configuration for ceramic specimens and (b) Four-point bend test configuration for ceramic specimens. [54]

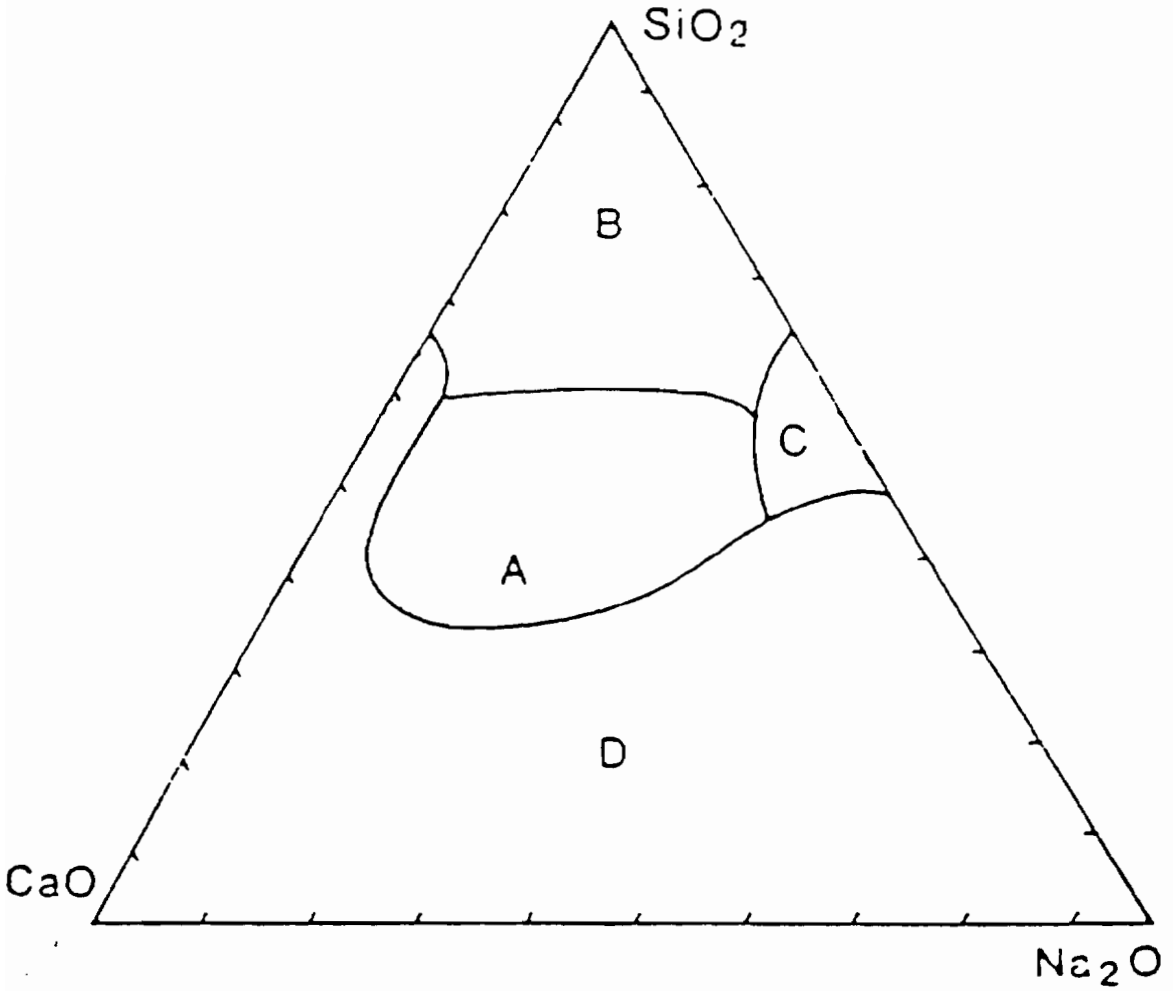

Figure 2.8 Compositional triad of bioactive glass. [35]

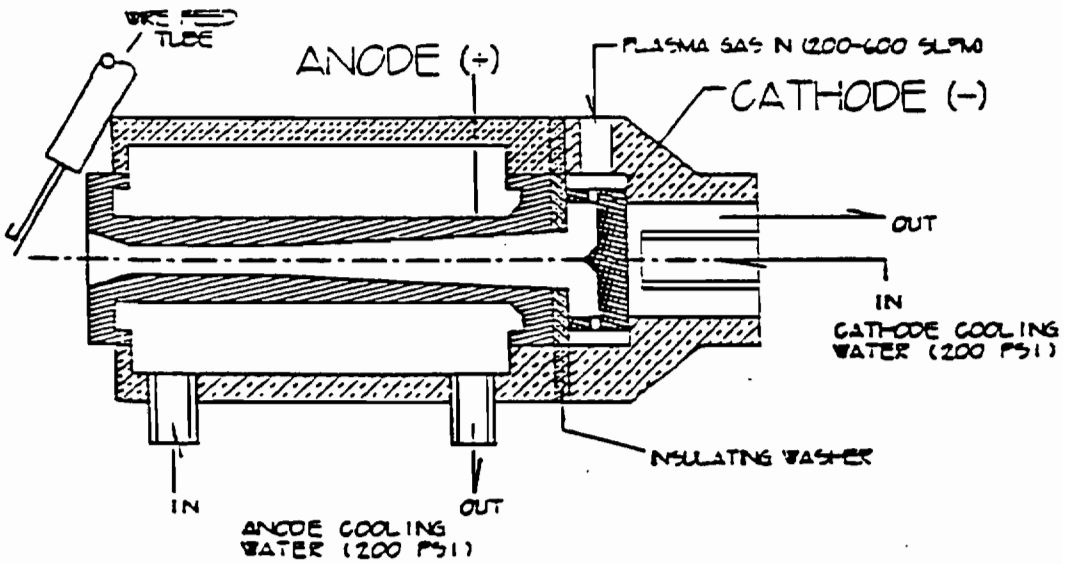

Figure 2.9 Plasma-spray gun [123].

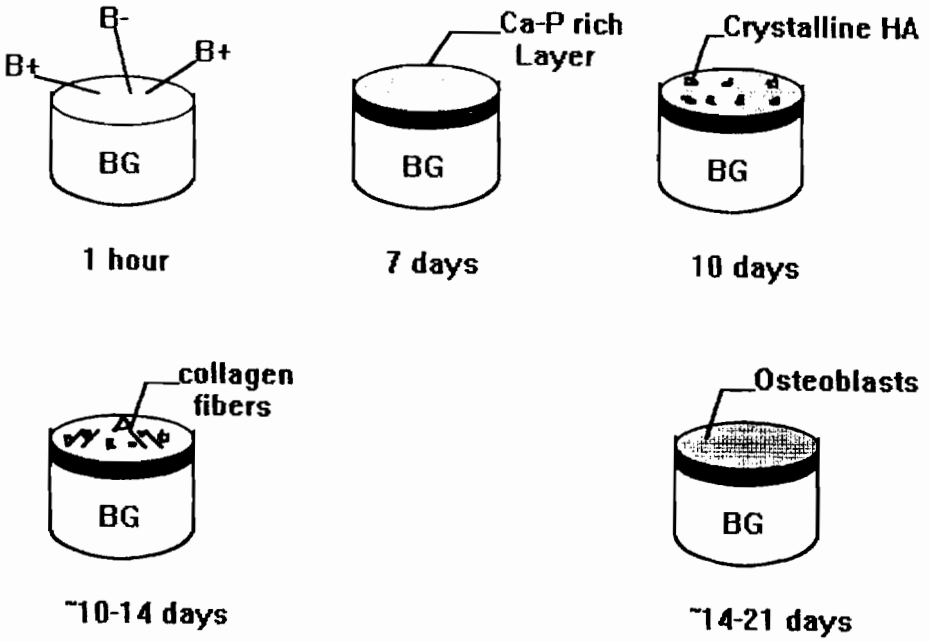

Figure 2.10 Tissue bonding mechanism of BG.
Note that $B^{+(-)}$ signifies alkali ions leaching from the BG surface.

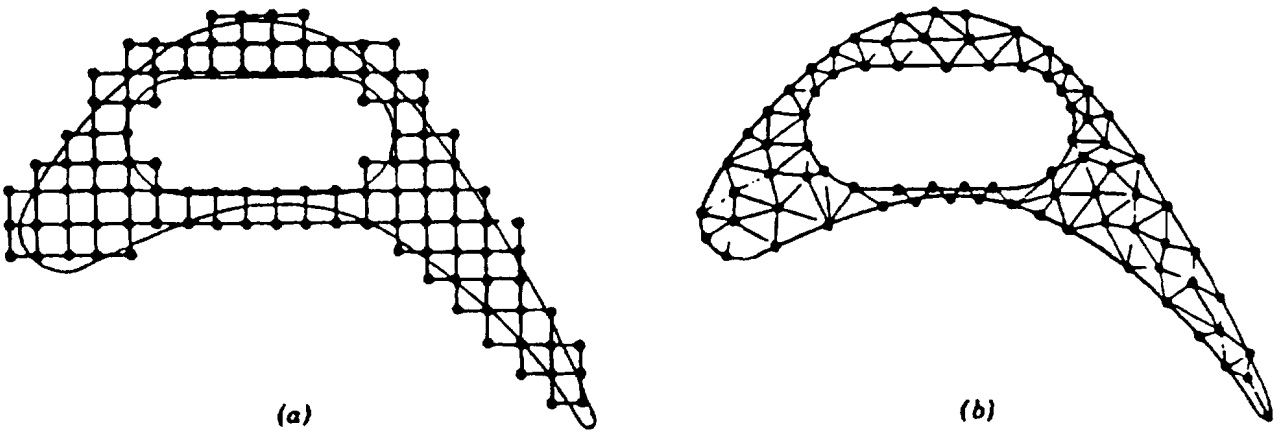

Figure 2.11 (a) Finite difference discretization and (b) Finite element discretization. [89]

CHAPTER 3

MATERIALS & METHODOLOGY

3.1 Mechanical Tests

Various mechanical tests have been performed to characterize the material properties of BG and Ti-6Al-4V. These material properties were then compared with properties previously recorded in the literature and applied as data in the Finite Element Analysis (FEA). A tensile bond strength test of the plasma-sprayed BG on Ti-6Al-4V was used to validate the FEA model.

3.1.1 Modulus of Rupture

Bioglass (45S5 composition) was manufactured into twenty-five 5mm X 5mm X 20mm rectangular cross section rods. With expert advise on specimen preparation [112], the sides of the specimens were not polished for fear of creating microfractures. The as-cast sides were measured, using a micrometer, at five locations along the length of the specimen to ensure a relatively uniform cross-sectional area. Each side had a slight concave contour along the length. This concavity is often found in cast materials. During the process of measuring dimensions, four of the specimens were observed to have defects. These were used as practice test specimens. Prior to testing, the tensile surface was marked with ink to aid in fracture analysis later.

A fixture for small three-point bend specimens was fabricated with ground-cemented-carbide cylinders, 6.35±0.02mm in diameter and 0.3mm in length as the two bottom supports. A 10mm cemented tungsten-carbide ball acted as the center point load.

The two cylinders were placed ~14mm apart, with the ball centered between this span length. This three-point bend test was conducted in accordance with ASTM B406-90 standard (Figure 3.1) [113].

A compressive load was applied at a rate of 2.54 mm/min until complete failure occurred. The test was accomplished using an Instron testing system with the load-displacement curve plotted on a Hewlett Packard 7046A X-Y Recorder. The failure load was recorded and used to calculate the modulus of rupture (MOR) for each specimen with the following relationship:

$$MOR=\frac{3PL}{2bh^2} \tag{3.1}$$

where b = the specimen width (mm), h = specimen thickness (mm), P = failure load (MPa), and L is the span length (mm).

3.1.2 Ti-6Al-4V Tensile Test

Three ASTM standard 505 round tensile samples were machined from a Ti-6Al-4V stock bar. Sample preparation began with a surface treatment which included rubbing of isopropyl alcohol as a degreaser, abrasion with 320 grit paper, then conditioner A and neutralizer 5A. The latter two steps were accomplished with solutions provided by Measurements Group, Inc. The conditioner and neutralizer were not permitted to dry on the sample surface for prevention of film formation.

A 90° strain gage rosette was placed on cellophane tape then applied to the center of the gage length on the tensile bar. One end of the tape was carefully peeled back just enough to lift the strain gage off the surface yet allow it to be held in position. The back of the gage was brushed with the MBond-200 catalyst and allowed to dry for one minute. One drop of MBond-200 polymer adhesive was placed on the specimen surface, under the patch where the strain gage would lie. Then the previously peeled portion of the tape was replaced in order to place the gage back into position. Pressure was applied over the gage with the thumb which would emit heat to accelerate the curing process of the adhesive.

After one minute of pressure, the tape was cautiously removed while leaving the now adhered strain gage (Figure 3.2).

Wire leads were soldered to the solder tabs on the strain gage to permit the recording of longitudinal and transverse strains occurring at the center of the gage length. A voltage calibration value was calculated as 0.978V with the use of the following equation:

$$\mu\varepsilon_{cal}=[\frac{R_A}{K'(R_{cal}+R_A)}]X10^6 \qquad (3.2)$$

where $\mu\varepsilon_{cal}$ is the microstrain calibration, R_A is the gage resistance of 350Ω, K' represents the gage correction factor of 2.04, and R_{cal} is the calibrated internal resistance which was set to 175000Ω. The converter box was then set to the calculated voltage calibration. The leads were then connected to the 10 channel strain-gage conditioner and amplifier (Measurements Group, Inc) then distributed to the Hewlett Packard 7046A X-Y Recorder and the data acquisition software. The specimens were placed into threaded fixtures on an Instron 8500 and loaded to failure at a rate of 0.1in/min.

3.1.3 Bond Strength Test

Forty-two Ti-6Al-4V coupons were cut into cylindrical samples, 0.5in in length and 1.0in in diameter. The flat surfaces of each coupon were sand blasted to enable solid adherence of the sintered titanium beads. The coupons have been separated into four groups: 4 smooth with 40μm BG, 6 smooth with 75μm BG, 12 25/35 mesh porous surface with 40μm BG, and 12 25/35 mesh porous surface with 75μm BG. Each group had four additional coupons for destructive measurements of the BG coating to ensure uniformity.

Before plasma-spraying the BG, the highest beads were sanded with 240 grit to create a flat surface for optimum epoxy adhesion to the test fixture. All of the groups

were plasma-sprayed with BG to the appropriate thickness. Then each specimen was laid BG down onto a "mushroom" cap (made of F75 => Co-Cr-Mo) with an FM1000 disc between them. The FM1000 is a thermoset epoxy adhesive that acts to bond the test specimen to the "mushroom" caps or holders. Another FM1000 disc was placed on top of the sample and a second "mushroom" cap was placed, inverted over the disc. These "mushroom" caps enable gripping of the specimen by the fixtures for tensile loading. Figure 3.3 shows the samples under a compressive spring load with ~30 lbs and placed into a furnace which was gradually heated to 350°C for two hours to allow for adequate curing of the FM1000. The furnace cooled down for an hour before removing the specimens.

ASTM F1147-88 [114] was used instead of ASTM C633-79 [115] as originally planned because it updated and referenced ASTM C633-79 and they were identical except for a slight change in sample diameter and a difference in loading rate. The cross-head rate chosen was 0.1in/min. Figure 3.4 shows the testing configuration with the sample and gripping fixtures.

After sufficient cooling, a sample was placed in the fixtures of an ATS No .A840018 (Applied Testing Systems, Inc.) and loaded in tension (Figure 3.4) until failure occurred. Upon completion, the second "mushroom" cap was removed from the specimen by applying heat to the FM1000 interface allowing for the adhesive to melt, hence easy removal of the coupon.

3.2 Scanning Electron Microscopy (SEM)

Fracture analysis of the mechanical test specimens were performed on Zeiss Digital Scanning Microscope DSM 960. The fracture surfaces of a BG modulus of rupture specimen and Ti-6Al-4V tensile sample were analyzed. Cross sections of the bond strength specimens were scanned for BG coating thickness measurements and compositional EDS which were analyzed with the Link^{eXL} software. Finally, area fraction measurements were made with the backscatter detector and image analysis software.

3.2.1 Secondary Electron

A global representation of the fracture surface of BG-MOR specimen number 23 was examined at a voltage of 10kV at a magnification of 14X with the secondary electron detector. One area was analyzed with both secondary and backscatter electron detectors at a magnification of 5000X at a voltage of 10kV.

One of the fractured ends of Ti-6Al-4V tensile specimen number 2 was cut off to allow for the surface of interest to slide into the SEM without damaging the detectors. This was accomplished with a Buehler Isomet low speed saw while lubricating with diamond blade oil. A global view of the fracture surface was also taken at a voltage of 10kV at a magnification of 10X with a secondary electron detector. At the same voltage and detector, the magnification was increased to 100X for a closer look at the fracture surface.

One representative specimen was chosen from each group of the bond-strength tensile samples: 40μm BG - porous --> specimen 2
40μm BG - smooth --> specimen 5
75μm BG - porous --> specimen 5
75μm BG - smooth --> specimen 1

The four specimens were cross-sectioned with a Buehler Isomet low speed saw with a diamond blade oil as lubricant. One of the sectioned halves of each specimen was set into bakelite (EXTEC green/brown, phen.mnt.pwdr.) using the LECO PR-30 1.25 mold heater-cooler for nine minutes. The flat surface of the specimens were exposed using a grinding wheel with 120 grit paper. The grinding continued with 240, 400, then 600 grit paper. The final polishing involved 6μm diamond polish with diamond extender oil on an EXTEC polishing cloth. The porous coupon coated with 75μm of BG was actually the only specimen left unpolished for fear of disrupting the brittle ceramic. The unpolished results were compared with those of the polished specimens. This specimen was analyzed for BG composition at two locations (Figure 3.5). These were taken at a magnification of 100X under an accelerating voltage of 10kV. The smooth coupon with a 75μm BG coating was also analyzed for BG composition on the two locations shown in Figure 3.6.

The first scan was taken at a magnification of 1000X under an accelerating voltage of 10kV. The second scan was observed with a 500X magnification at 10kV. Figure 3.7a depicts the cross-section of the Ti beads that were sintered onto the Ti-6Al-4V substrate. A porous specimen coated with 40μm BG coating was also scanned twice for BG composition. The first scan was performed with a magnification of 5000X at an accelerating voltage of 10kV (Figure 3.7b). The second scan was observed under a 3000X magnification (Figure 3.8a). Figure 3.8b shows this same field which was reduced to a magnification of 2000X and analyzed under the backscatter electron detector to confirm the different compositions of the specimen. The smooth coupon with a 40μm BG coating was examined for BG composition at magnifications of 5000X and 2000X; both at an accelerating voltage of 10kV (Figure 3.9).

A smooth polished, unfractured BG specimen was also analyzed with the SEM for purposes of comparison with the SEM of the BG-MOR sample. The surface was coated with platinum to allow for conductivity and prevention of charging of the specimen. This polished BG specimen was analyzed under an acceleration voltage of 10kV at a magnification of 5000X with both the BSE and SE detectors.

An untested "practice" plasma-sprayed BG on metal was cross-sectioned and analyzed under the SEM purely for qualitative information. The sample was also sectioned with a Buehler Isomet low speed saw with diamond blade oil as a lubricant. At a magnification of 100X and accelerating voltage of 10kV, one can clearly define the BG coating from the substrate. EDS was performed to get a characteristic spectrum of BG.

3.2.2 Backscatter Electron Imaging

Number 4 of the smooth bond strength specimens coated with 40μm of BG was sputter coated with a thin layer of gold/palladium. EDS was performed for confirmation of the BG regions still adhered to the Ti-6Al-4V substrate. These spectra were performed at a magnification of 1000X at an accelerating voltage of 20kV (Figure 3.10). Thirty fields were imported into the Image analysis software for area fraction measurements (Figure 3.11). No smooth coupon with a BG coating of 75μm were suited for area

fraction analyses. A porous specimen with a 40μm BG coating (number 9) was also sputter coated with gold/palladium and analyzed with EDS under a magnification of 50X at an accelerating voltage of 20kV. Again, thirty fields were recorded for area fraction analysis (Figure 3.12).

3.3 Finite Element Analysis (FEA)

Given the material properties of BG and Ti-6Al-4V from the mechanical tests, several FEA models, both two- and three-dimensional, were constructed. The primary concern of the FEA was to simulate the tensile bond strength test performed experimentally. This study was accomplished with the aid of the ANSYS program.

3.3.1 Contact Theory

Contact theory is commonly applied to problems involving two or more bodies that transmit forces via contact points, lines or surfaces. It was considered appropriate to incorporate contact theory in analyzing the tensile bond strength at the interface between BG and Ti-6Al-4V. All of the 2D contact problems had their areas meshed with 2D, quadrilateral 8-noded elements, however, the interfaces were discretized with contact elements. These are three-sided point-to-surface elements with three nodes, one on each corner. The contact theory in the Ansys program used in this study has limited the contact zone being bounded by elements with linear variation along the edges. The surface contact elements are actually fictitious elements that represent the contact/sliding interface on a 2D point-to-surface problem. The elements generated take the form of triangles with two degrees of freedom at each node (Figure 3.13) [1]. The contact interface that is represented by these "fictitious" elements is in the form of a line. Contact elements have specific characteristics that must be addressed. These requirements include the normal stiffness (KN), tangential stiffness (KT), and absolute tolerance (TOLN) for surface inter-penetration compatibility. The value of stiffness is crucial in contact theory in that it cannot be too high or else it may lead to convergence difficulties yet a value too small will

result in excessive inter-penetration of the contacting objects. These qualities ensure that the coefficient of friction does not exceed the value of unity. Contact elements do not always meet the requirements of perfect rigid-rigid contact and therefore, the corresponding TOLN must be assigned a value close to zero to keep penetration to a minimum and yet avoid a gap of exactly zero. As a result, TOLN in the samples presented in the following models was set to 0.001.

Contact elements have several conditions that further characterize them from line elements. The only ones that were pertinent to this study were the type of friction experienced at the interface and contact predictions. The friction may be labeled as no friction, elastic Coulomb friction, or rigid Coulomb friction. For the purpose of this study, elastic Coulomb friction was used. When establishing friction as being anything other than zero, a coefficient of friction ($\mu = 0.5$) was assigned. The contact predictions can be one of the following: no contact time predictions are performed, change-in-contact predictions are made in order to maintain a reasonable time/load increment, or change-in-contact predictions are made in order to achieve the minimum time/load increment whenever a change in contact status occurs.

Two other characteristics of contact theory that are noteworthy include the analysis regime and the contact algorithm formulation. Two regimes are possible namely structural, and coupled thermal-structural analyses. Two algorithm types are supported in the Ansys program, namely the Penalty Function and the Penalty Function with the Lagrange Multiplier. For purposes of this study the penalty function option was used in a structural analysis regime. Three 2D models were built and analyzed, with boundary and initial conditions as follows: Prescribed Displacement, Compressive Point-Load with Initial Gap, and Tensile Point-Load with No Initial Gap.

The three test contact models were analyzed using material with a yield stress of 7000MPa and a plastic modulus of 800MPa. Other material properties assigned to these models was a Young's modulus of $54.9X10^6$MPa and Poisson's ratio of 0.25.

3.3.1.1 Prescribed Displacement

This 2D model consisted of two 1mm X 1mm square areas with a 0.05mm gap between them. Figure 3.14 shows a plot of the configuration of the model. The top area is meshed with a line division of 10 whereas the bottom area is meshed with a line division of 12. This uneven element size across the contact interface allows the contact nodes and target nodes to be slightly misaligned for the generation of contact elements. The nodes on the bottom surface of the top square were designated as the contact nodes. The nodes on the top surface of the bottom square were designated as the target nodes.

The bottom most surface was fixed or constrained in the y direction (the direction of loading). The entire left side of both squares were constrained in the x direction in order to restrict the degree of freedom. With this all in mind, the top area was then subjected to a prescribed displacement of -0.05mm in order to close the gap.

3.3.1.2 Compressive Point-Load with Initial Gap

The model was similar to the one generated in the prescribed displacement problem. This model also had a gap of 0.05mm for the test of closing this gap using compressive point loads on the top surface of the top square. The same surfaces were assigned as the contact and target nodes as in the model above.

This time the only constraint implemented was on the bottom most surface in the y direction. Then an arbitrary compressive load of -100N was applied to the entire top surface to close the gap. Figure 3.15 illustrates this model with the given constraints and loads.

Unsuccessful iterations of this model eventually lead to the use of link elements on either side of the top box in order to provide adequate constraints. Figure 3.15 shows the position of the link elements. Note that the free ends of the link elements were fixed in both the x and the y directions which holds the top box into position, however, allowing for displacement as if the links were soft springs.

3.3.1.3 Tensile Point-Load with No Initial Gap

Like the two previous models, the two squares for this model had dimensions of a 1mm X 1mm square. This time, however, there was no separation (gap size = 0) between the two entities. The same meshing parameters and material properties were assigned as above. Again, the identical surfaces contained the contact and target nodes. Note, the contact and target nodes lie on the lines that essentially are on top of each other.

This model was fixed only along the bottom most surface. It was constrained both in the x and the y directions which depicts the real fixed support that will be applied to the tensile test specimen. Then the top most surface was subjected to an arbitrary tensile load of 100N.

3.3.2 Rigid Contact

Several 2D and 3D models were created for stress distribution analysis of bimaterial butt tensile joints. Many tests were performed to establish trends in the solutions.

3.3.2.1 2D Rigid Contact

Initially, the 2D model began with two Ti-6Al-4V components (1.25mm X 1.00mm) with BG (0.50mm) between them. The BG and Ti-6Al-4V share a common line as a rigid interface. This 2D model was devised as the midline cross-sectional representation of the full 3D model. FM1000 was neglected for reasons that theoretically, adhesives are to have a thickness of zero. Also, the FM1000 was not used in the mechanical tests to enhance the bond strength. The serendipity 8-node quadralateral element was used in the entire model. A graded mesh was decided upon such that it was much finer near the free interface corners since these are the areas where singular fields were expected. The element mesh density was adjusted iteratively, by varying the mesh density parameter which permits the defining of element sizes at given keypoints of the analysis domain. The top-most surface had a total tensile load of 125N distributed across

it. The corner nodes of each element held 1/6 of the total load, the midsided nodes carried 2/3 of the total load, and the common node shared between two elements sustained 1/3 of the total load. This is in accordance with the isoparametric load distributions for quadratic elements.

Another 2D model was generated with the BG layer only 150μm in height. In order to reduce the problem size, the two Ti-6Al-4V regions were reduced from 1.25mm to 4233μm long. This second 2D model opened questions which inspired the performance of the following tests. The first test was created where the BG layer was set to either 0.5mm or 0.05mm and the Ti-6Al-4V was kept at 1mm. This test was designed to reveal any geometric effects on the stress distribution. Another test was done where the material properties of the BG and Ti-6Al-4V were interchanged. The purpose of this test was to examine how the material properties may effect the singular fields with stress jumps. A third test in which all three areas were of one material; either all Ti-6Al-4V or all BG was performed. All three sets of tests had their models constrained in the y direction along the entire bottom-most surface. Only the center node on the bottom surface, however, was constrained in the x direction to allow for deformation due to the elongation. The top surface of each model had a uniform surface pressure load of 30MPa applied.

The final 2D model resulted from the previous tests that were run. A 2D rigid contact model with the center region consisting of BG 150μm long and both Ti-6Al-4V were 4233μm in length. Figure 3.16 represents the element mesh with the constraints and surface pressure as seen in the previous tests. The element mesh was generated with the requirement that the outer edges of each area were divided into the number and size of elements desired. With this, the number of elements through the BG thickness was under strict control with four uniform elements along the length. Also, the element mesh throughout both Ti-6Al-4V regions became progressively finer as they approached the BG interface. The number of nodes and elements generated were 18715 and 6622, respectively.

This particular model was chosen to include a BG region of 150μm long in order to make a comparison with published experimental mechanical bond strength tests that

were performed with this BG coating thickness. A tensile pressure load of 30MPa was selected from the literature where the bond strength was observed as being between 30 - 32MPa.

3.3.2.2 3D Rigid Contact

The initial 3D model began with modeling the entire cylinder similar to that tested experimentally (Figure 3.17). After many iterations of reducing the problem size, the 3D model chosen was a Ti-6Al-4V maximum length of 4233μm with BG 150μm long. First, the angle of the cylinder was reduced by various magnitudes and eventually, the model was further reduced to a symmetric model. This was accomplished by bisecting the three volumes transversely through the midline of the BG layer. This model had varying angles from 10° to 90° and Ti-6Al-4V lengths between 338μm to 4233μm.

The first element type attempted was a 10-noded tetrahedral, however, the element type chosen was an 8-noded brick element. Again, a graded mesh approach was used for which the mesh densities were progressively finer as the interface was approached. Figure 3.18 and 3.19 show the element plots of the 10° and 80° cylinder models. The number of nodes and elements generated were 3472 and 2880, respectively.

All of the nodes on the bottom-most surface, be it the bottom surface of Ti-6Al-4V or the midline of the BG, were constrained in the z direction which was the direction of the active load. As in the 2D model, only one node was further constrained in both the x and the y directions to eliminate zero energy nodes, hence a sufficient constraint condition. This node was at the origin which represents the center of the base of the specimen. The top surface was then loaded with a uniform surface pressure of -30MPa. The negative pressure signified that the pressure was under a tensile mode. The solution was applied in one load step and as a linear elastic model due to the fact that BG was the weaker of the two materials and behaves in a linear elastic, brittle manner.

3.3.2.3 3D Rigid Contact: Three Volume

The final model was a 10° cylinder that had the full 150μm BG region with the two Ti-6Al-4V volumes at 450μm in length. Again, this model was meshed with 8-noded brick elements and with the mesh density finer towards the two interfaces (Figure 3.20). This three-volume model was constrained and loaded in the same fashion as the symmetric 3D rigid contact model.

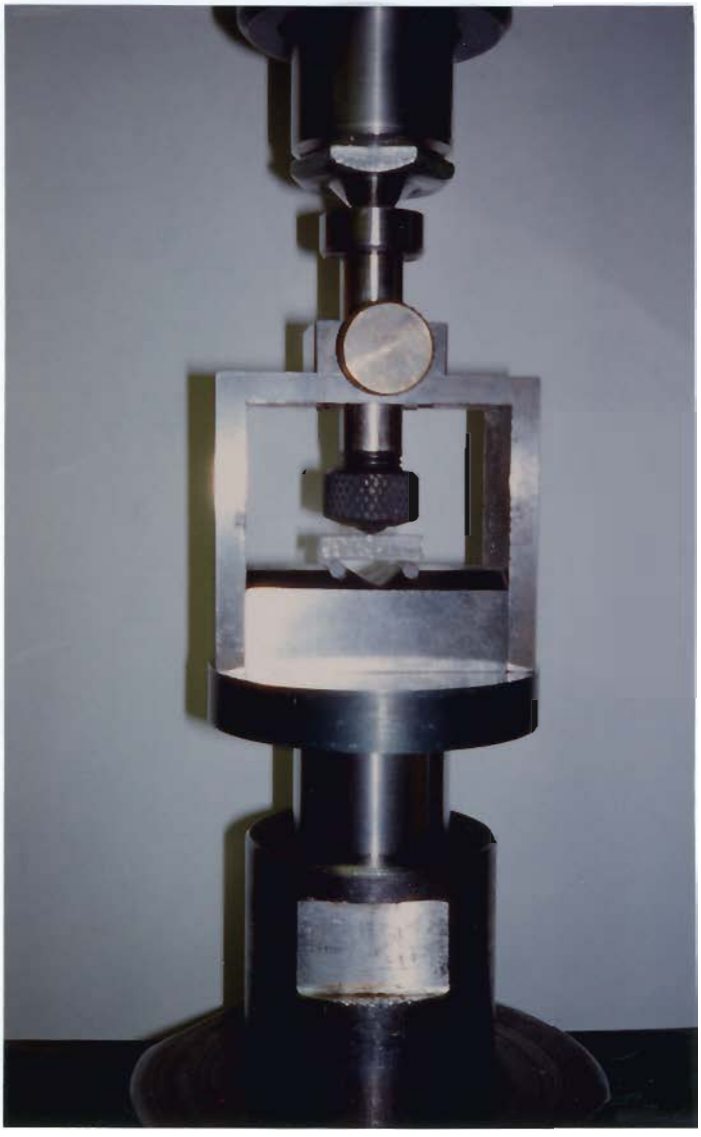

Figure 3.1 Modulus of rupture three-point bend test.

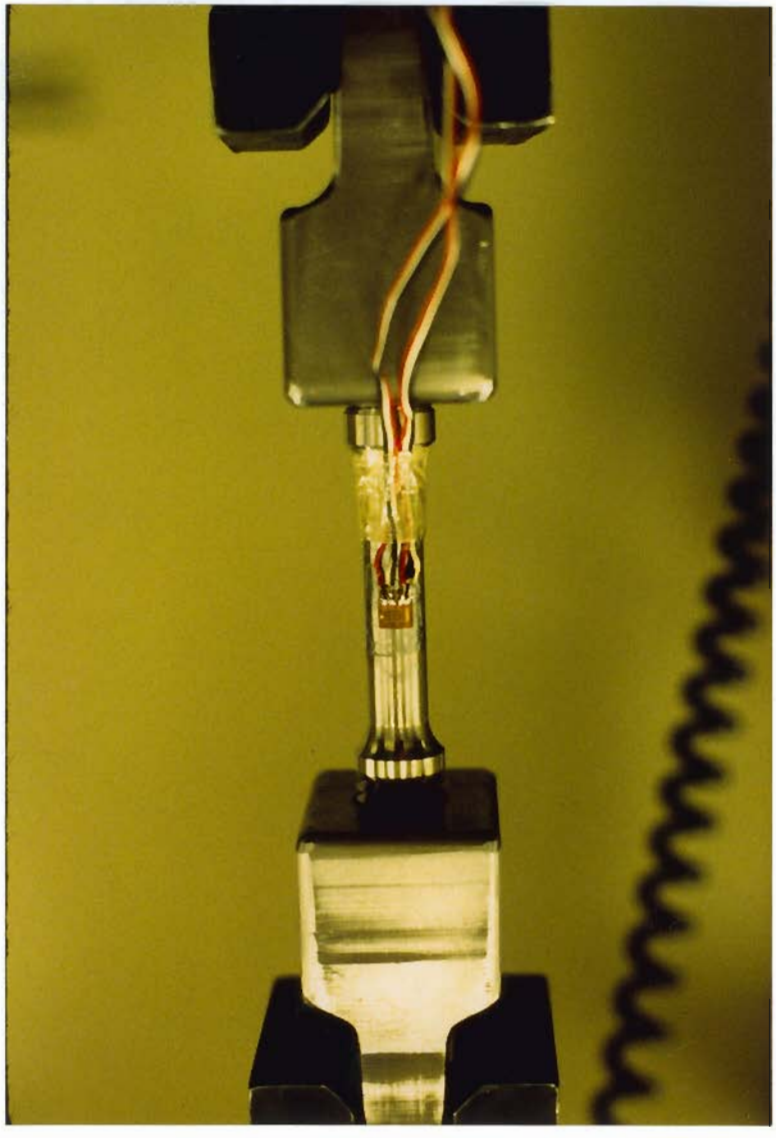

Figure 3.2 Ti-6Al-4V tensile test using a 90° rosette strain gage.

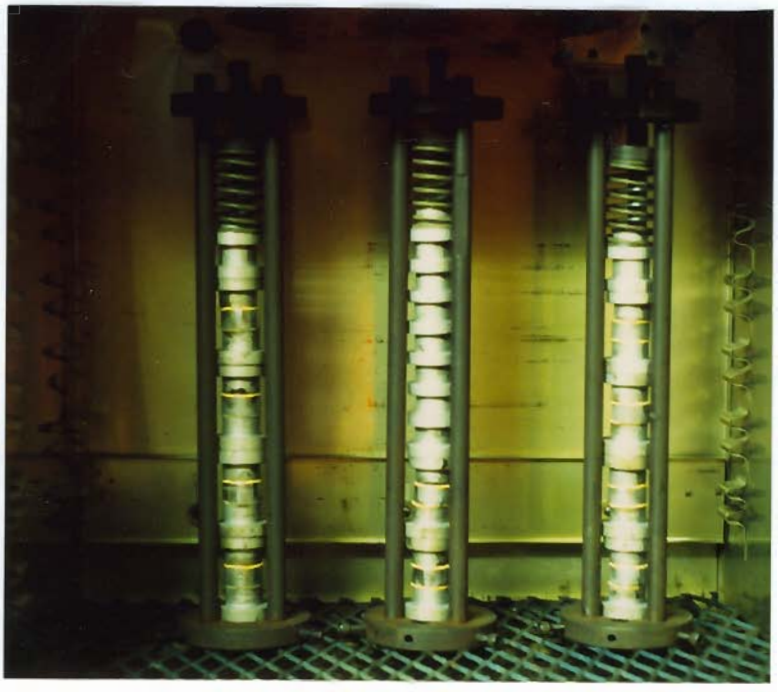

Figure 3.3 Curing apparatus for bond strength tensile test specimens.

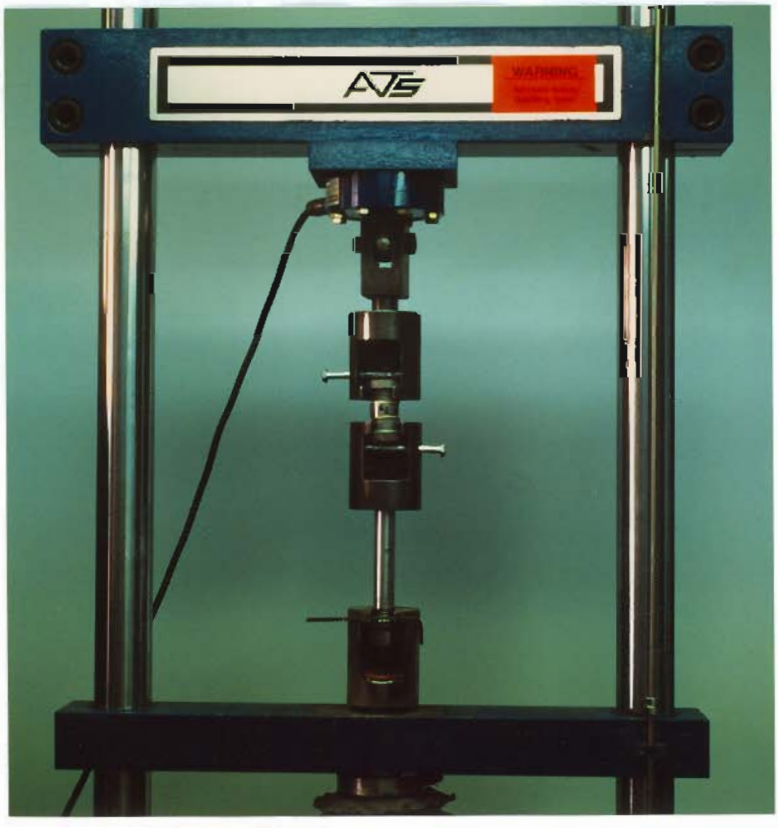

Figure 3.4 Tensile test for bond strength of plasma-sprayed BG on Ti-6Al-4V.

(a)

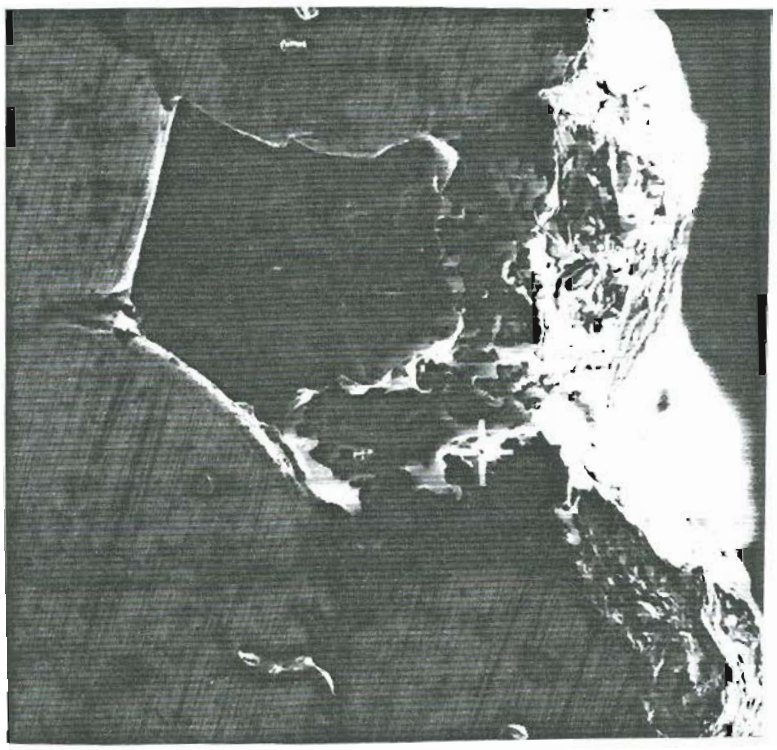

(b)

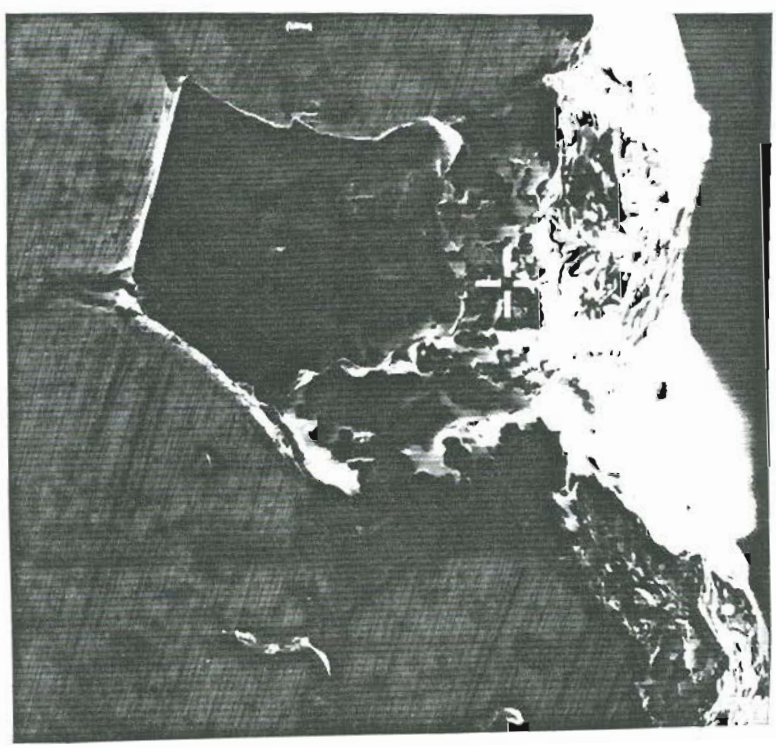

Figure 3.5 (a) and (b) Images (10kV, 100X) of two locations on an unpolished porous-75μm BG sample.

(a)

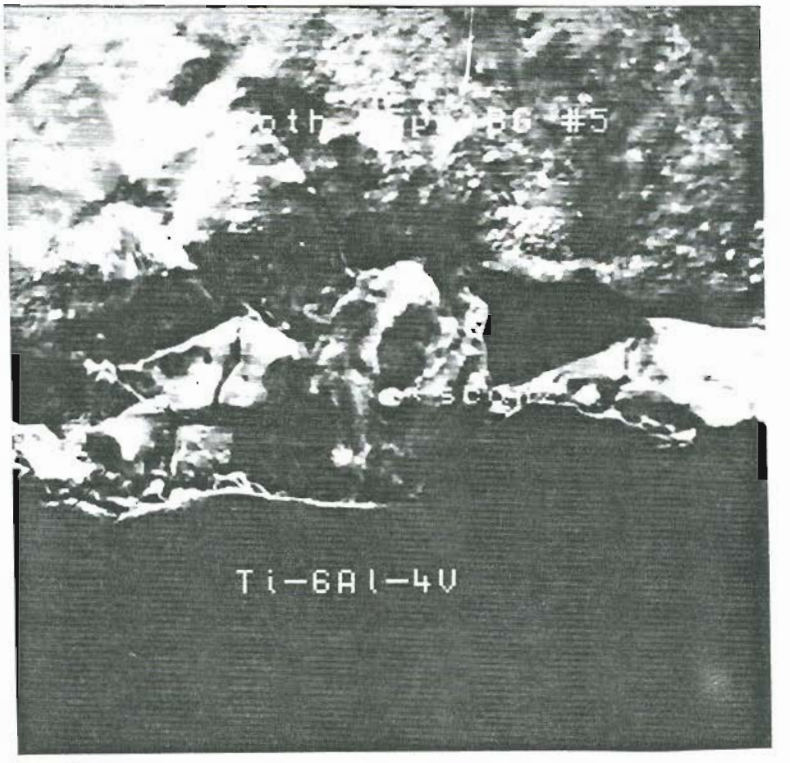

(b)

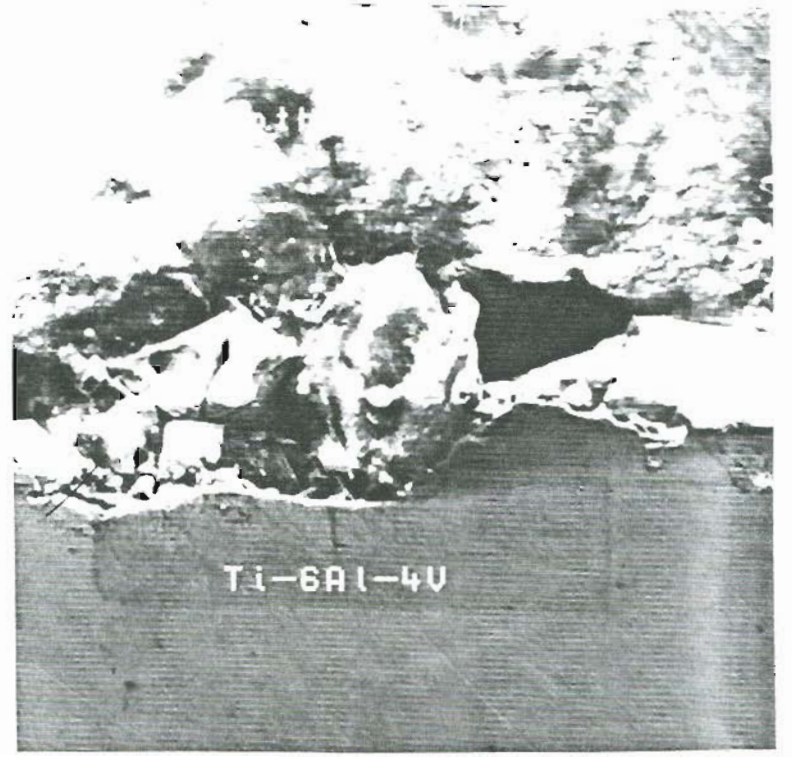

Figure 3.6 (a) and (b) Images (10kV, 500X) of two locations on a polished smooth-75μm BG sample.

(a)

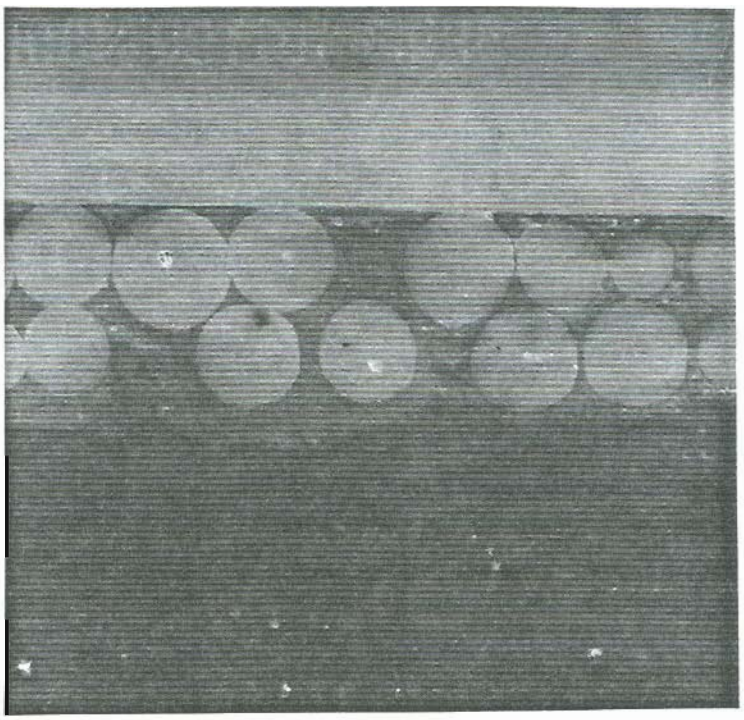

(b)

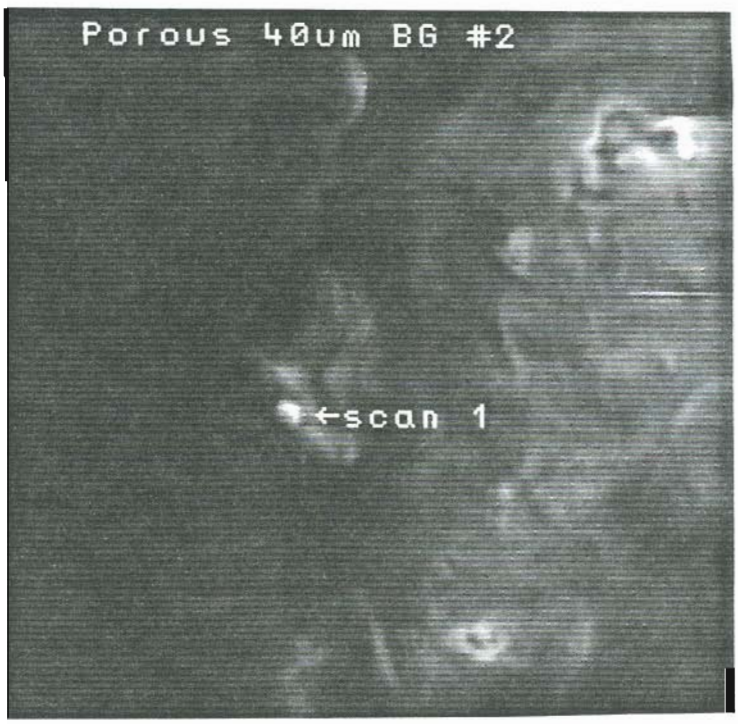

Figure 3.7 (a) Image (10kV, 20X) of polished porous-40μm BG sample showing beads and (b) Image (10kV, 5000X) of polished porous-40μm BG sample.

(a)

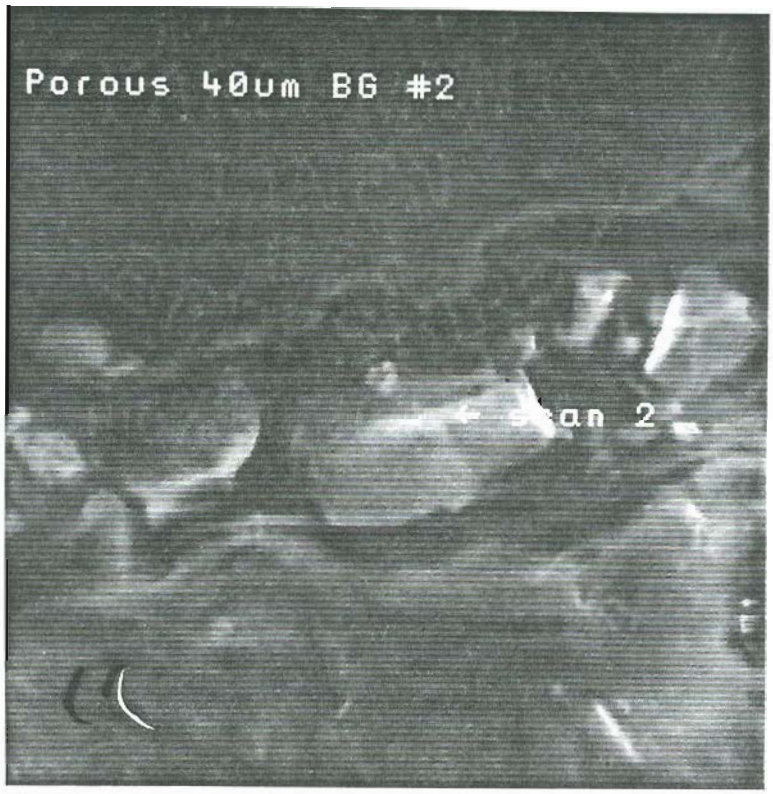

(b)

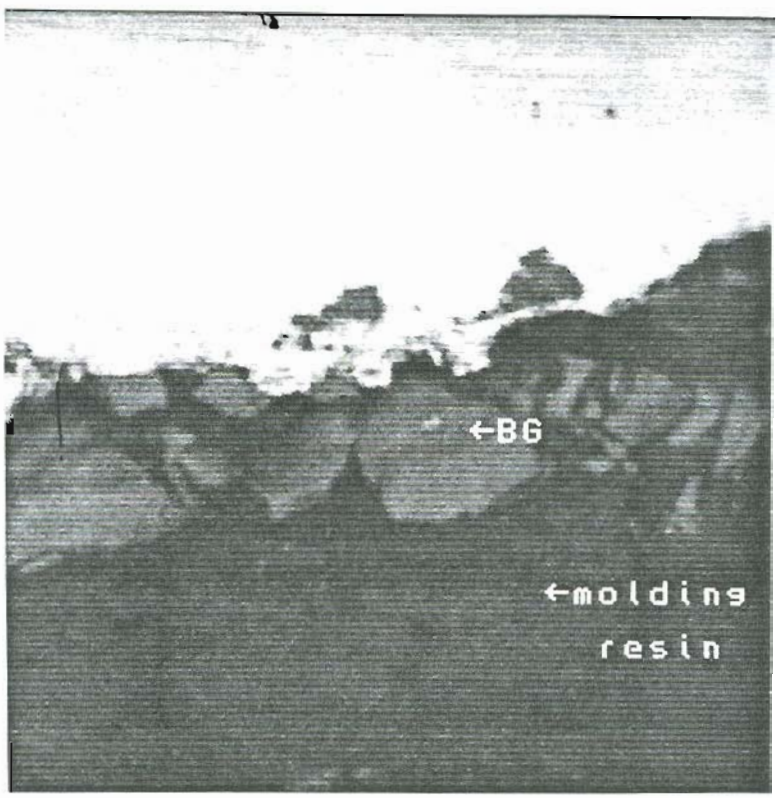

Figure 3.8 (a) Image (10kV, 3000X) of polished porous-40μm BG sample and (b) Image (10kV, 2000X) of same region but with BSE detector.

(a)

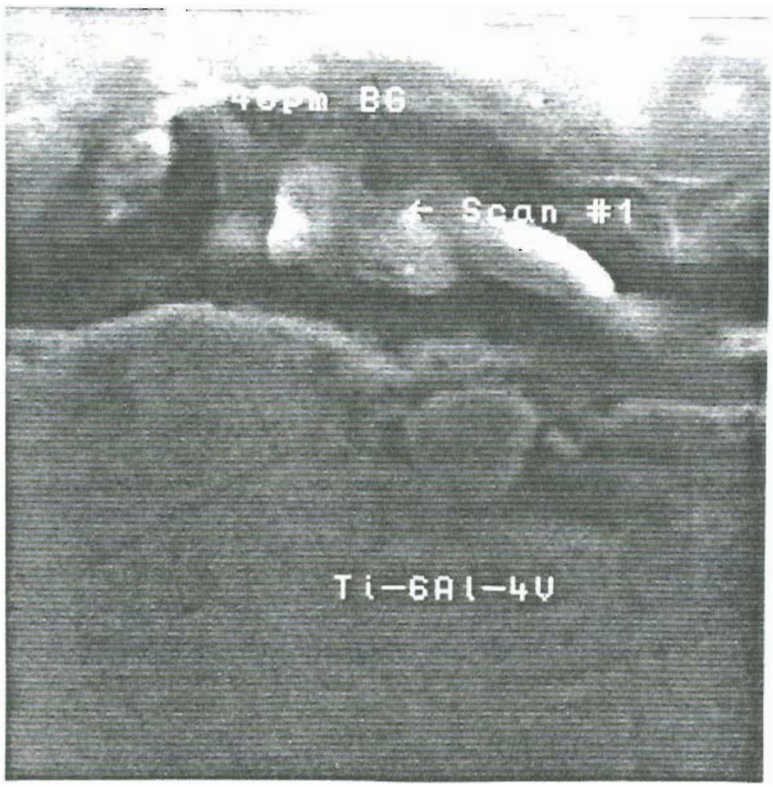

(b)

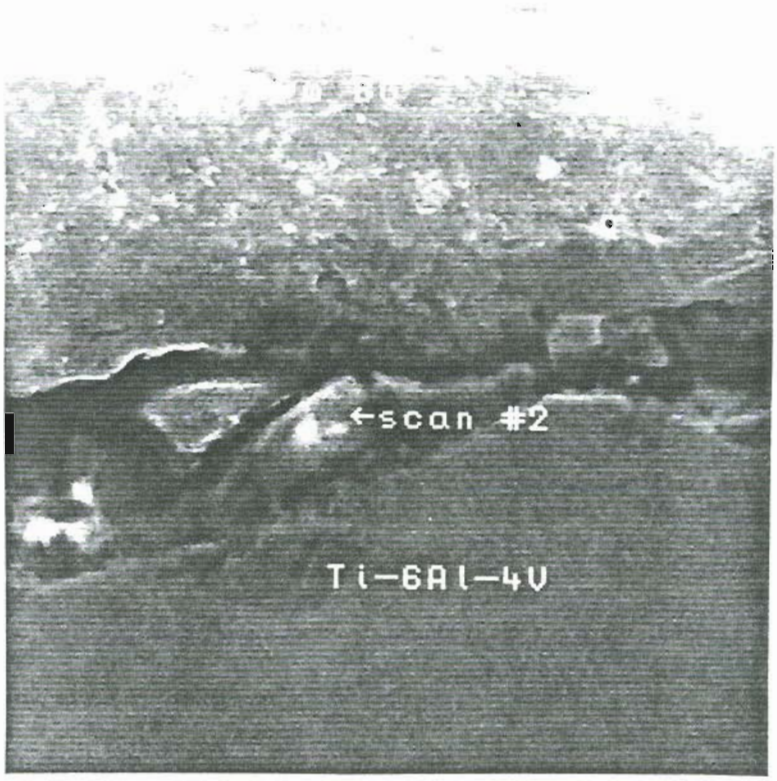

Figure 3.9 (a) Image (10kV, 5000X) and (b) Image (10kV, 2000X) of two locations on a polished smooth-40μm BG sample.

(a)

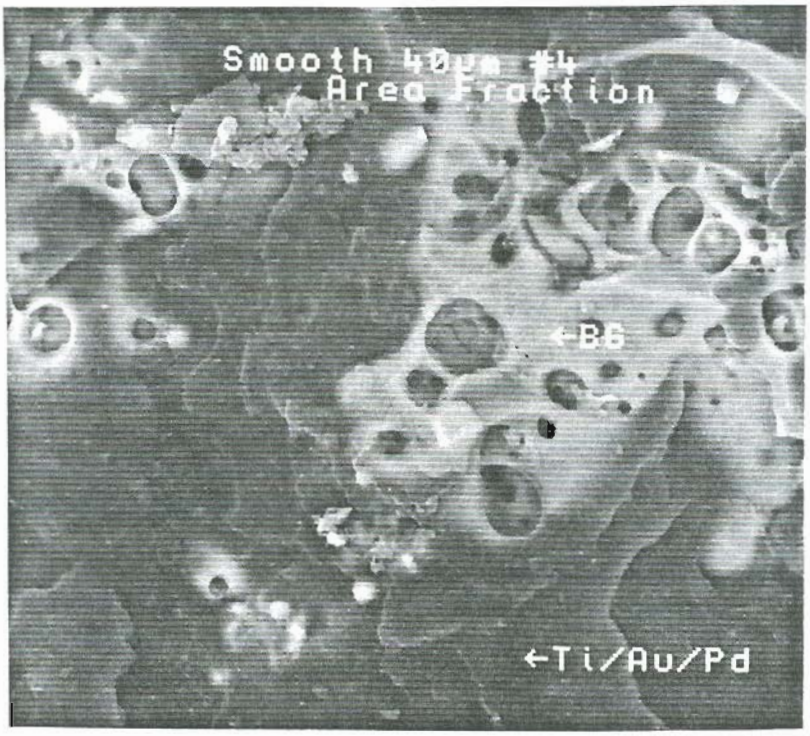

(b)

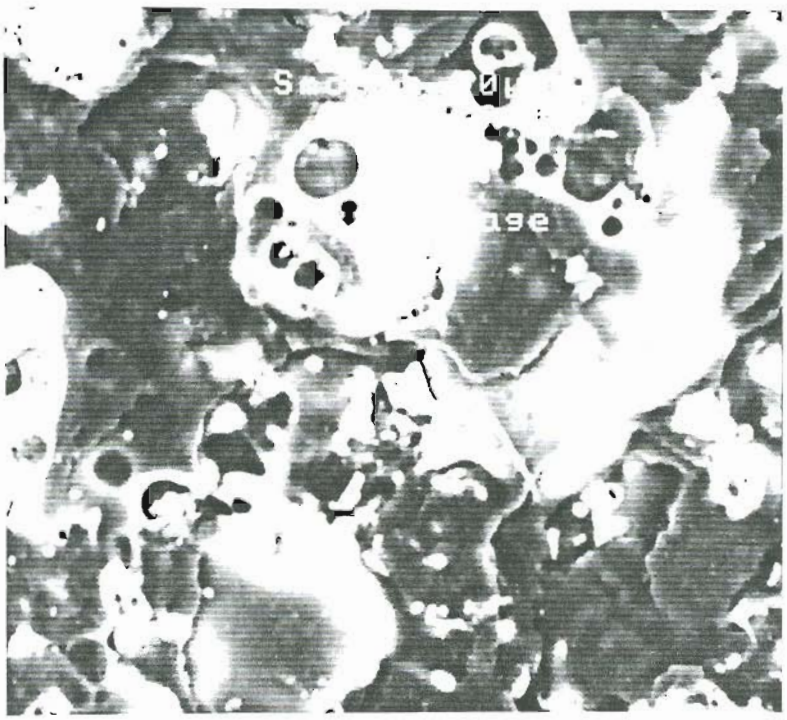

Figure 3.10 (a) Secondary electron image (20kV, 1000X) of smooth-40µm BG sample showing areas of BG and Ti-6Al-4V and (b) Same image (20kV, 500X) under BSE.

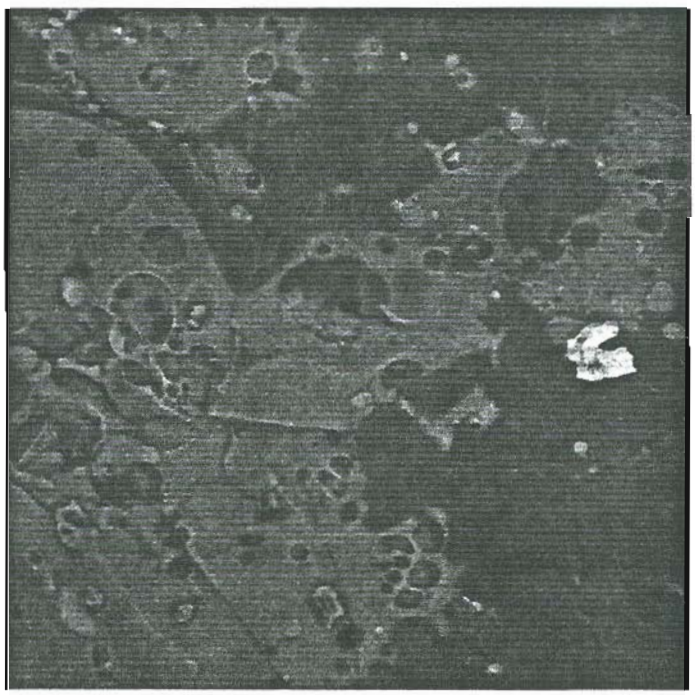

Figure 3.11 BSE image of fracture surface of smooth-40μm BG sample for area fraction measurement.

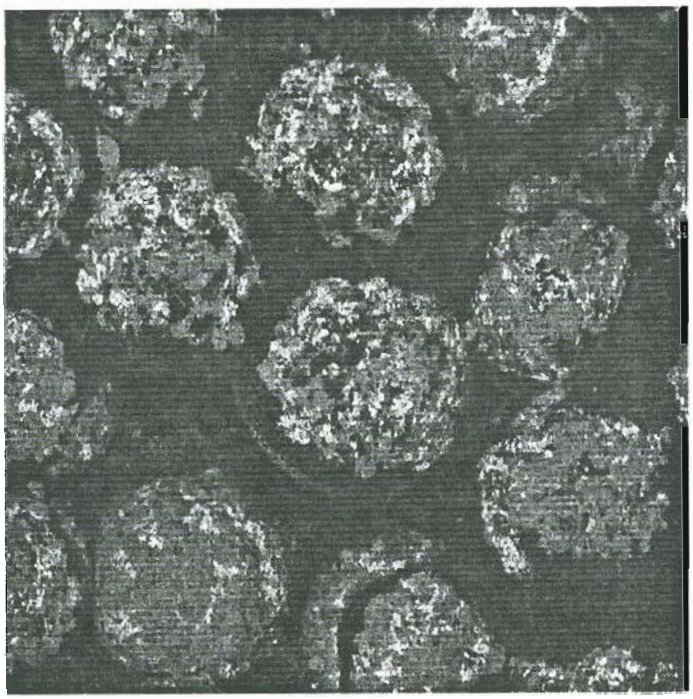

Figure 3.12 BSE image of porous-40μm BG sample for area fraction measurement.

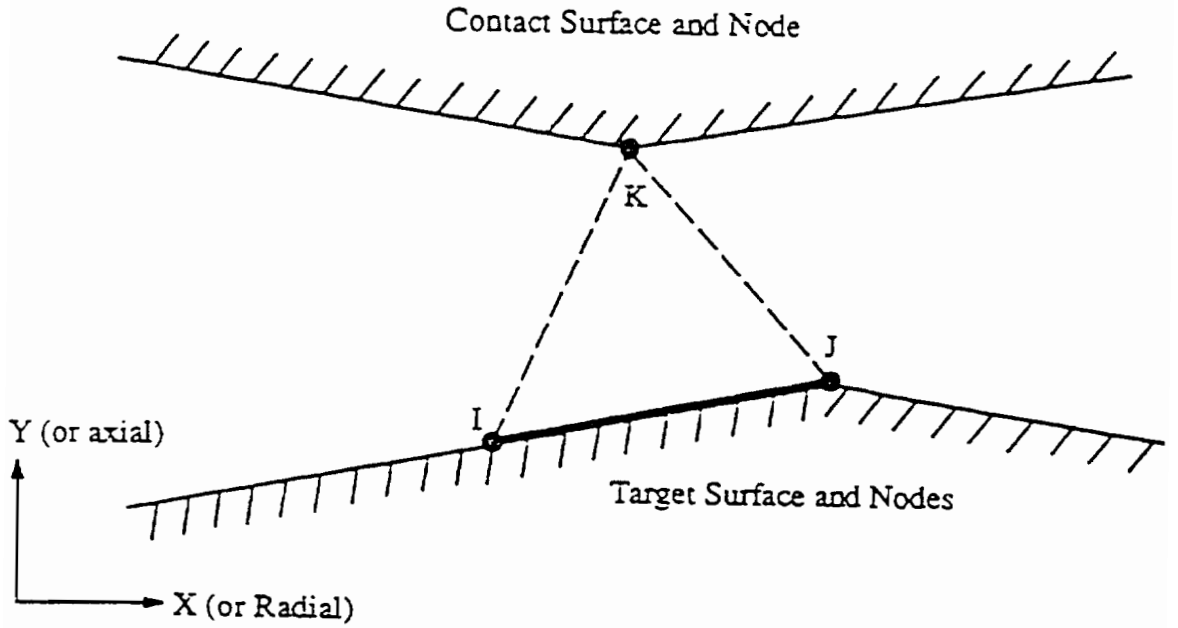

Figure 3.13 2D point-to-surface contact element.

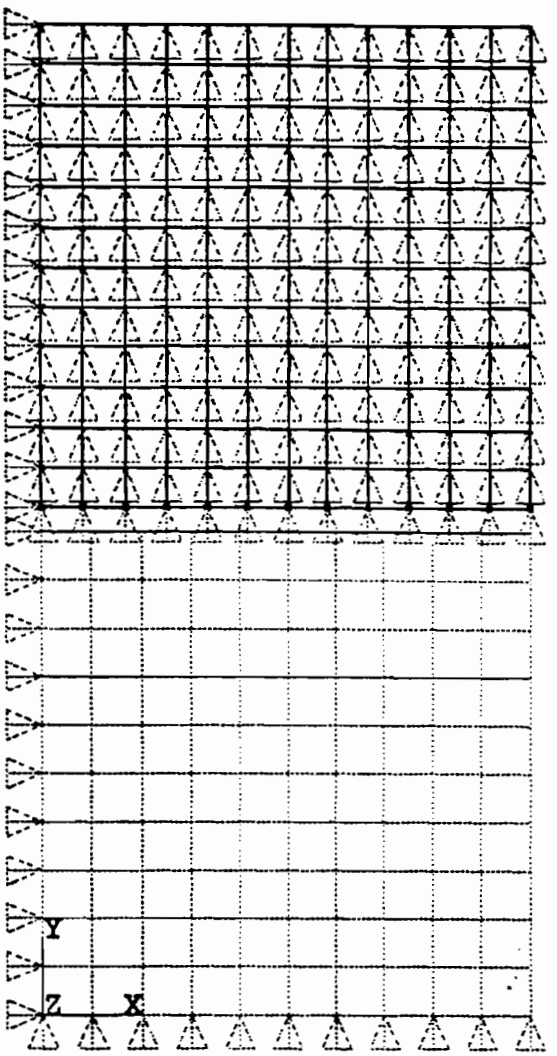

Figure 3.14 Element plot of prescribed displacement contact model.

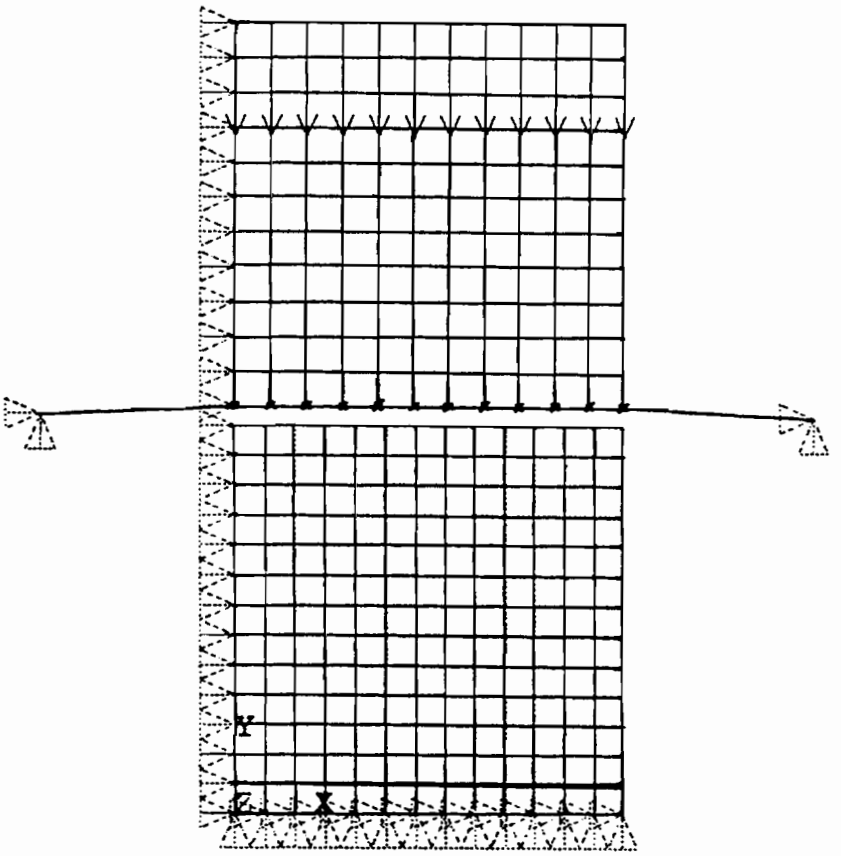

Figure 3.15 Element plot of compressive point-load with initial gap contact model.

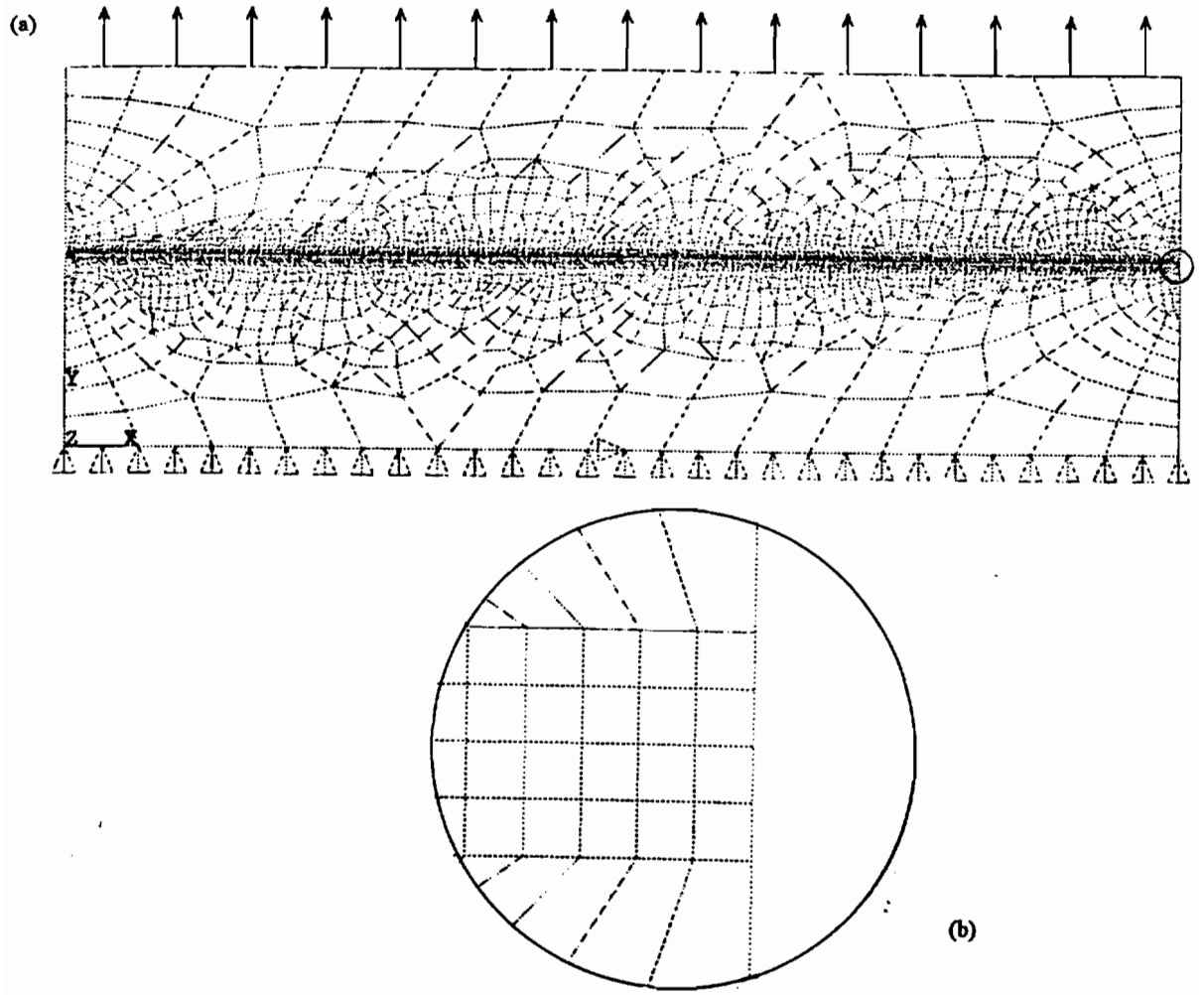

Figure 3.16 (a) Element plot of 2D rigid contact model and (b) Zoomed element plot showing a four element thickness through the BG area.

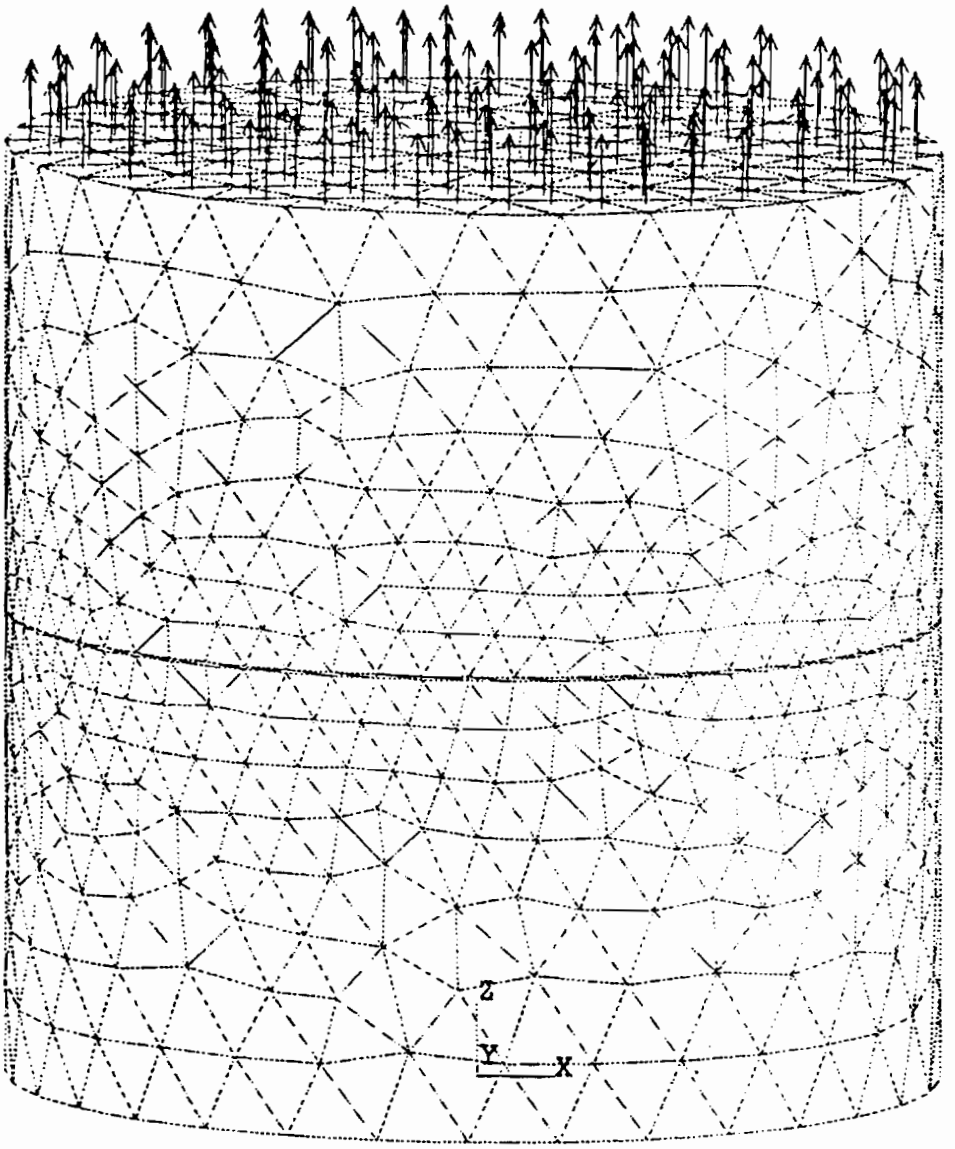

Figure 3.17 3D element plot of entire 360° cylinder.

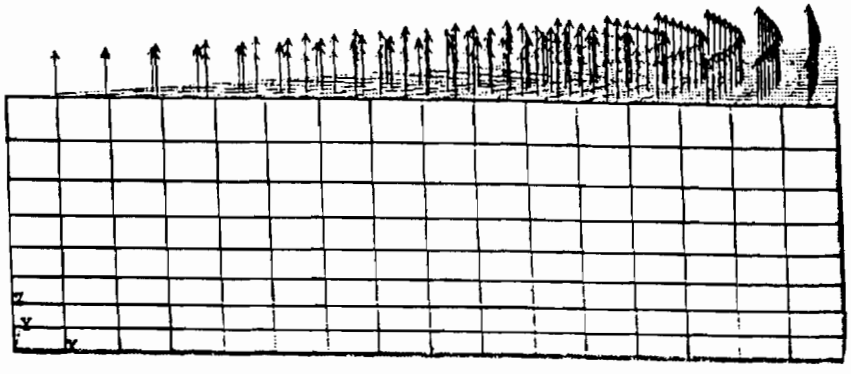

Figure 3.18 Element plot of 10° cylinder.

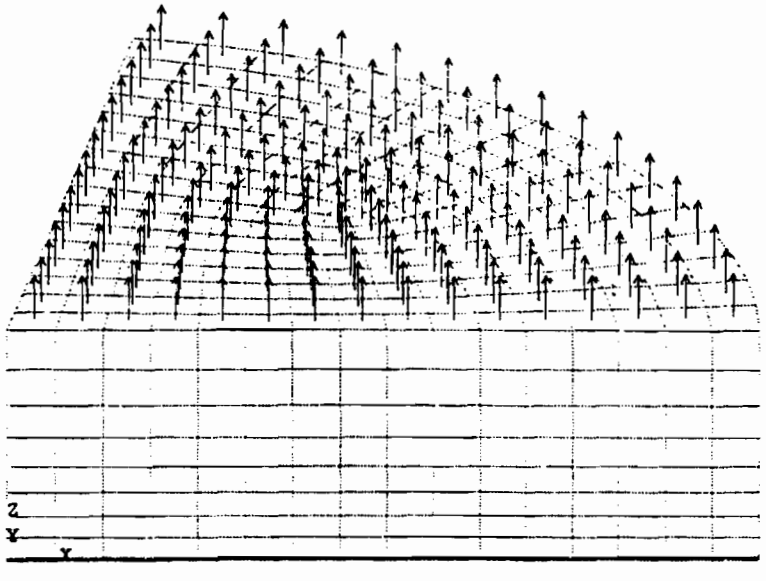

Figure 3.19 Element plot of 80° cylinder.

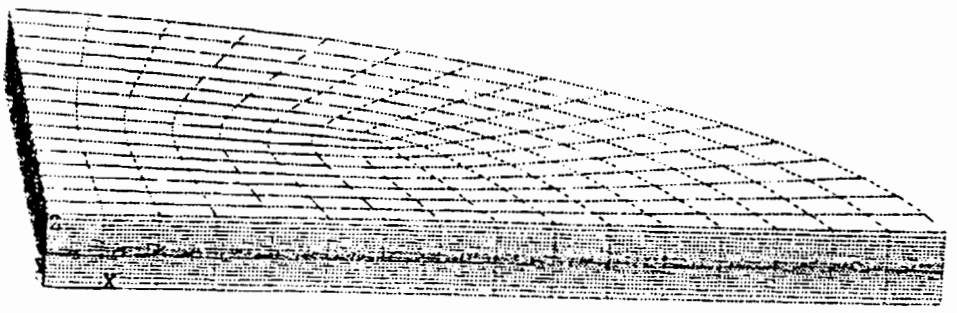

Figure 3.20 Element plot of 3D, three volume model.

CHAPTER 4

RESULTS

4.1 Mechanical Test

4.1.1 Modulus Of Rupture

Sixteen modulus of rupture specimens, 5mm X 5mm X 20mm in dimensions, were tested and analyzed statistically for the three-point bend test. Figure 4.1 illustrates the modulus of rupture for each sample. The representative average and standard deviation for the given samples were calculated to be 48.14±15.23 MPa.

4.1.2 Ti-6Al-4V Tensile Test

Three standard tension test specimens were tested and analyzed statistically for the ultimate tensile strength (UTS), Young's modulus (E), and Poisson's ratio (υ). Figure 4.2 shows the load versus displacement curve for the first specimen tested. Table 4.1 shows the UTS, E, and υ for all three specimens with the average and standard deviation. The representative average and standard deviation of E and υ are 12389±496 MPa and 0.314±0.01, respectively.

4.1.3 Bond Strength Test

The porous specimens with a 75μm BG coating had a sample size of 11, whereas the porous samples with a 40μm BG coating had a sample size of 8. The smooth coupons had 4 and 6 specimens for 75μm and 40μm BG coating, respectively. Table 4.2 shows the average and standard deviation for the bond strength of porous and smooth coupons with 75μm and 40μm BG coatings.

4.2 Scanning Electron Microscopy (SEM)

4.2.1 Secondary Electron

Figure 4.3 shows the fracture surface of a BG MOR specimen. Note the concentric "rings" protruding towards the tensile surface of this three-point bend specimen. At higher magnifications, raised particulate-like features are shown to contribute the formation of the "rings". Also, when these features are examined under a backscatter detector, it appears as though they are of a different composition or atomic number/Z value (Figure 4.4). The smooth polished, unfractured BG surface seen in Figure 4.5 shows that this ceramic is a homogenous material. Figure 4.6 shows the cross-section of the plasma-sprayed BG on Ti that was used as practice for the coating technique. The standard EDS spectra of BG that was collected from the practice plasma-spray sample is shown in Figure 4.7.

Figure 4.8 illustrates the fracture surface of the Ti-6Al-4V tensile specimen which shows shear lips around the edges. Higher magnification reveals the topography of the fracture surface.

The EDS spectra of both scans from the cross-section of the smooth-75μm BG bond strength test sample are shown in Figures 4.9 and 4.10. Note that scan 2 shows signs of the Ti-6Al-4V. The unpolished porous-75μm sample yielded a less clear spectrum, however, signs of BG, Ti-6Al-4V, and additional unexpected elements were seen (Figure 4.11). The backscatter electron detector clearly showed the different

composition of the BG, Ti-6Al-4V, and the molding resin, in which the specimen was potted, for the cross-section of the porous-40μm BG (Figure 3.8). The EDS spectra for this specimen are shown in Figures 4.12 and 4.13 with peaks indicating an obvious prevalent existence of BG. The EDS spectra for the smooth-40μm BG specimen are presented in Figures 4.14 and 4.15. Note that scan 1 shows signs of the Ti-6Al-4V. Areas of the cross-sectioned specimens that still had BG adhered to them, were on average ~5μm in thickness.

4.2.2 Backscatter Electron

The EDS spectra differentiating the BG regions from the Ti-6Al-4V or FM1000 are shown in Figures 4.16 and 4.17 for the smooth-40μm and Figures 4.18 and 4.19 for the porous-40μm specimens. The average and standard deviation of the area fraction taken from the thirty fields of the smooth-40μm BG sample is 63%. The porous-40μm BG specimen yielded an average and standard deviation of 94%.

4.3 Finite Element Analysis (FEA)

4.3.1 Contact Theory

4.3.1.1 Prescribed Displacement

Figure 4.20 shows that the prescribed displacement was sufficient to bring the two square areas together.

4.3.1.2 Compressive Point-Load With Initial Gap

Figure 4.21 shows that, like the prescribed displacement model, the compressive point-load model was also capable of closing the gap between the two square areas.

4.3.2 Rigid Contact

4.3.2.1 2D Rigid Contact

The final 2D model that was generated experienced transverse shrinkage and an increase in length when submitted to a tensile load (Figure 4.22). This model yielded a maximum and minimum von Mises stress values of 31.4MPa and 24.0MPa, respectively, with the greatest stress at the BG/Ti-6Al-4V free edge interfaces (Figure 4.23). These values are of the nodal solution, however, the elemental solution yielded a maximum von Mises stress of 32.2MPa. This discrepancy results from the stress averaging in the case of nodal solutions. Element-based solutions of stress are raw stresses. The equivalent stresses are graphically shown in Figure 4.24 with the sharp increase in stress being the regions of the interfaces, thus, the existence of singular zones.

Figure 4.25 shows the first principle stress at the region of interest. It shows the similarity in the "wings" with the von Mises stress. Figure 4.26 depicts the second principal stress with the highest stresses in the center of the BG area.

The first principal strain can be seen in Figure 4.27 where the highest strains exists in the center region of the BG. The second principle strain is shown in Figure 4.28 where the maximum strains are just outside of the interfaces.

4.3.2.2 3D Rigid Contact

Table 4.1 best displays the results of the von Mises stress values of all of the 3D models. The models that were constructed with the Ti-6Al-4V length as 1710μm or 450μm resulted in a "wing" of slightly lower stresses of 30.0 - 31.2MPa (Figure 4.29). These "wings" appear around the circumference towards the end of the Ti-6Al-4V furthest away from the BG interface. Only representative results will be discussed in this chapter.

Figures 4.30 show the equivalent stresses for the 10° cylinder with the Ti-6Al-4V length equal to 450μm. Note the maximum and minimum were 32.5MPa and 21.4MPa. Figure 4.31 is a graphical illustration of the equivalent stresses showing the sharp increase

at the BG/Ti-6Al-4V interface.

Figure 4.32 presents the deformation experienced by the 10° cylinder model with Ti-6Al-4V equal to 4233μm. Note the decrease in radius and increase in length. Figures 4.33 and 4.34 show the equivalent stresses for this model where the maximum and minimum values are 30.8MPa and 21.3MPa. Again, the equivalent stresses have been plotted in Figure 4.35 to show the onset of the singular zone as the interface is approached.

4.3.2.3 3D Rigid Contact: Three Volume Model

Figure 4.36 shows the deformation of the 10° cylinder with all three volumes (Ti-6Al-4V/BG/Ti-6Al-4V). Again, a decrease in radius is observed along with an increase in length. The von Mises stress contours of the area of interest, being the two BG/Ti-6Al-4V interfaces, can be seen in Figure 4.37. The maximum and minimum equivalent stresses were found to be 32.4MPa and 21.4MPa, respectively. The BG region is evident on the graph depicted in Figure 4.38 where the equivalent stresses are at a minimum and increase dramatically on either side to show the interfaces. One can see in Figure 4.39 that the equivalent stresses along the interfaces at the center axis of the cylinder are uniform with no signs of a singular field.

Table 4.1 UTS, E, and υ for Ti-6Al-4V tensile samples

Specimen	UTS (kips)	E (ksi)	υ
1	28.53	12955	0.31
2	28.73	12072	0.30
3	28.61	12121	0.33
Ave±STD	28.62±0.10	12388.75±496.2	0.32±0.012

Table 4.2 Bond strength of plasma-sprayed BG on Ti-6Al-4V

	Bond Strength (MPa)	
	75μm BG	40μm BG
Porous	36.42±8.61	43.94±4.92
Smooth	53.23±9.98	70.54±7.26

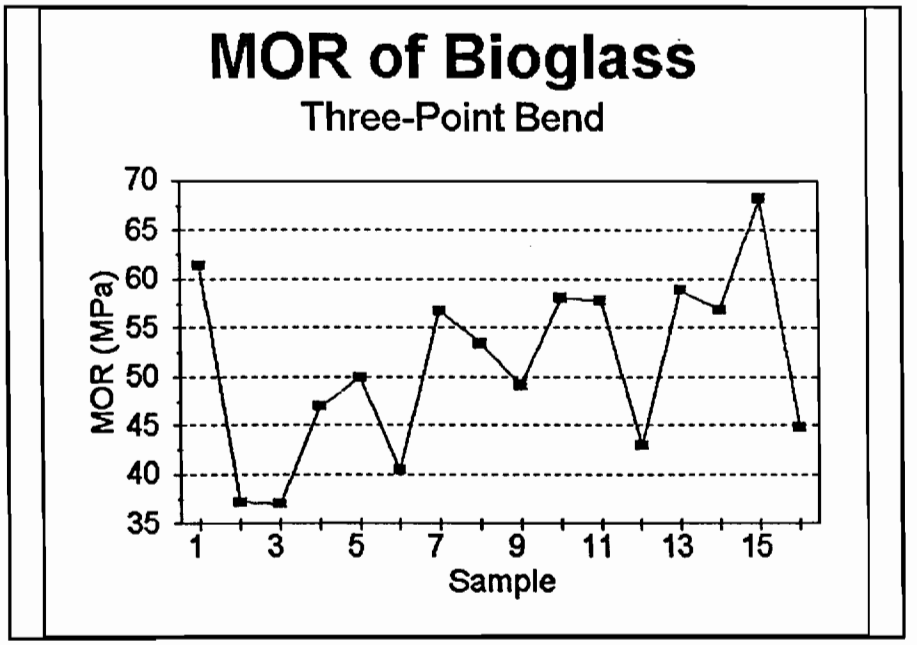

Figure 4.1 MOR values of 16 three-point bend specimens.

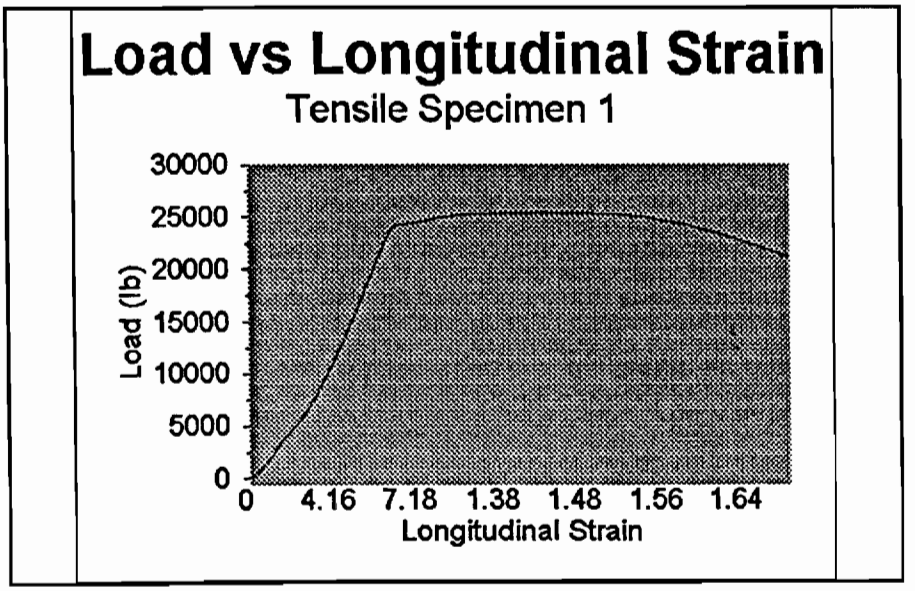

Figure 4.2 Load vs displacement for Ti-6Al-4V tensile test.

Table 4.3 Maximum equivalent stress values for 3D models

			maximum von Mises Stresses (MPa)				
			Ti-6Al- 4V Length				
Angle	338μm	450μm	1710μm	2970μm	4230μm	4233μm	3 vol.
10°		32.5	***	***	***	30.8	32.4
20°	***	***	***	***	***	30.8	***
30°	***	***	***	***	***	30.8	***
40°	***	***	***	***	***	30.8	***
50°	***	***	***	***	***	30.8	***
60°	***	***	***	***	***	30.8	***
70°	***	***	***	***	***	30.8	***
80°	***	32.2	31.3	30.9	30.8	30.8	***
90°	***	32.2	***	***	***	30.8	***

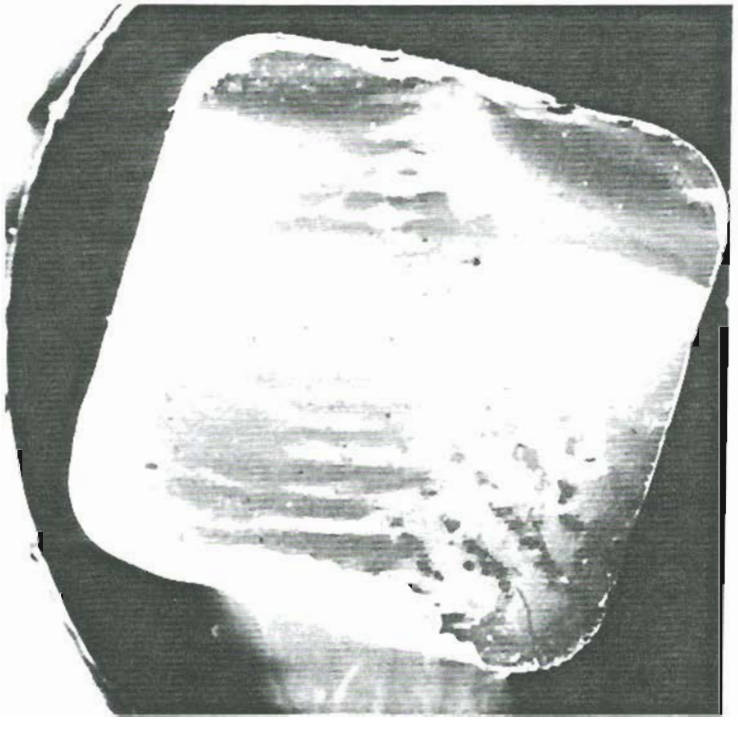

Figure 4.3 Fracture surface of BG MOR specimen.

Figure 4.4(a) Enlarged region of the fracture surface of a BG MOR specimen, secondary electron image.

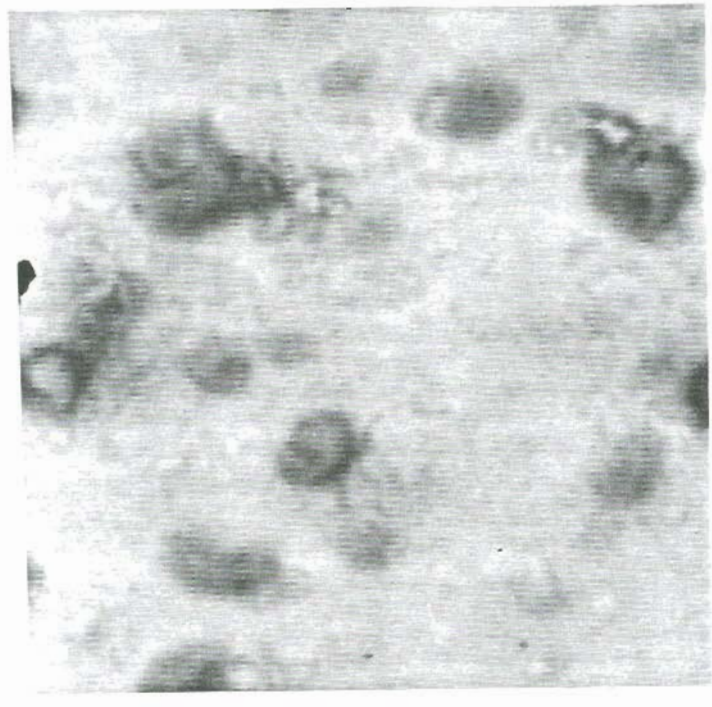

Figure 4.4(b) Same field as Figure 4.4(a) Backscatter Electron image.

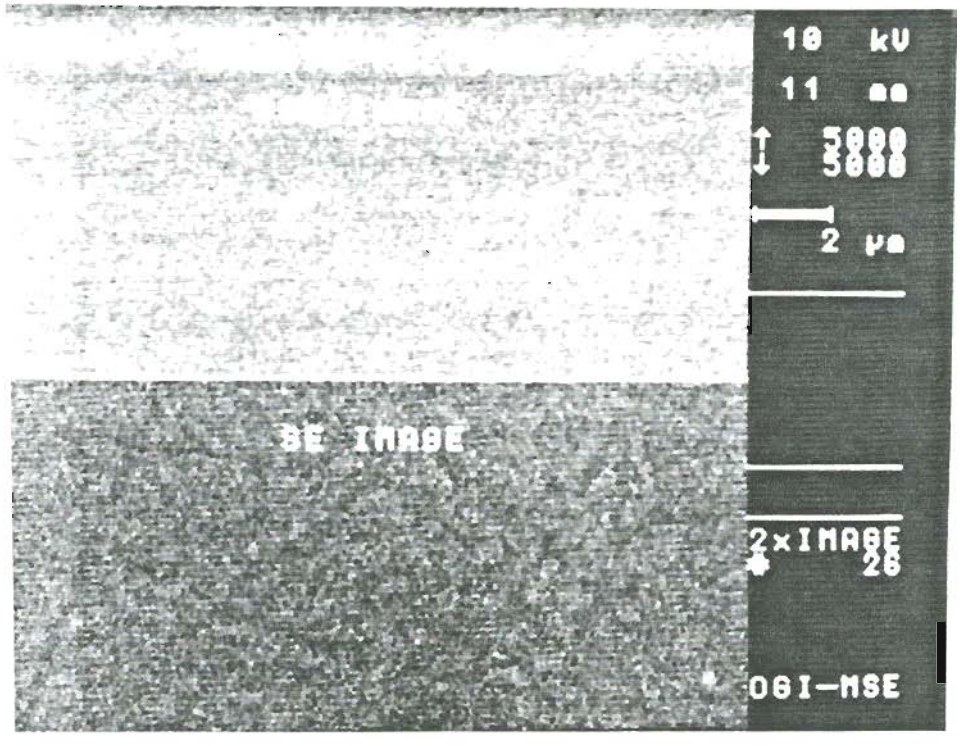

Figure 4.5 Secondary and backscatter electron images of an unfractured surface of BG.

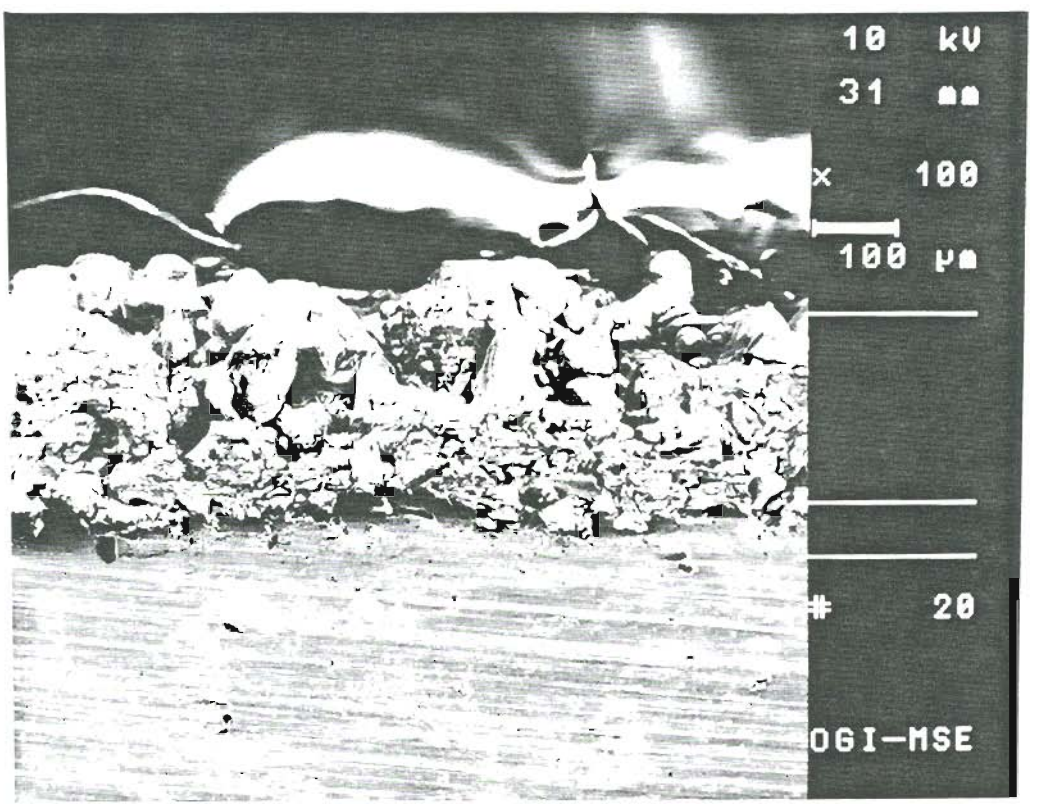

Figure 4.6 Cross-sectional secondary electron image of the practice plasma-sprayed BG on Ti.

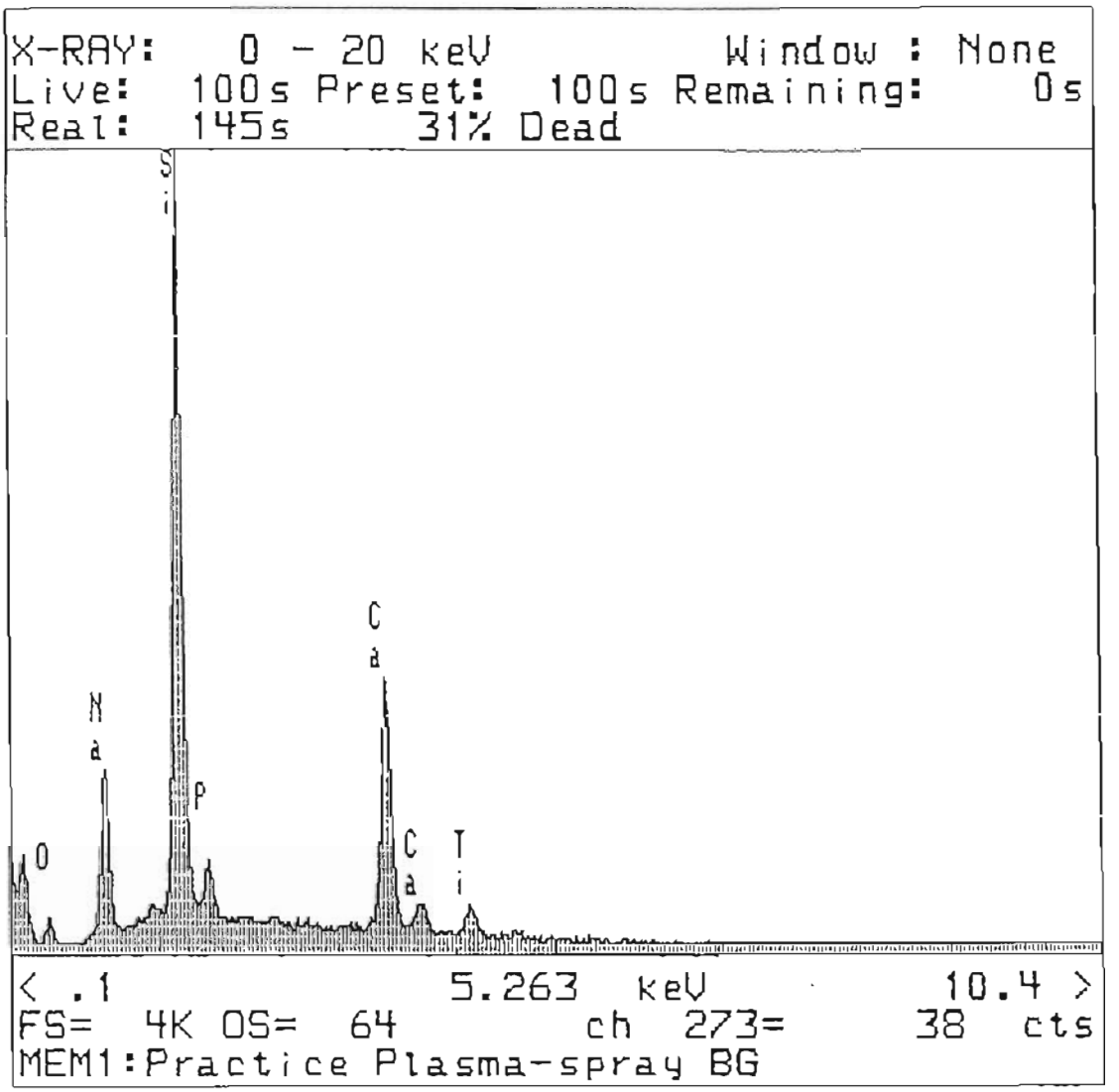

Figure 4.7 EDS spectrum of BG.

(a)

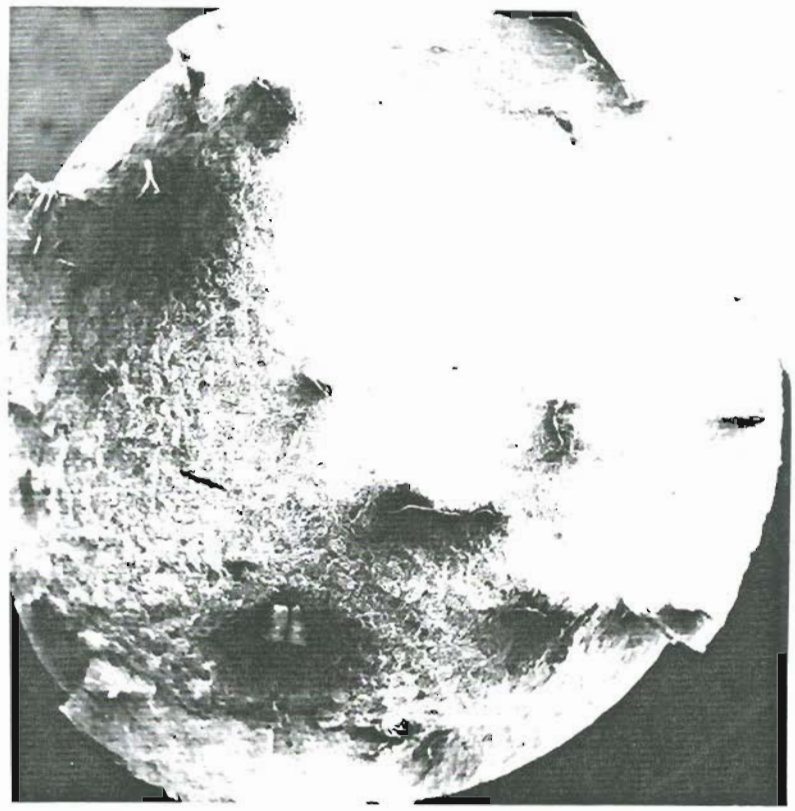

(b)

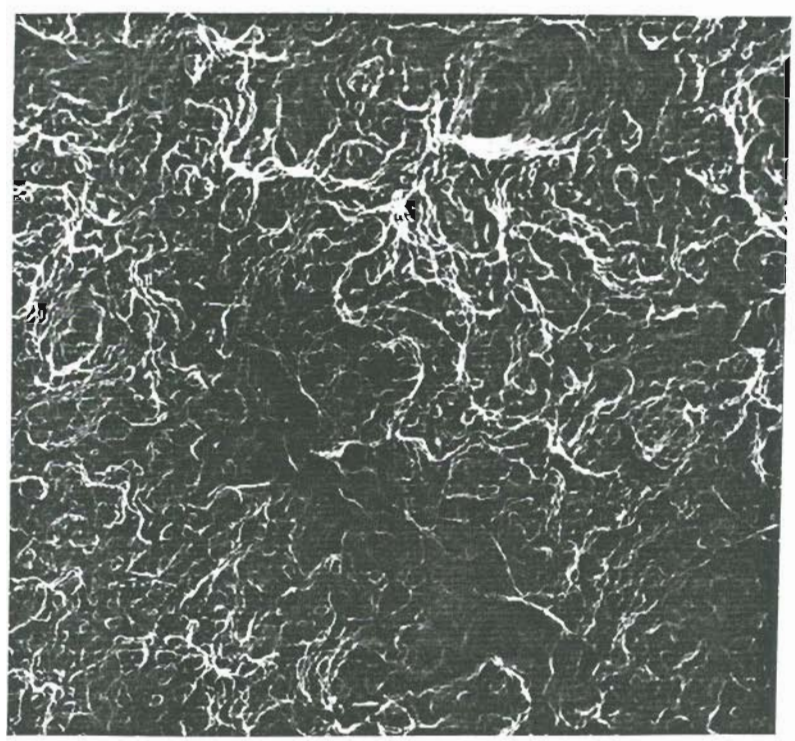

Figure 4.8 (a) Image (10kV, 10X) of global view of Ti-6Al-4V tensile specimen fracture surface and (b) Same specimen magnified to 100X.

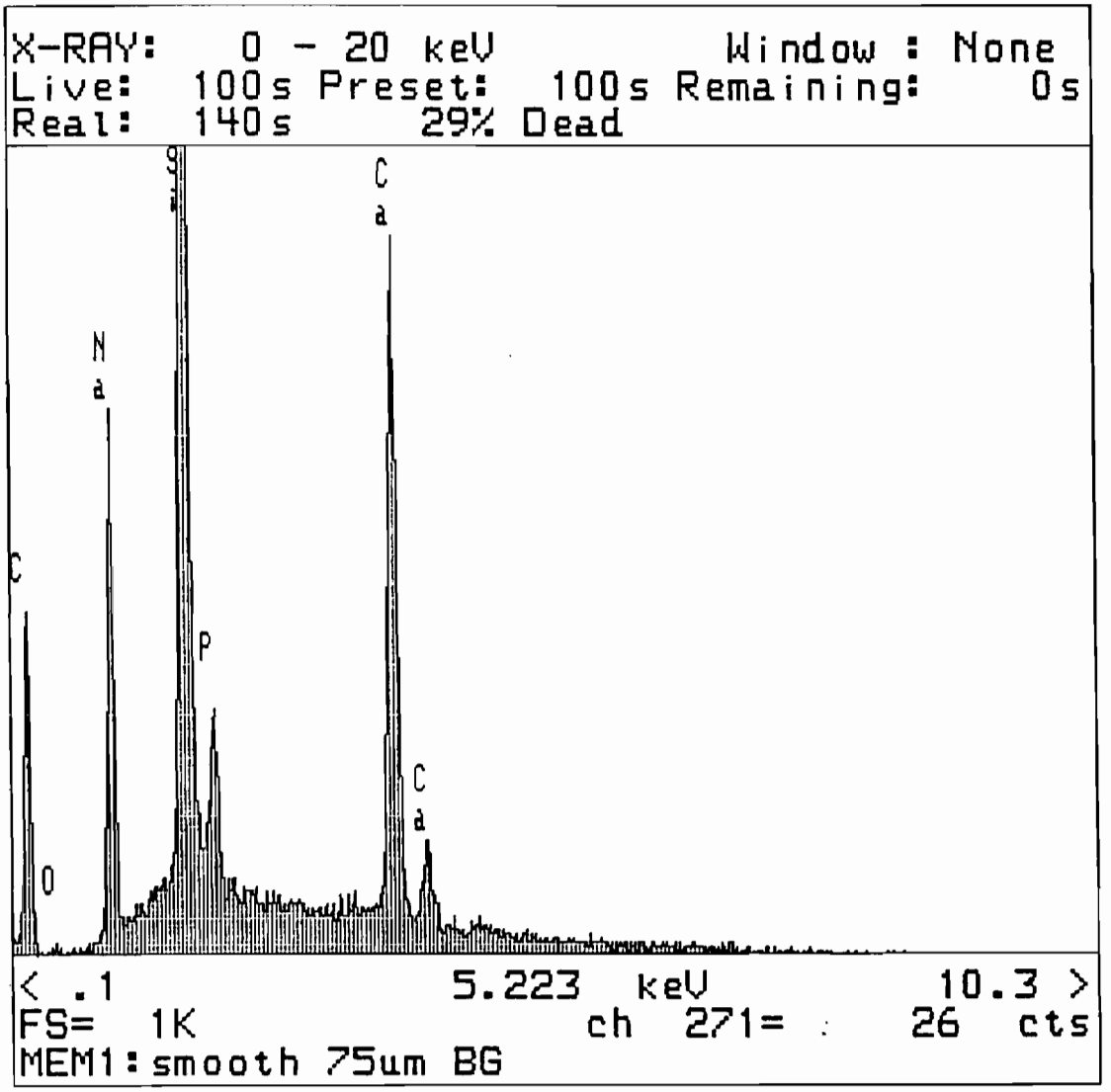

Figure 4.9 First EDS spectrum of BG on the polished cross-section of a smooth-75μm BG specimen.

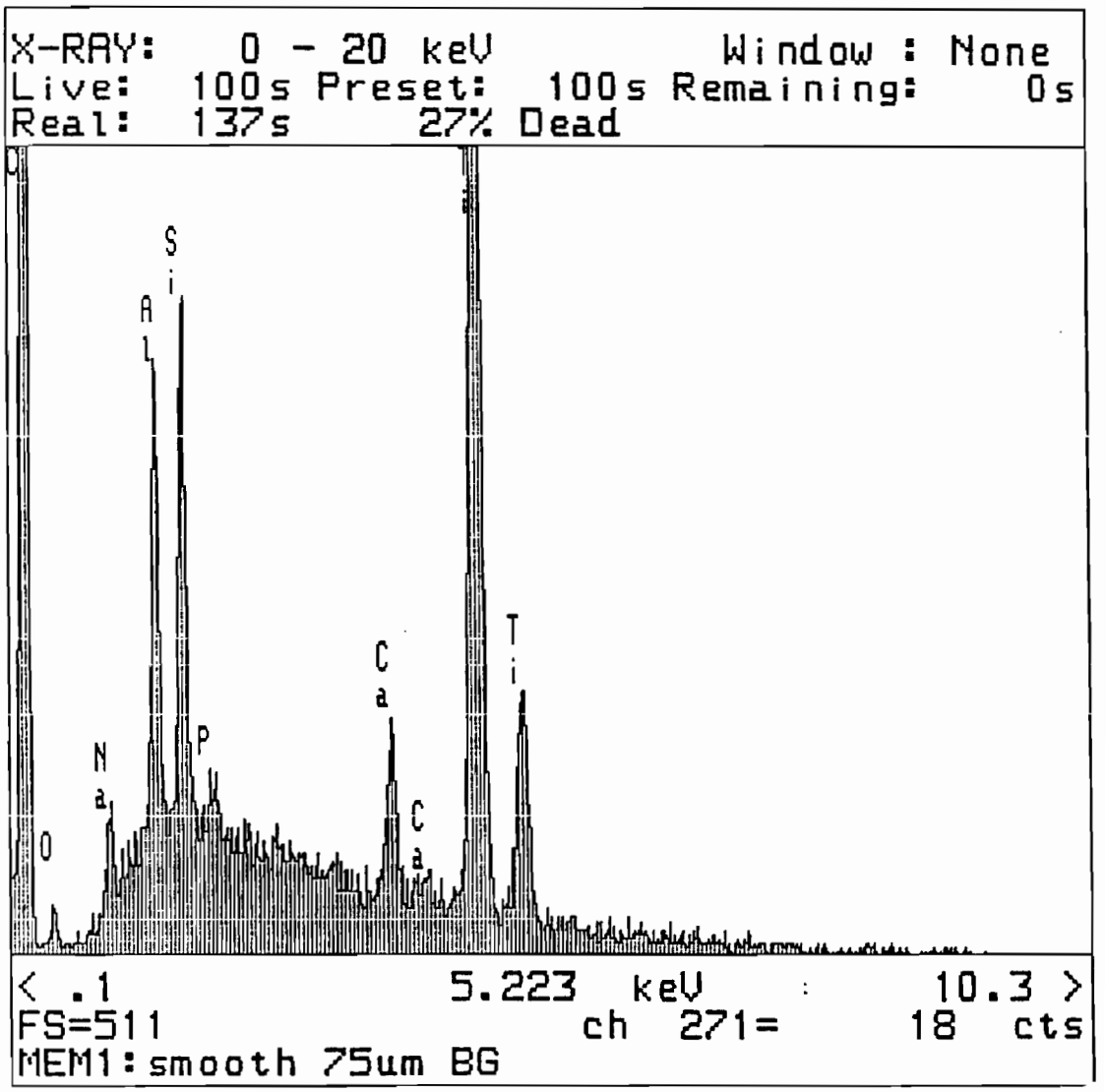

Figure 4.10 Second EDS spectrum of BG on the polished cross-section of a smooth-75μm BG specimen. Note the signs of the Ti-6Al-4V substrate.

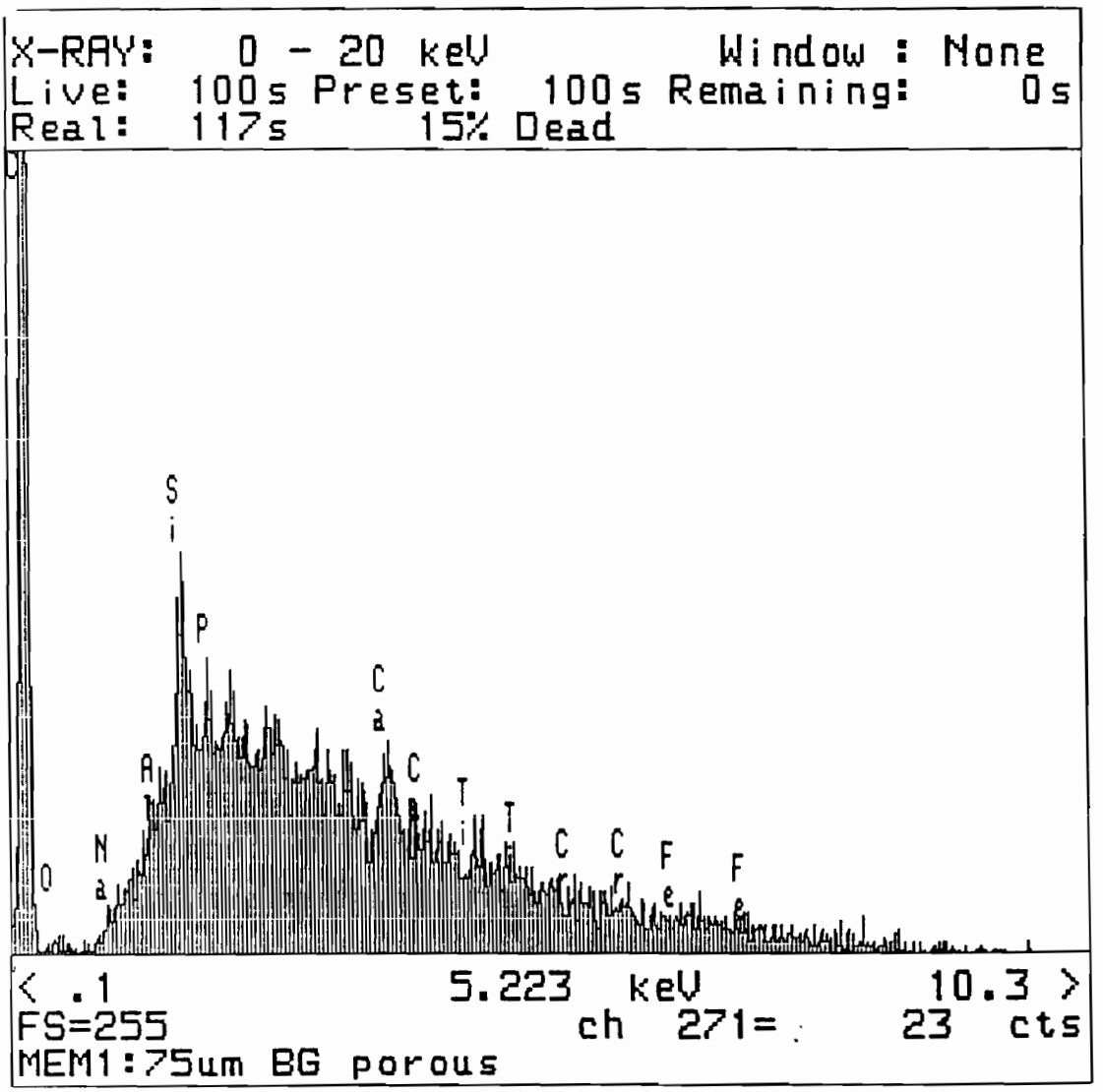

Figure 4.11 EDS spectrum of the unpolished cross-section of a porous-75µm BG specimen. Note the low clarity in the peaks and the signs of Fe and Cr.

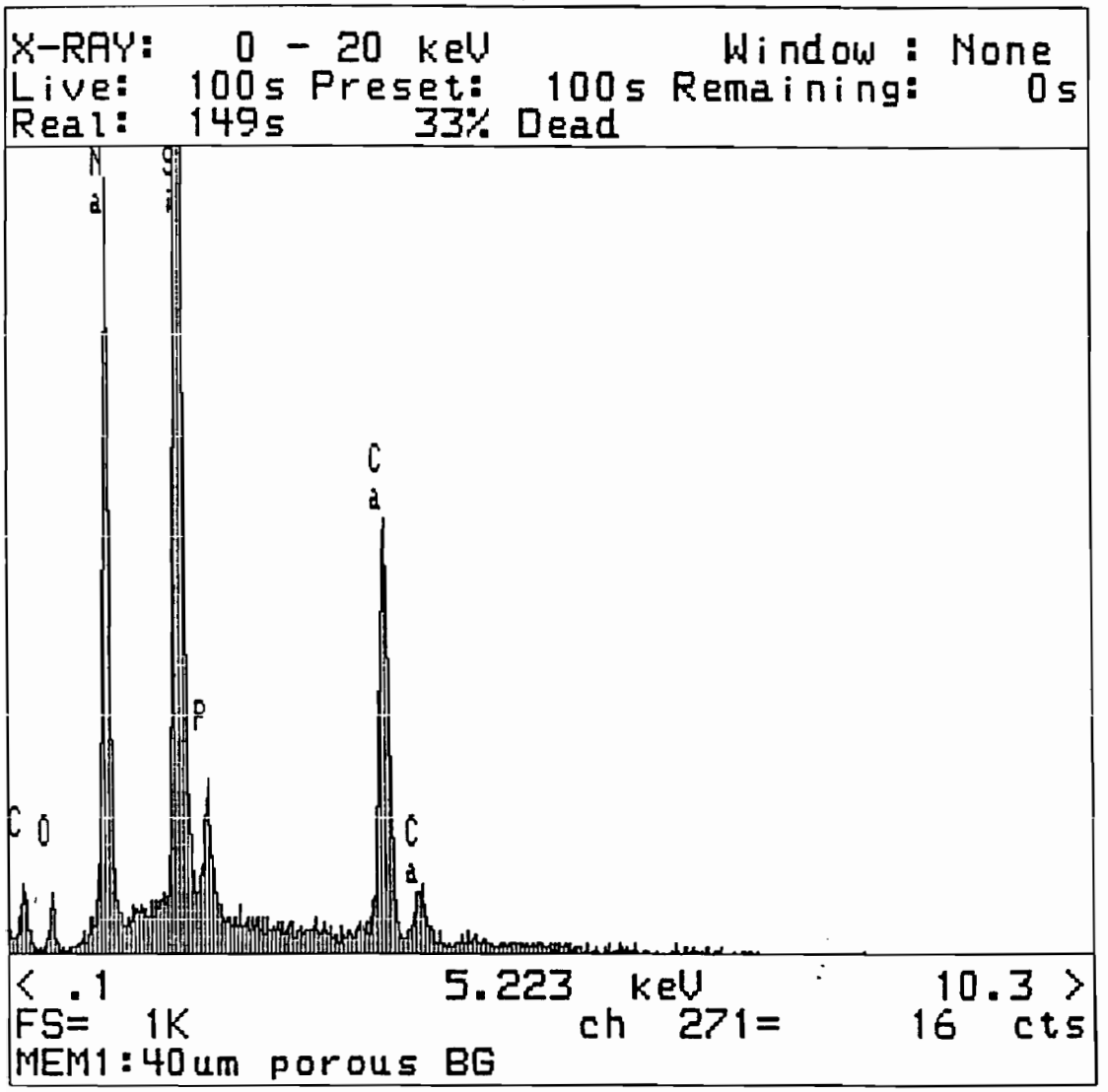

Figure 4.12 First EDS spectrum of BG on the polished cross-section of a porous-40μm BG specimen.

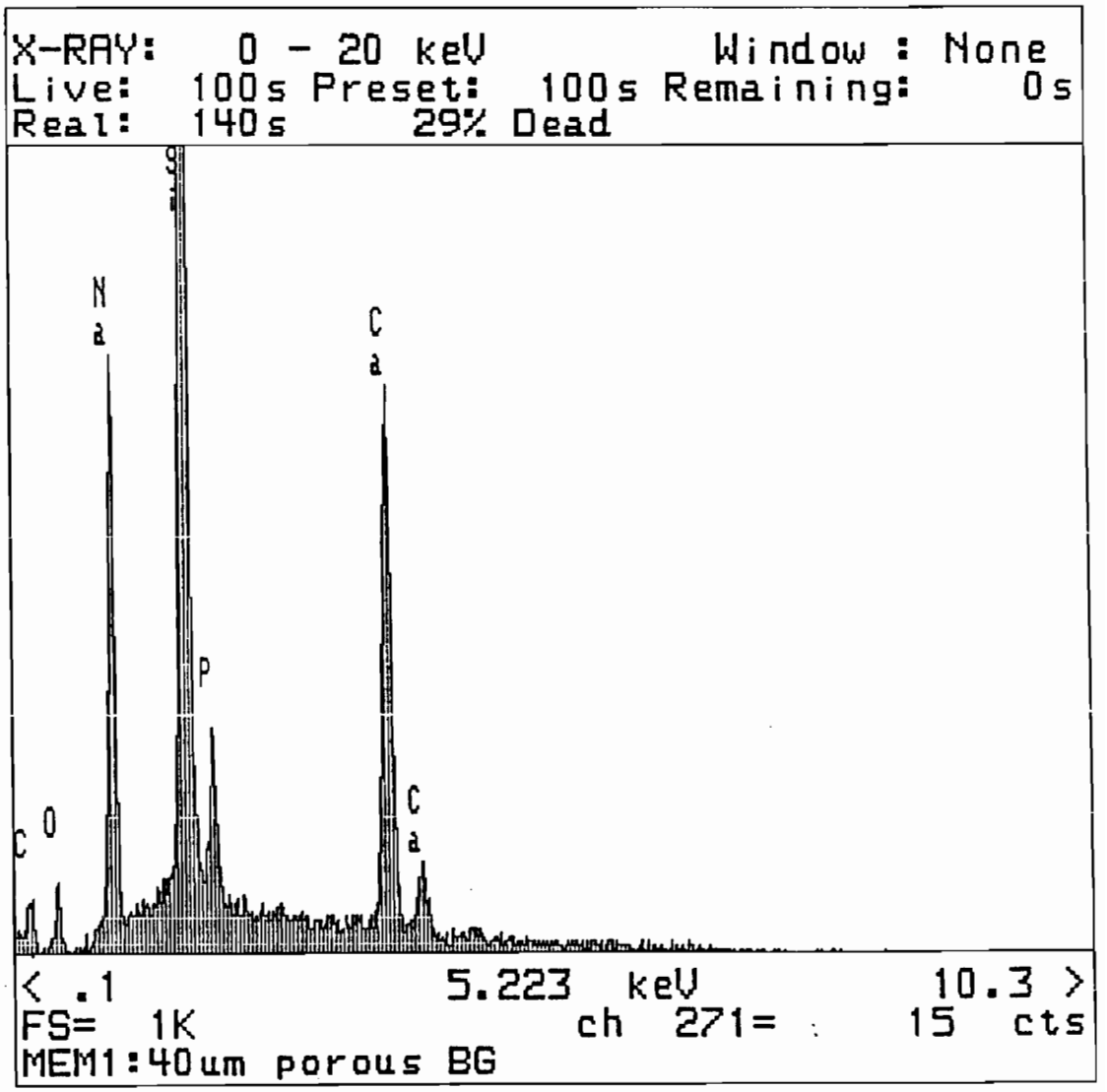

Figure 4.13 Second EDS spectrum of BG on the polished cross-section of a porous-40μm BG specimen.

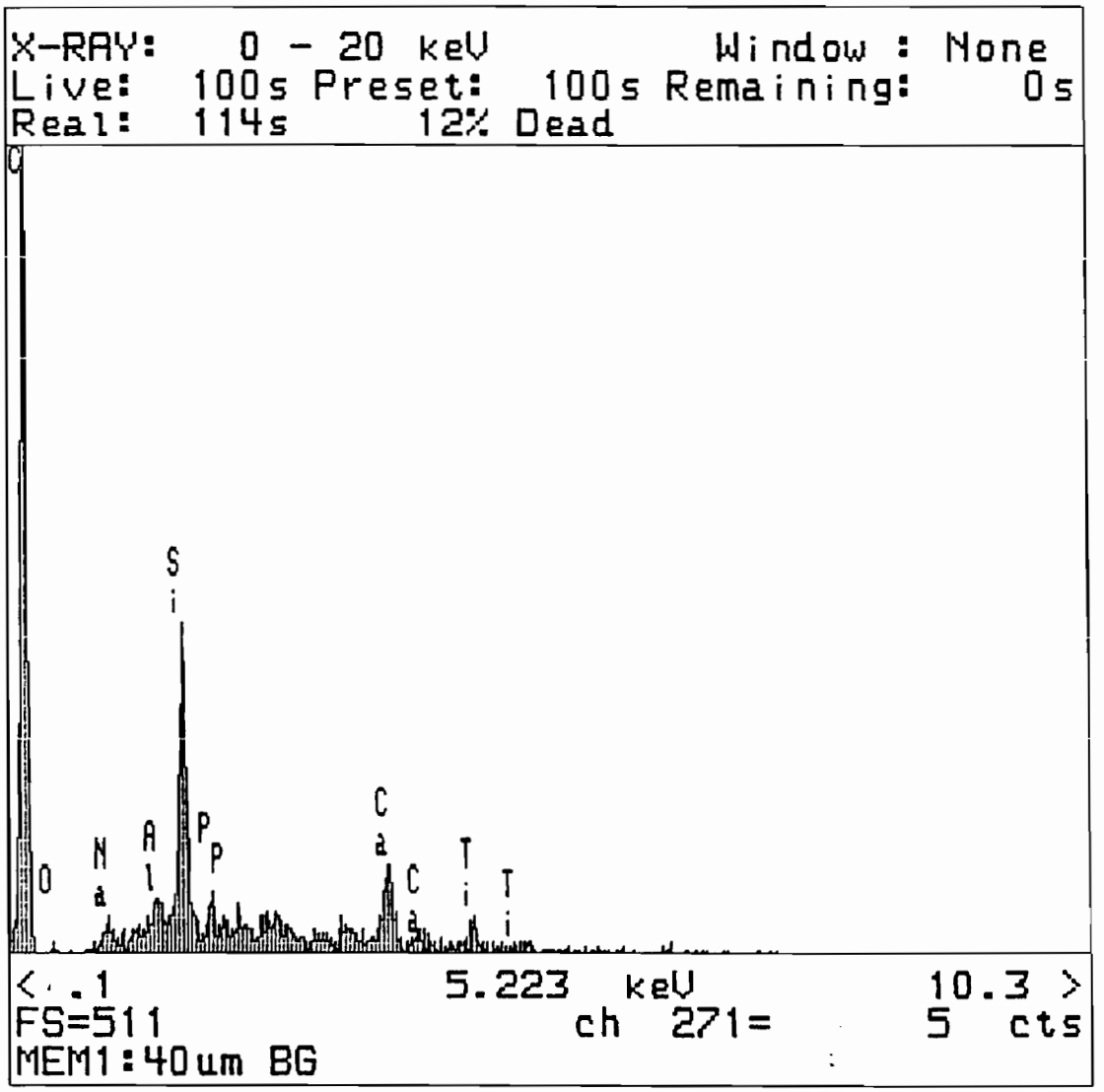

Figure 4.14 First EDS spectrum of BG on the polished smooth-40μm BG specimen. Note the signs of the Ti-6Al-4V substrate.

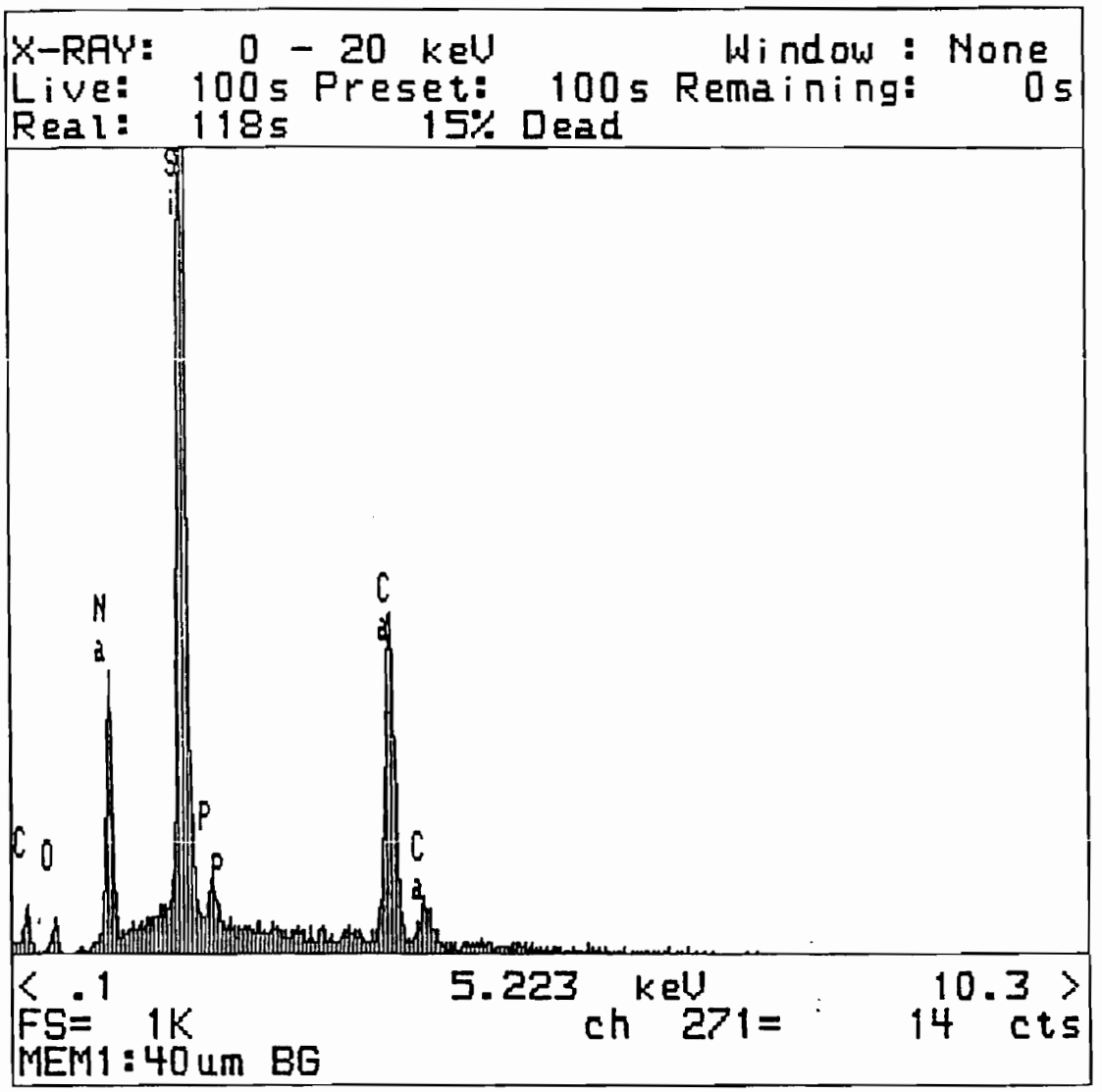

Figure 4.15 Second EDS spectrum of a BG on the polished cross-section of a smooth-40μm BG specimen.

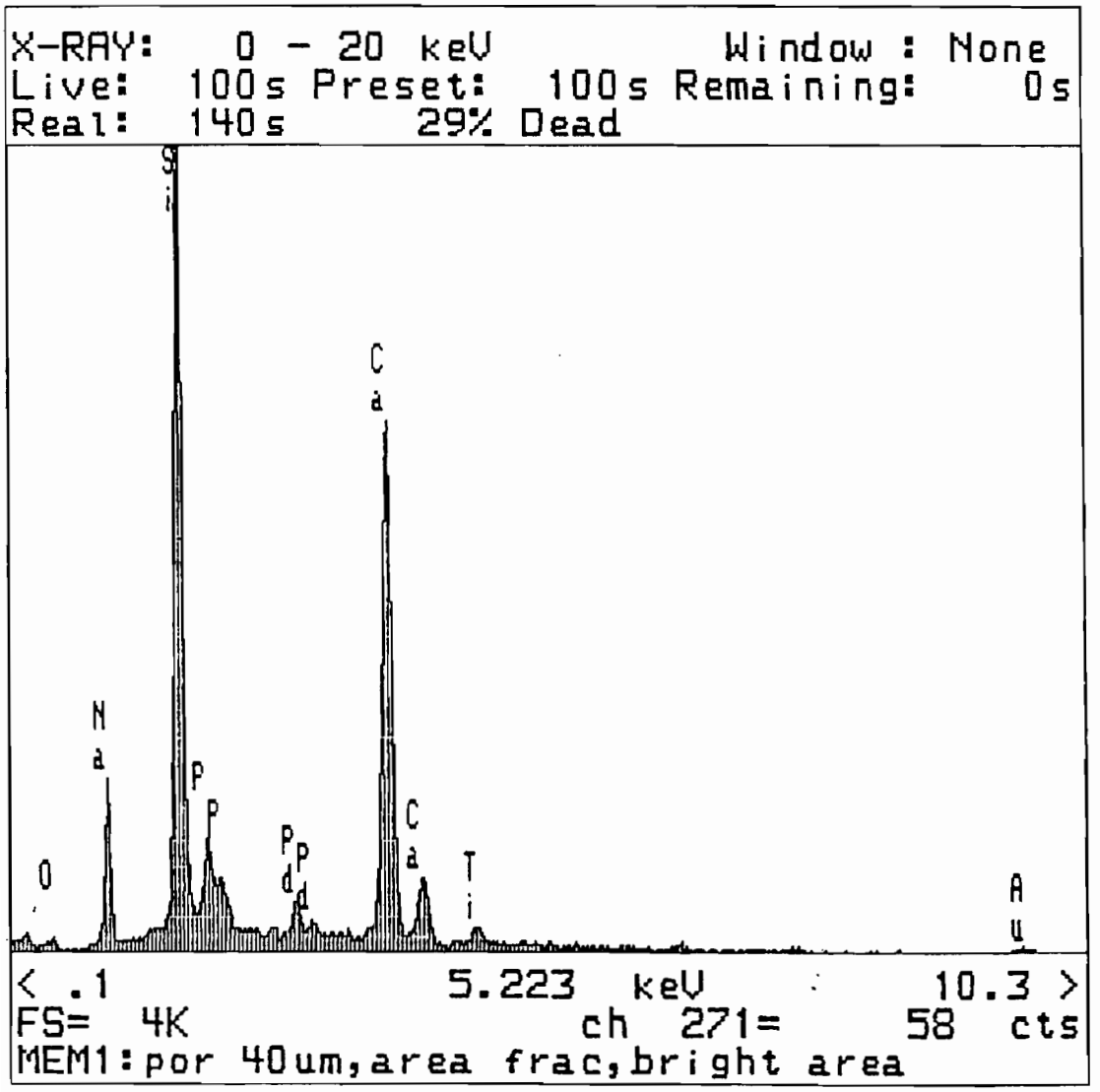

Figure 4.18 EDS spectrum of the brighter zones as BG of porous-40μm sample. Note the peaks from the Au/Pd coating.

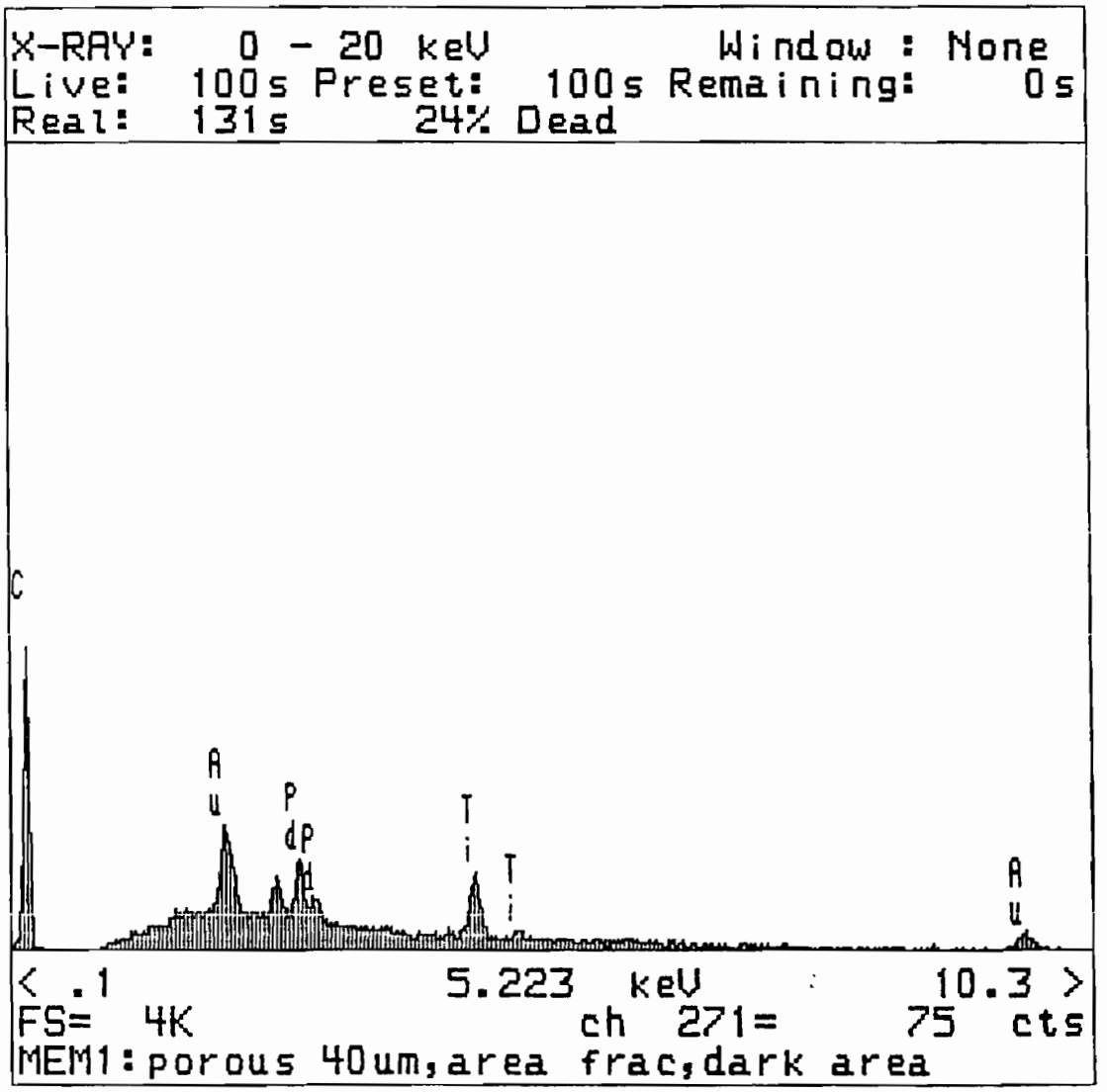

Figure 4.19 EDS spectrum of the darker areas as Ti and Au/Pd sputter coating of the porous-40μm sample.

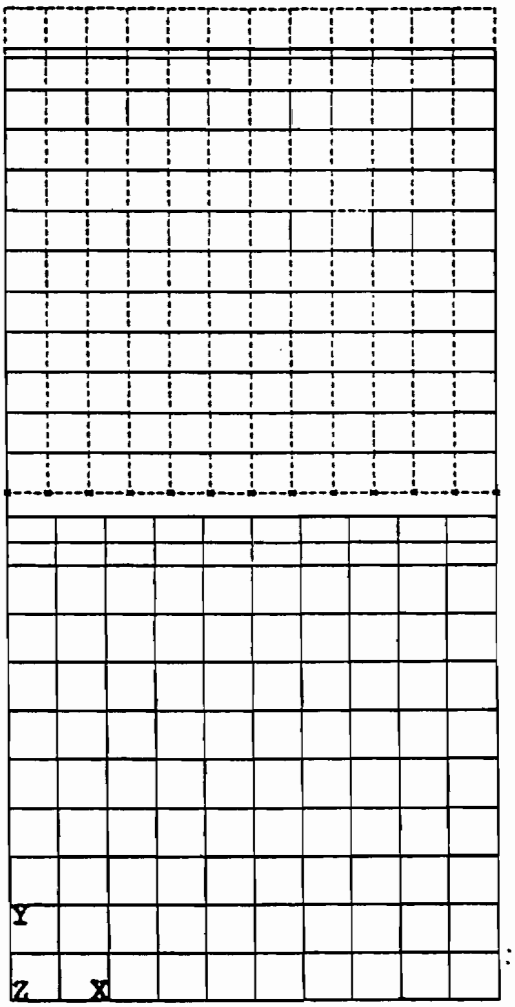

Figure 4.20 Displacement plot of the prescribed displacement contact model showing closure of the gap.

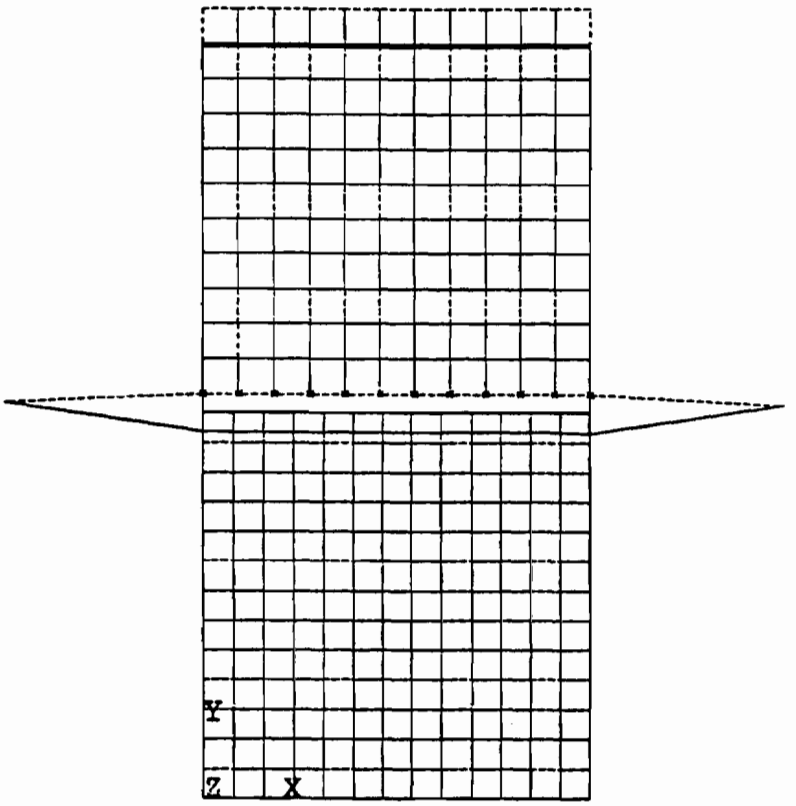

Figure 4.21 Displacement plot of the compressive point-load contact model. Note the closure of the gap.

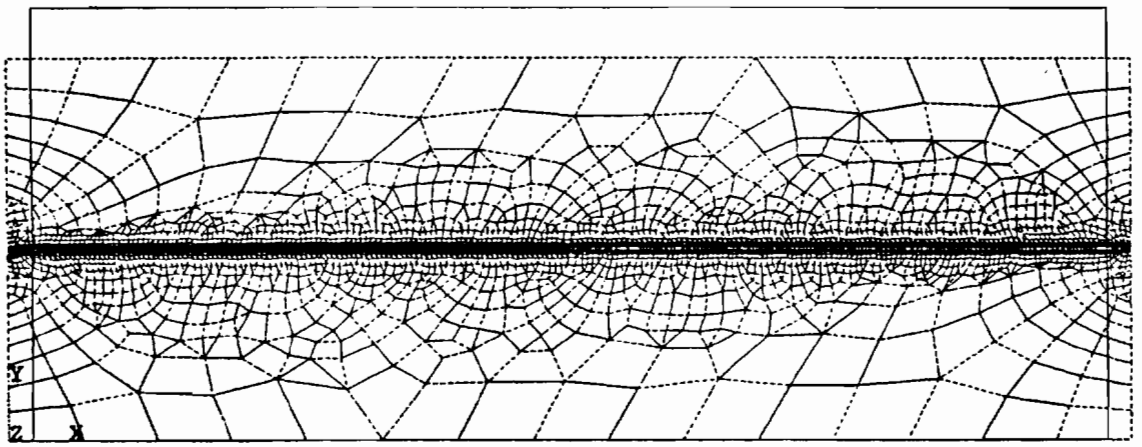

Figure 4.22 Displacement plot of the 2D model.

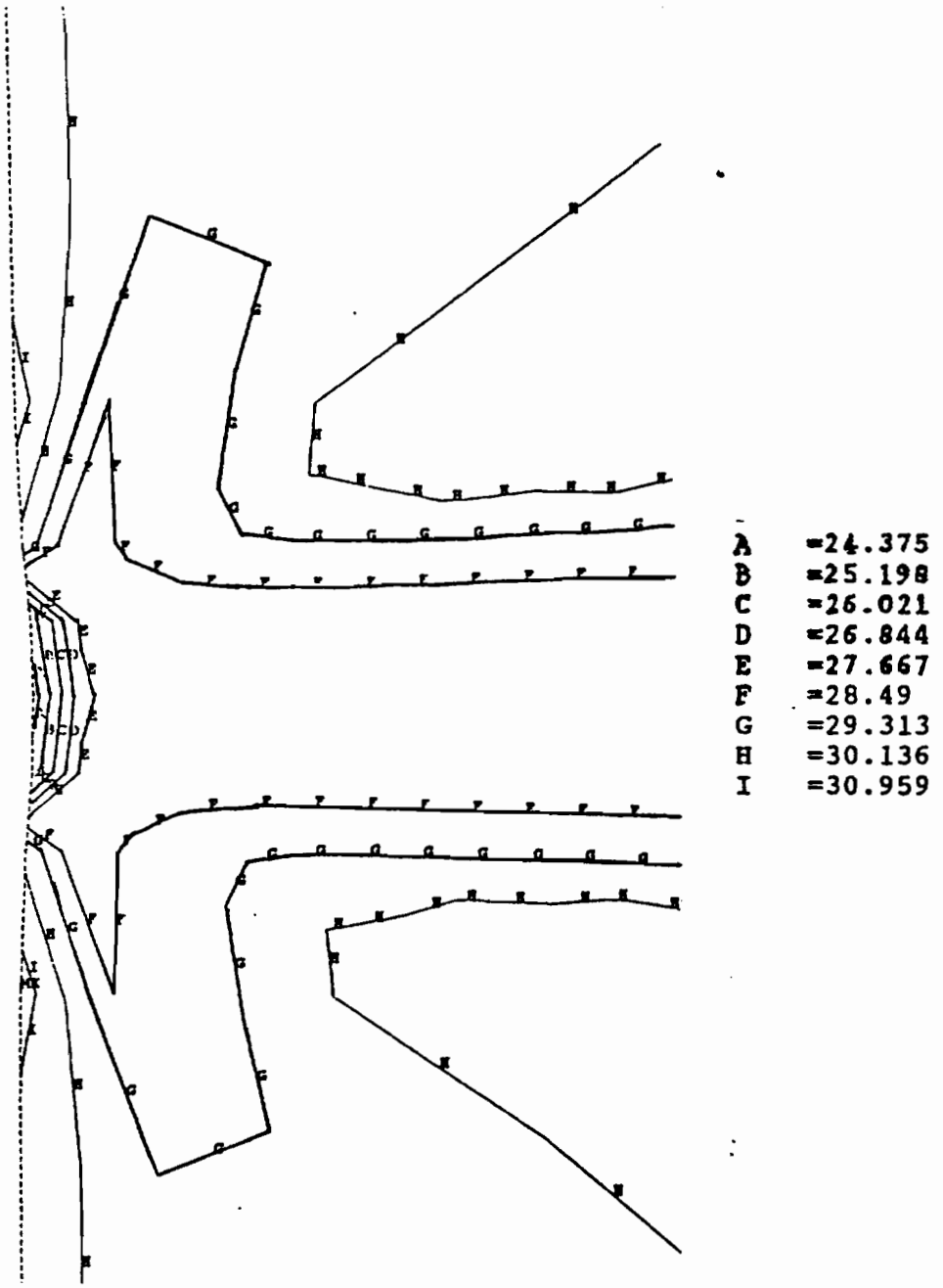

Figure 4.23 Equivalent stress of the two BG/Ti-6Al-4V interfaces of the 2D model.

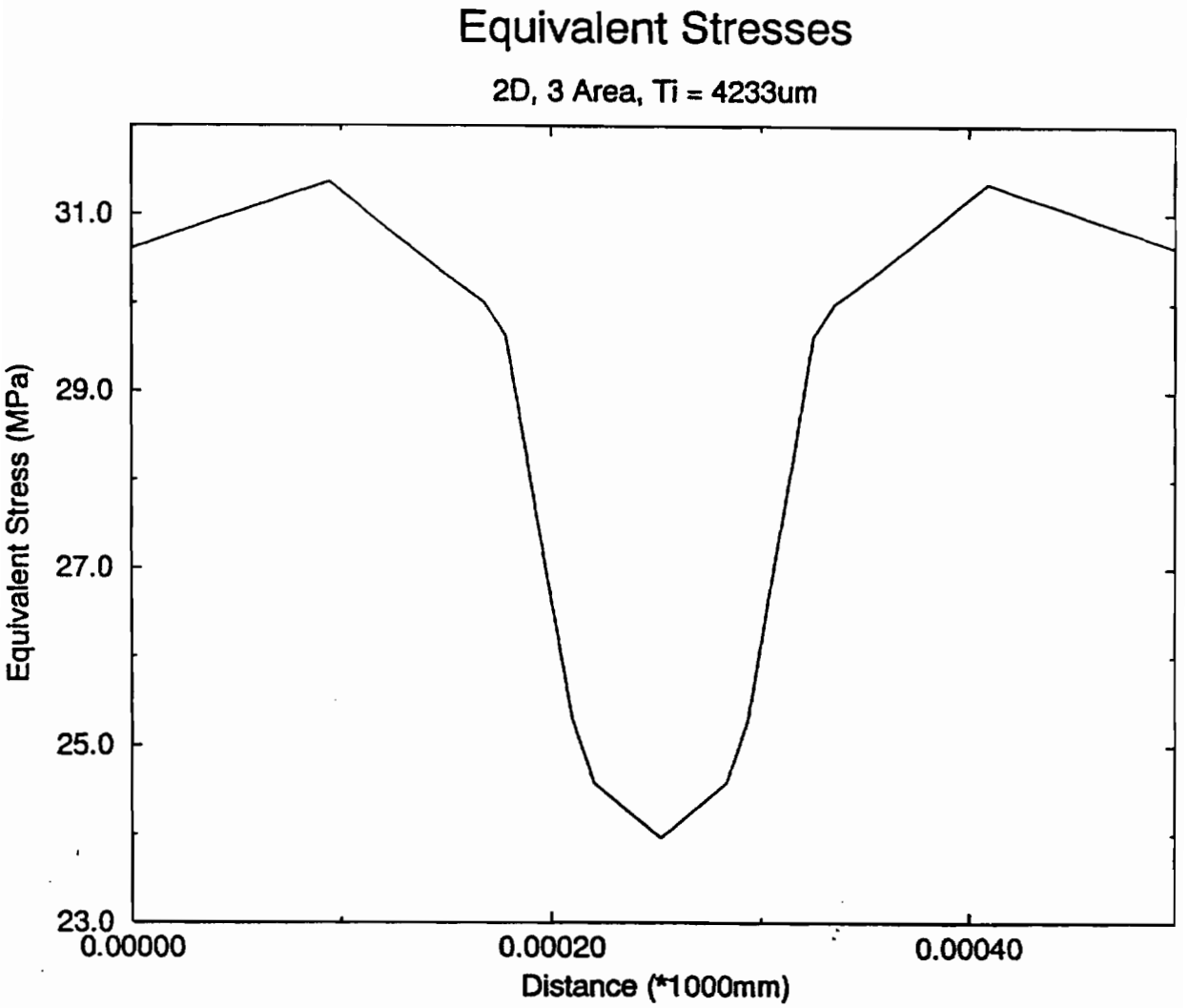

Figure 4.24 Graphical plot of the equivalent stress from Figure 4.23 indicating the interfaces with sharp stress jumps.

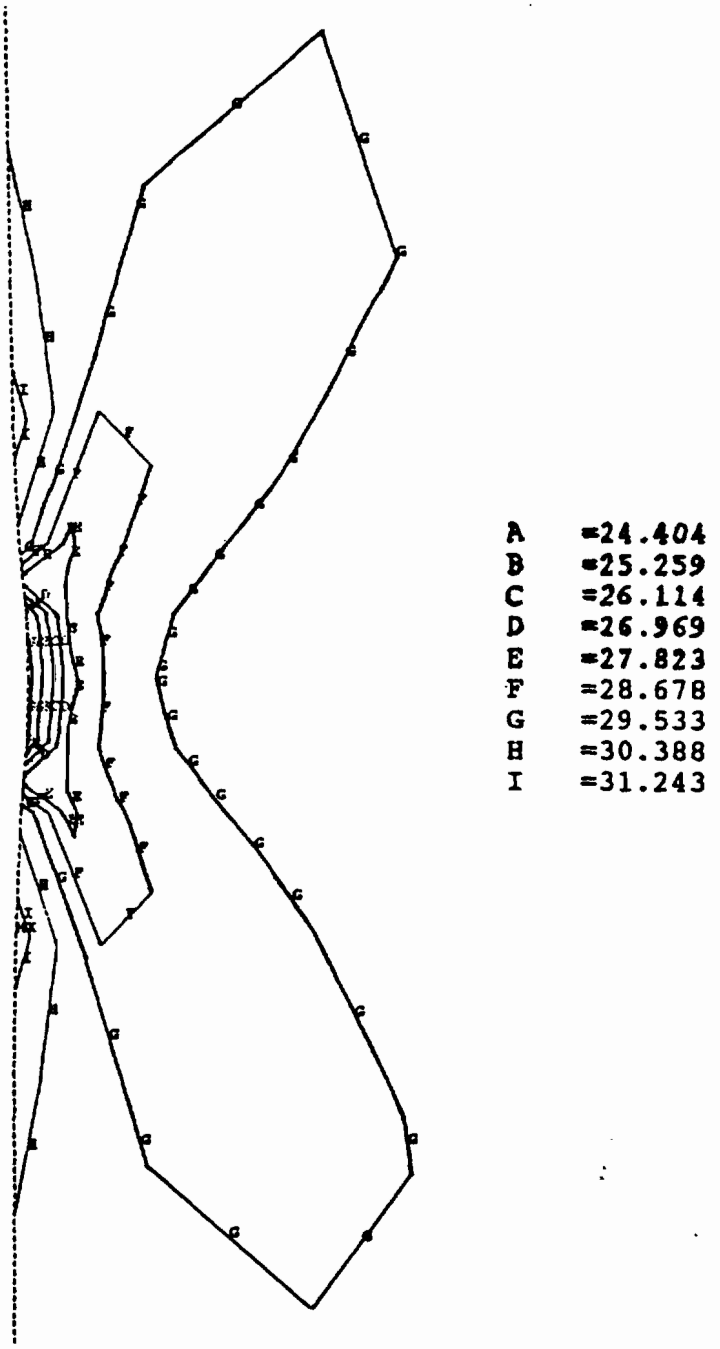

Figure 4.25 First principal stress of the 2D model at the two BG/Ti-6Al-4V interfaces.

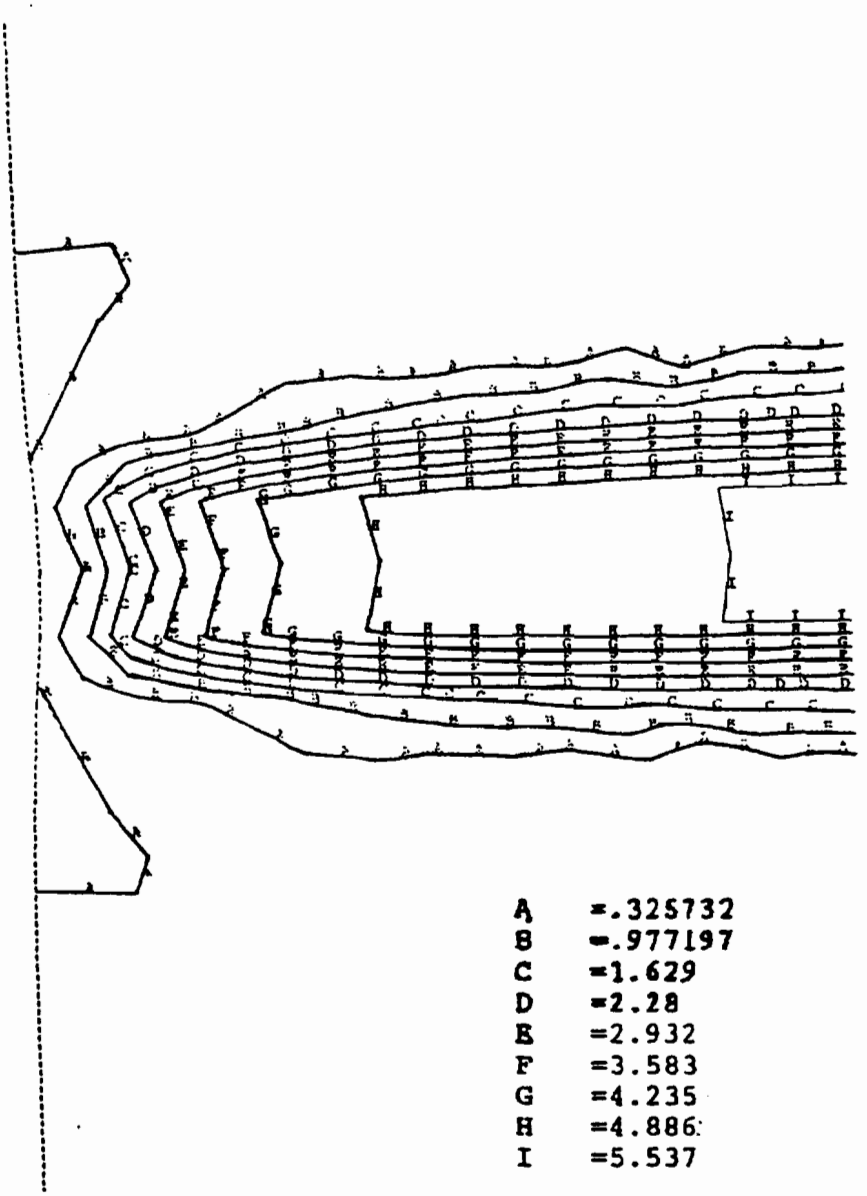

Figure 4.26 Second principal stress at the two BG/Ti-6Al-4V interfaces of the 2D model.

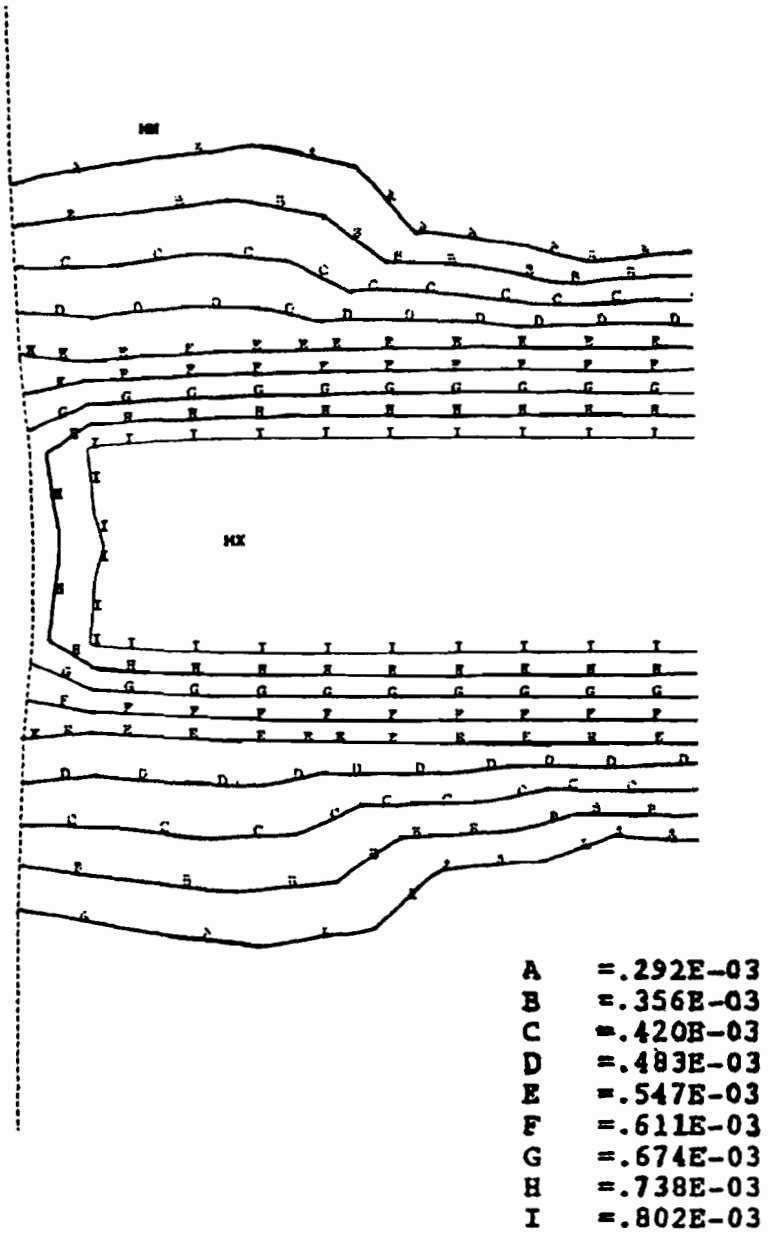

Figure 4.27 First principal strain of the two BG/Ti-6Al-4V interfaces of the 2D model.

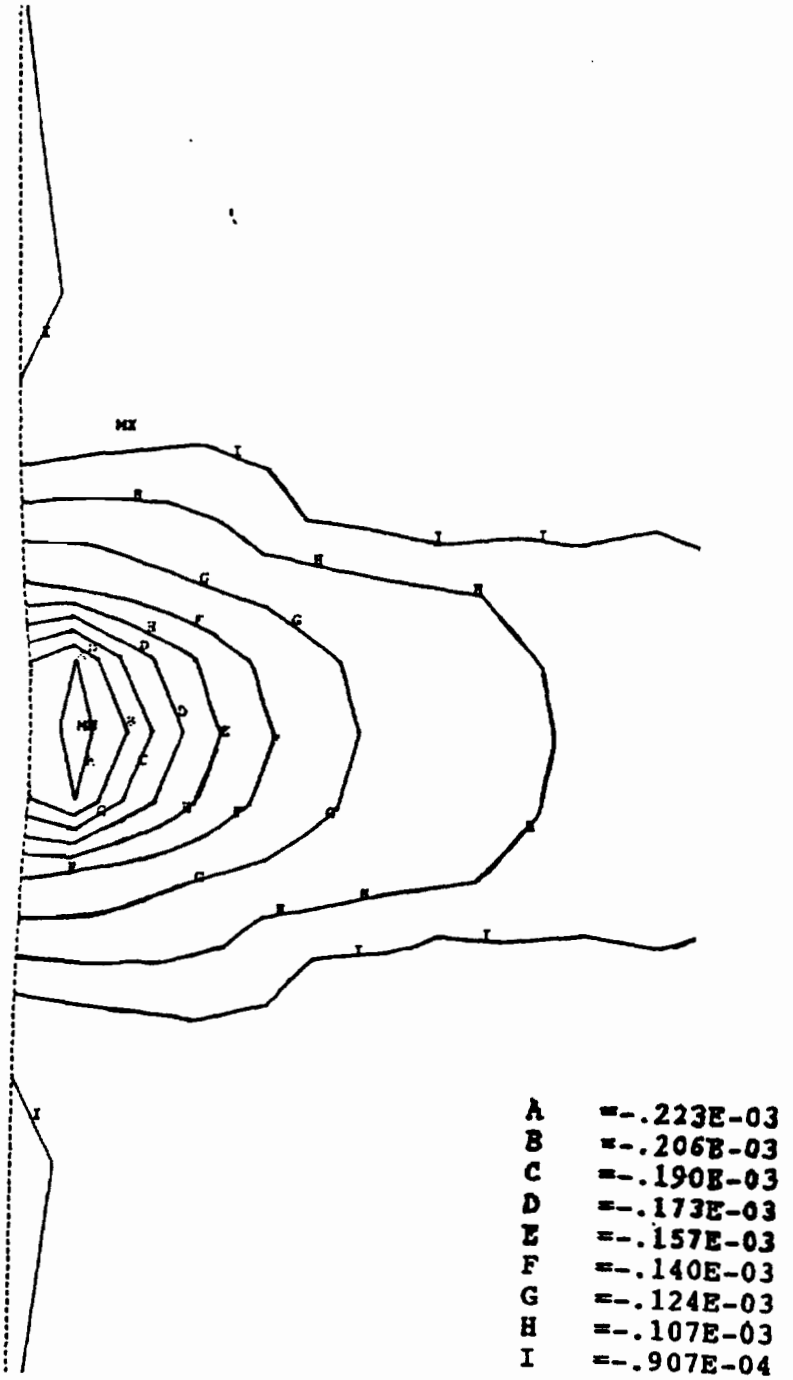

Figure 4.28 Second principal strain of the two BG/Ti-6Al-4V interfaces of the 2D model.

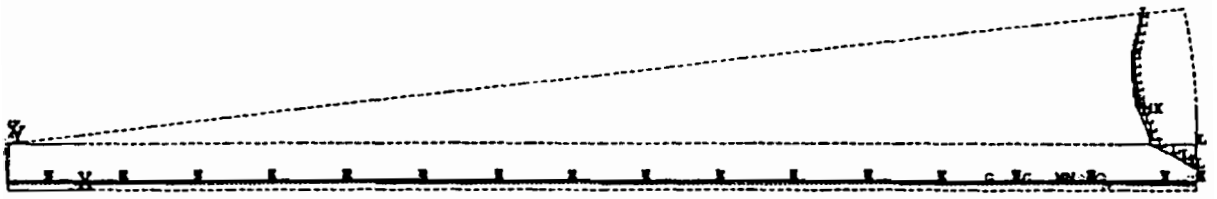

A =23
B =23.9
C =24.8
D =25.7
E =26.6
F =27.5
G =28.4
H =29.3
I =30.2
J =31.1
K =32
L =32.9

Figure 4.29 Equivalent stress plot of the 10° cylinder with the Ti-6Al-4V height of 450μm.

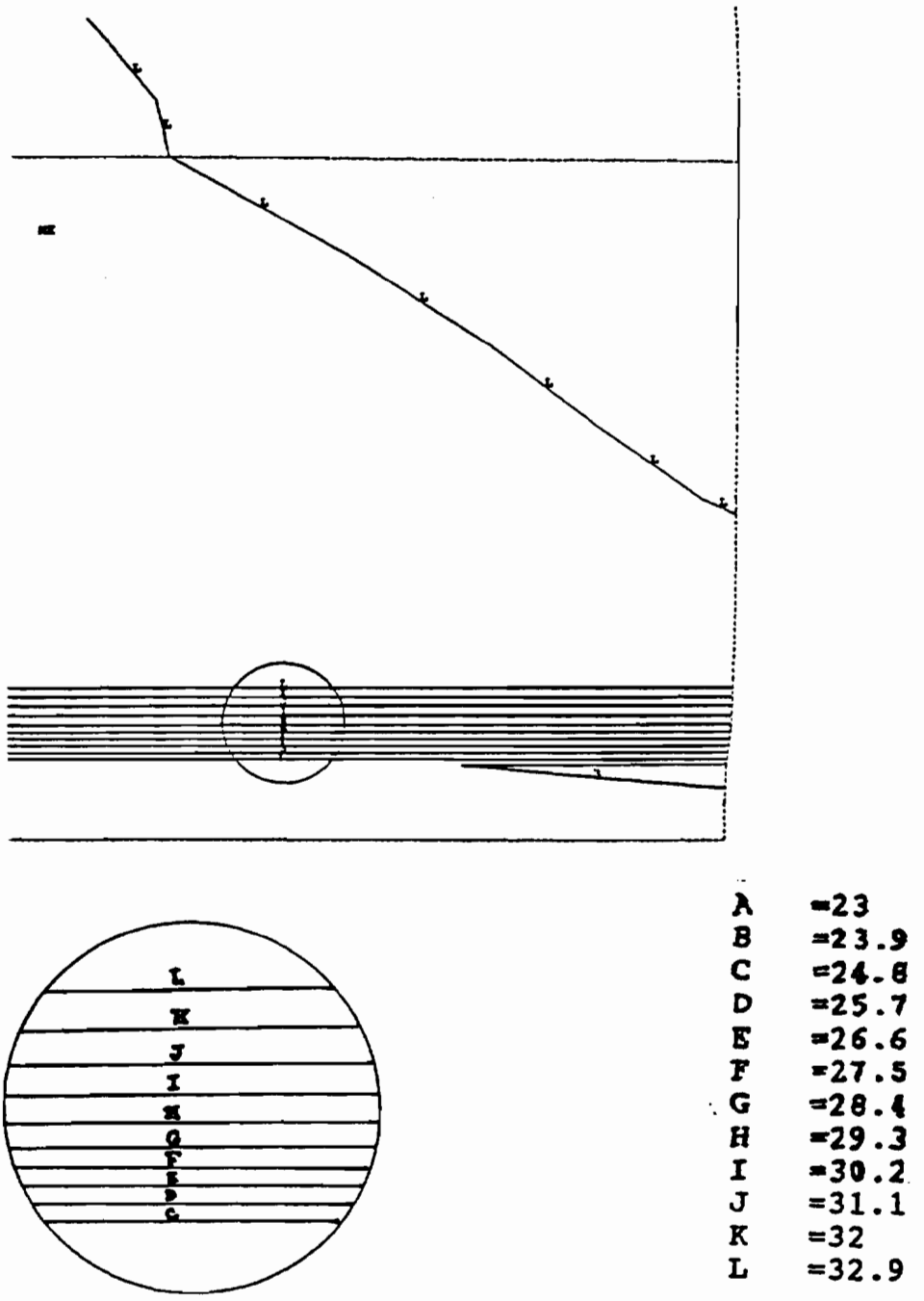

Figure 4.30 Magnification of the equivalent stresses shown in Figure 4.29 with the area of interest being the outer edge of the cylinder.

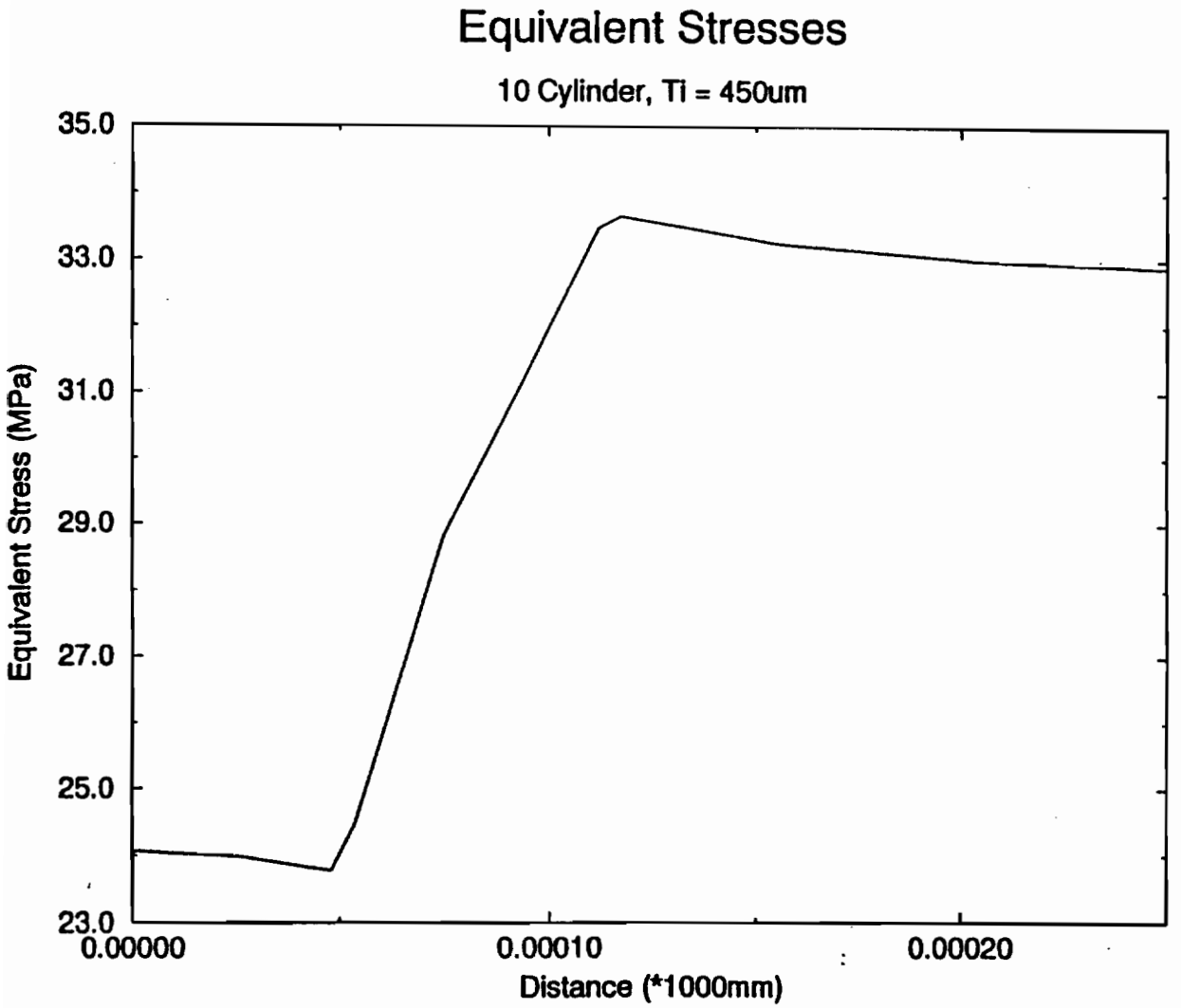

Figure 4.31 Graphical plot of equivalent stresses of the 10° cylinder with the Ti-6Al-4V height of 450μm. Note the sharp increase in stress at the BG/Ti-6Al-4V interface.

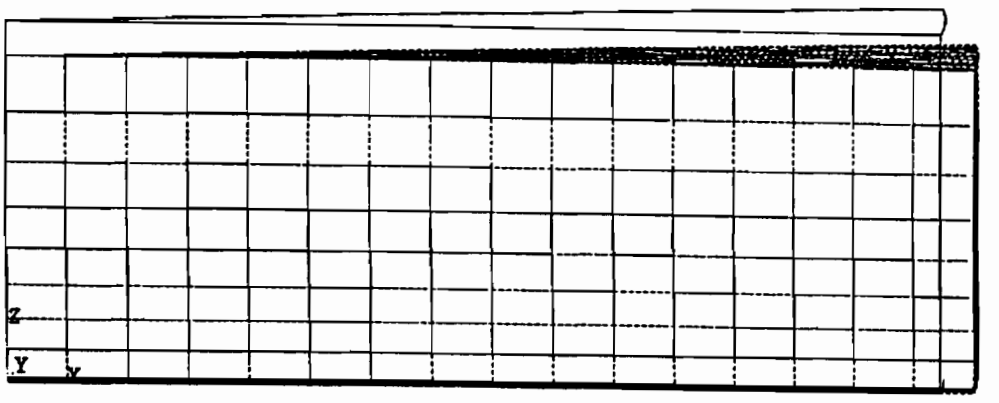

Figure 4.32 Displacement plot of the 10° cylinder with Ti-6Al-4V height set to 4233μm. Note the increase in height and decrease in radius.

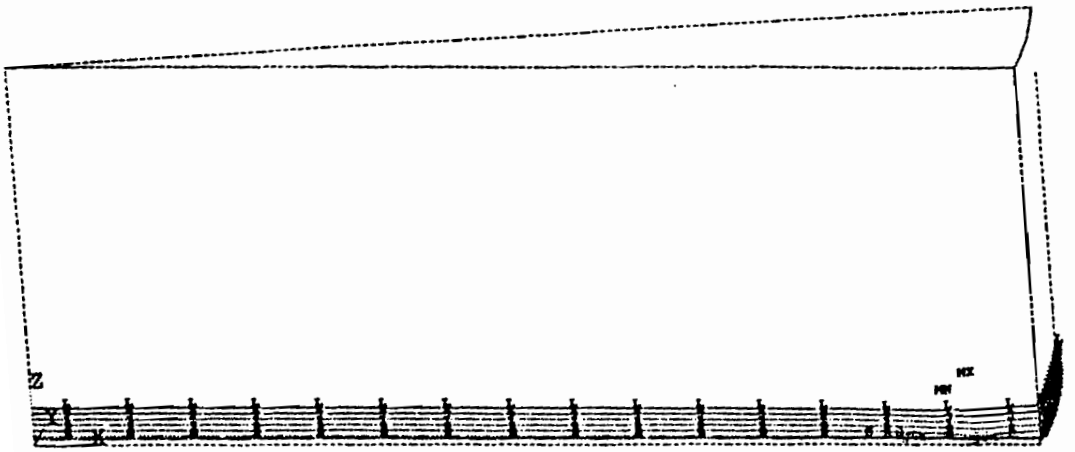

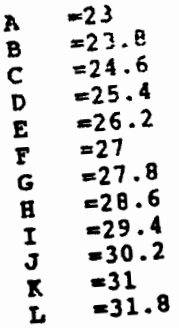

Figure 4.33 Equivalent stress plot of the 10° cylinder with Ti-6Al-4V height set to 4233μm.

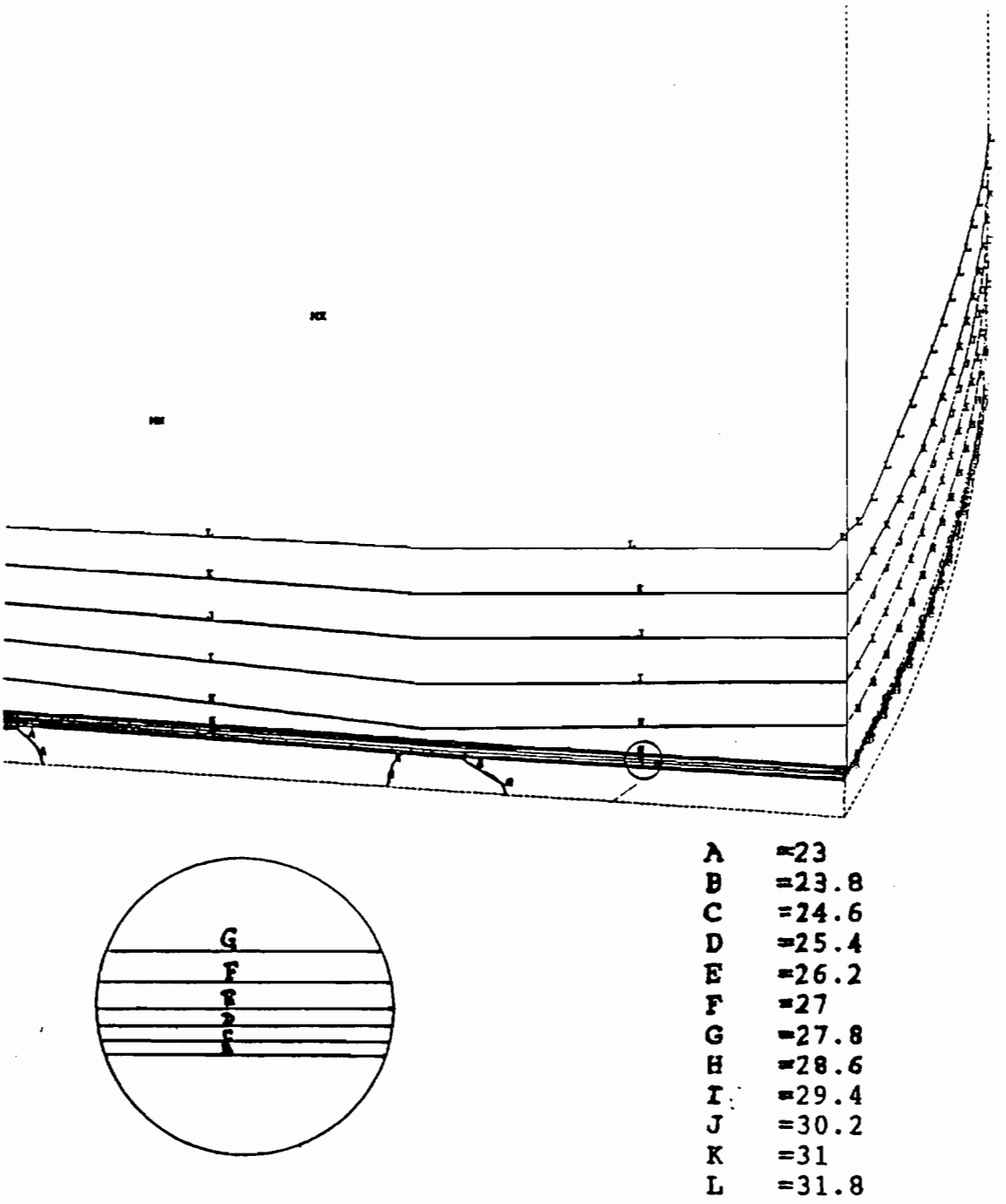

Figure 4.34 Magnification of the outer edge of Figure 4.33 showing the equivalent stress at the BG/Ti-6Al-4V interface.

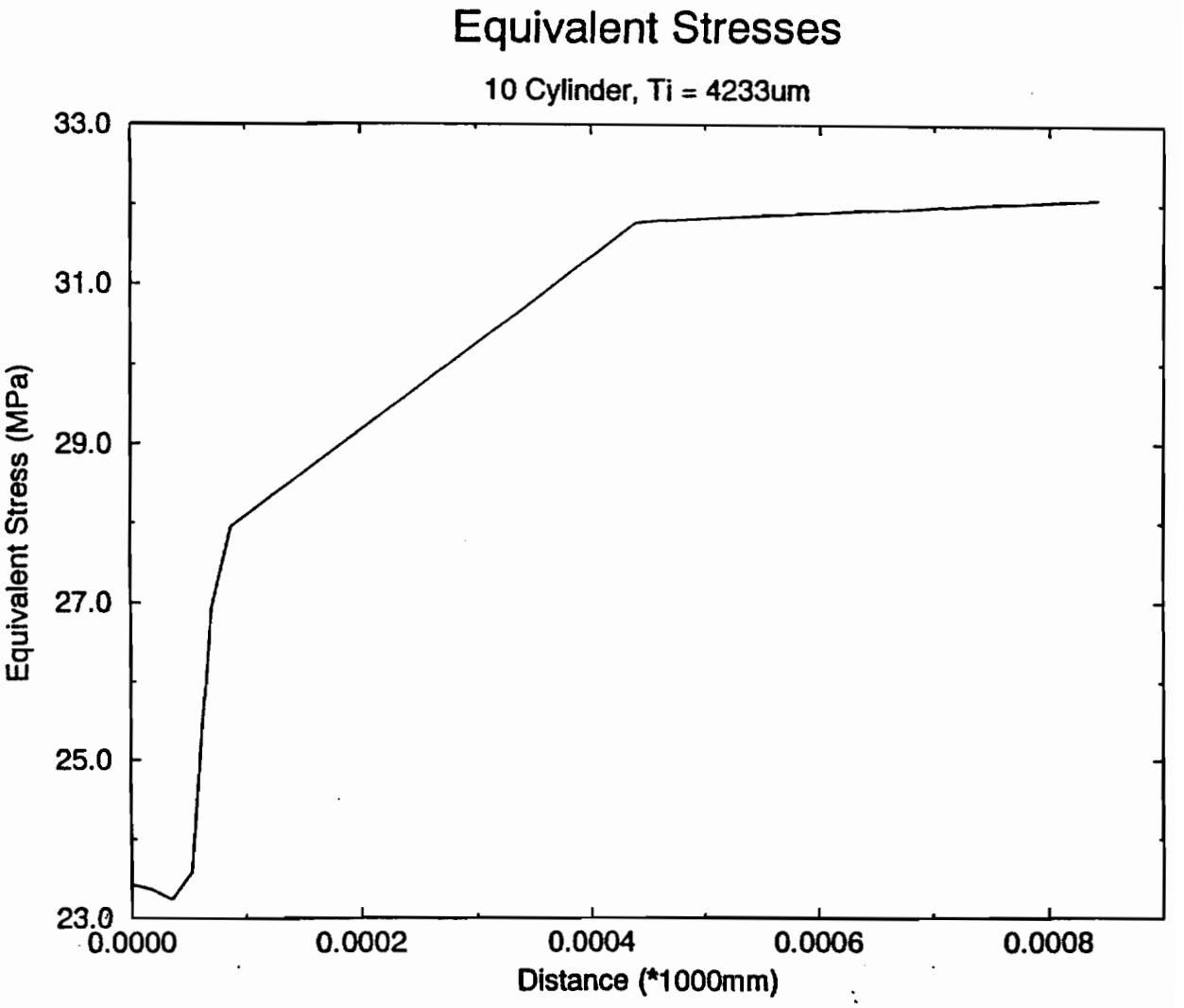

Figure 4.35 Graphical plot of the equivalent stress shown in Figure 4.34. Note the sharp increase in stress at the BG/Ti-6Al-4V interface.

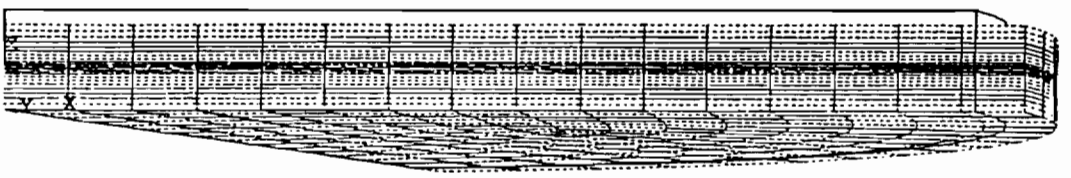

Figure 4.36 Displacement plot of the 10°, three volume cylinder showing the height increase and a decrease in radius.

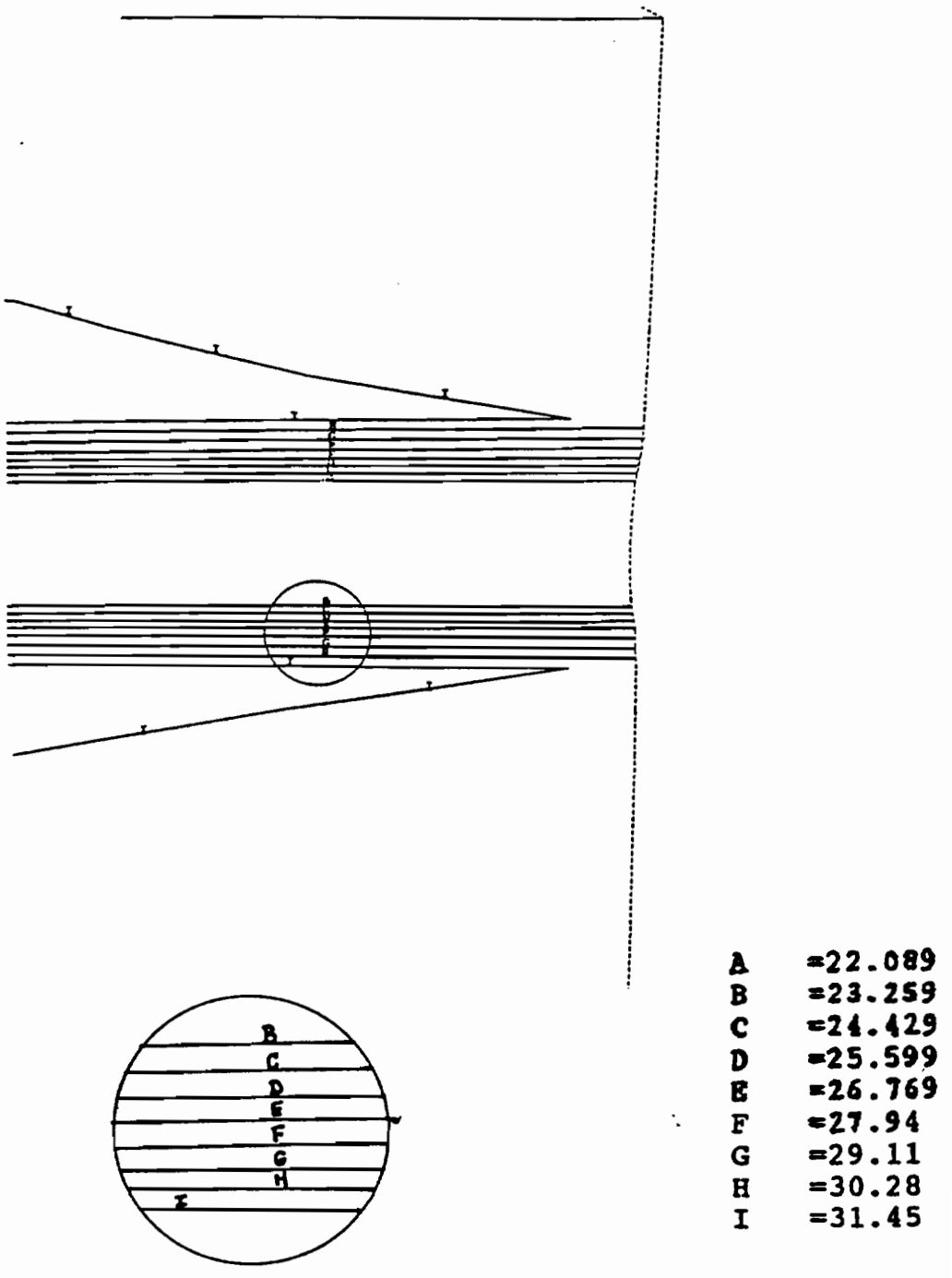

Figure 4.37 Equivalent stress at the two BG/Ti-6Al-4V interfaces along the circumference of the 10°, three volume model.

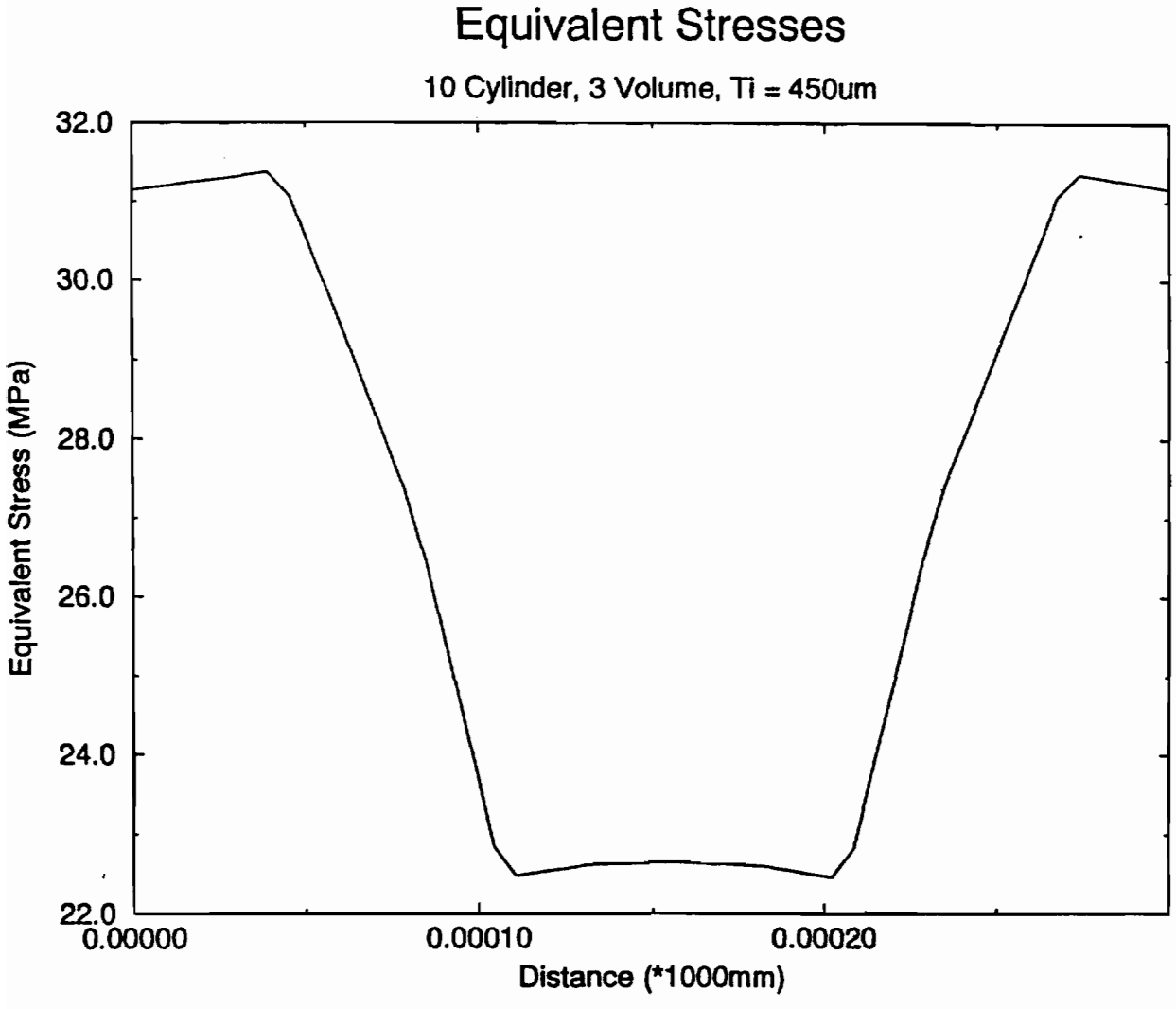

Figure 4.38 Graphical plot of the equivalent stress of the 10°, three volume cylinder showing the two interfaces with increases in stresses.

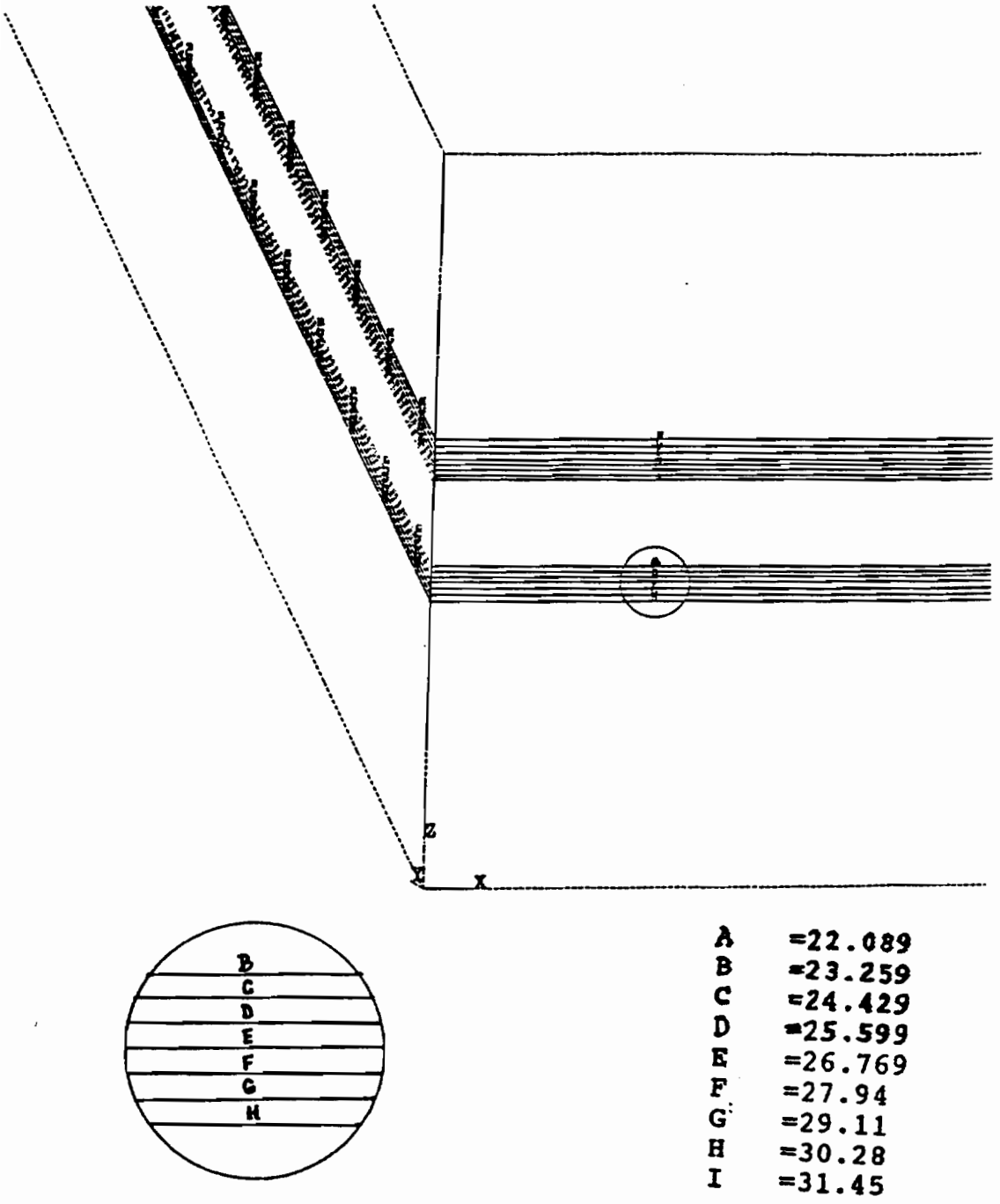

Figure 4.39 Equivalent stress of the two BG/Ti-6Al-4V interfaces at the center of the 10°, three volume cylinder.

CHAPTER 5

DISCUSSION

5.1 Mechanical Test

5.1.1 Modulus of Rupture

The modulus of rupture acquired through the three-point bend (48.14±15.23MPa) differs from the value observed under the four-point bend performed by Filho et al [52]. The MOR from the four-point bend was as high as 80MPa with a standard deviation of approximately ±22MPa. This discrepancy could be attributed to several factors including the difference in specimen cross-section. This study used specimens of 5mm X 5mm cross-section whereas the four-point bend test used specimen cross-sections of 5.4mm X 3.5mm. The calculation of the MOR involves the inverse of the width (b) times the thickness (h) squared -- (bh^2). The four-point bend had a bh^2 value of 66.15mm^3, whereas, this study had a bh^2 value of 125mm^3. With the bh^2 value being inversely proportional to the MOR, the lower the bh^2 value, the higher the calculated MOR. The distance between the outer supports was 28mm for the four-point bend, however, this study had an outer support span of 14mm. The outer support span is directly proportional to the MOR and therefore, the larger the support span, the higher the MOR value.

5.1.2 Ti-6Al-4V Tensile Test

Even though the measured modulus of elasticity for Ti-6Al-4V had a difference of 18% from that taken from the literature, the effects on the FEA results were negligible.

5.1.3 Bond Strength Test

The porous samples yielded lower bond strength than the smooth coupons. One may expect that the porous interlocking of BG would result in higher bond strengths, however, upon analyzing the fractured surfaces, it was evident that the FM1000 did not effectively cover the test surface. Some portions of the porous test surface had FM1000 in the pores which leads to the question of whether or not the mechanical test yielded the bond strength of BG on Ti-6Al-4V, or a combination of BG bonding and the mechanical interlock strength of FM1000.

The thinner the BG coating, the higher the bond strength value. This trend is consistent with a study using a 150μm BG coating from which a bond strength of 33.0±4.3MPa was reported [6]. A similar trend was also noted for HA coatings [117].

Proper alignment was a problem with some of the test specimens. During the curing of the FM1000, the smooth surfaces slid out of alignment. This was overcome by the rotating and pivoting arms of the fixtures that could reposition themselves with the specimen.

Previous studies of the bond strength of plasma-sprayed bioceramics on metal cite bond strengths of HA on metal. A 50μm HA coating on Ti-6Al-4V was tested in tension and its bond strength was found to be 85±3.9MPa [17]. Another study [118] investigated the bond strength of plasma-sprayed HA coatings on Ti-6Al-4V. This study used a smooth Ti-6Al-4V coupon that was gritblasted with a HA coating of 135μm and loaded in tension which yielded a bond strength of 6.7±1.5MPa. A porous Ti-6Al-4V coupon with a 120μm HA coating resulted in a lower bond strength of 3.7±1.2MPa. A tensile test with a 150μm HA coating plasma-sprayed onto Ti-6Al-4V resulted in a bond strength of 52.0±11.7MPa [6]. Yang et al [117] used a tensile bond strength test to determine the adhesion strength between plasma-sprayed HA and Ti-6Al-4V. The HA coatings were

approximately 200μm thick and varied in porosity percentage, concentration of impurity phases, and crystallinity. The maximum value of bond strength for Yang's study was 30.98±1.12MPa [117]. The trend observed from all of these studies agrees with the trend seen in this study where the bond strength was inversely proportional to the coating thickness.

5.2 Scanning Electron Microscopy (SEM)

5.2.1 Secondary Electron

The BG-MOR fracture surface revealed concentric rings coming from the compressive surface to the tensile surface. These "rings" appear to be related to iso-stress lines at the contact patch that are in accordance with Hertzian contact theory. They may signify the potential of spalling under flexure loading (Figure 5.1). Amorphous BG is a homogenous material as seen by the backscatter electron microscopy shown in Figure 4.5. Under mechanism of failure, however, the Backscatter electron images show that the spicules from the "spalling" to be of a different composition.

The EDS spectra of the bond strength test specimens shows that BG is indeed still evident on the fracture surface which indicates that the bulk BG coating is actually weaker than the bond between BG and Ti-6Al-4V. Some of spectra also show signs of the Ti substrate which is expected, especially in areas of the BG closest to the metal due to diffusion that occurs from plasma-spraying.

The unpolished cross-section of the porous-75μm specimen revealed a less clear EDS spectrum when compared with the polished samples. Also, signs of foreign elements were observed such as Cr and Fe. These unexpected elements can be from residual metal that was possibly on the diamond blade used to section this specimen.

Measurements of BG found were approximately 5μm in thickness. This would indicate that BG delaminated from sections of the substrate but failed within itself in other areas of the fracture surface. This phenomena is also witnessed in the fields taken under

backscatter electron microscopy for area fraction measurements. Area fraction measurements were not taken of the smooth or the porous 75μm BG group. The smooth-75μm group were extremely burned during the torching of FM1000 for fixture removal. While collecting fields from the porous 40μm specimen, it was noted that many of the pores were filled with glue; leaving only the very top surfaces of the upper layer of beads to show any BG. Other fields did show open pores where the lower layer of beads could be seen in addition to the sides of the upper layer beads. Considering the inconsistent glue coverage, it was decided that this method of estimating the area of BG was inconclusive, thus the porous 75μm group were not analyzed for area fraction measurements.

5.3 Finite Element Analysis (FEA)

5.3.1 Contact Theory

The prescribed displacement and compressive point-load models were successfully completed. The tensile model did not attain complete convergence since contact elements do not support tensile loading. Therefore, a prescribed displacement model with the displacement oriented in a tensile direction would have failed as well, and was thus not attempted. The findings of this study showed that contact theory was inappropriate for modeling tensile loading across contact interfaces. However, contact theory was found to be robust for modeling compressive loading, and thus, would be appropriate for simulating a push-out test.

5.3.2 Rigid Contact

5.3.2.1 2D Rigid Contact

The stress distribution was as expected, with the singular stress fields appearing at the free edge interfaces. This 2D model suggests that failure would initiate at the free edge interfaces then propagate along the interfaces resulting in complete delamination of the BG coating from the Ti-6Al-4V substrate. The 45° projections of high stresses from

the singular stress fields suggest the presence of resolved shear stresses experienced during lateral contractions caused from the tensile load.

The nodal and elemental solution differ slightly due to the averaging that occurs across the nodes of each element and its neighboring elements. The nodal solution therefore displays smooth flowing contours of stress distributions throughout the model.

The first principle strain shows the anticipated delamination that occurs along the x-direction. The third principle strain would represent delamination through the depth of this plane stress model. The second principle strain displays the delamination along the y-direction.

5.3.2.2 3D Rigid Contact

The results of the 3D model suggests complete delamination of BG off Ti-6Al-4V. Unlike the 2D model, the 3D model also shows that failure would occur all at once because of the lack of singular stress fields at the free edge interface. Instead of a pronounced point of maximum stresses (singular stress fields), maximum stresses are shown throughout the Ti-6Al-4V substrate until the BG volume is reached.

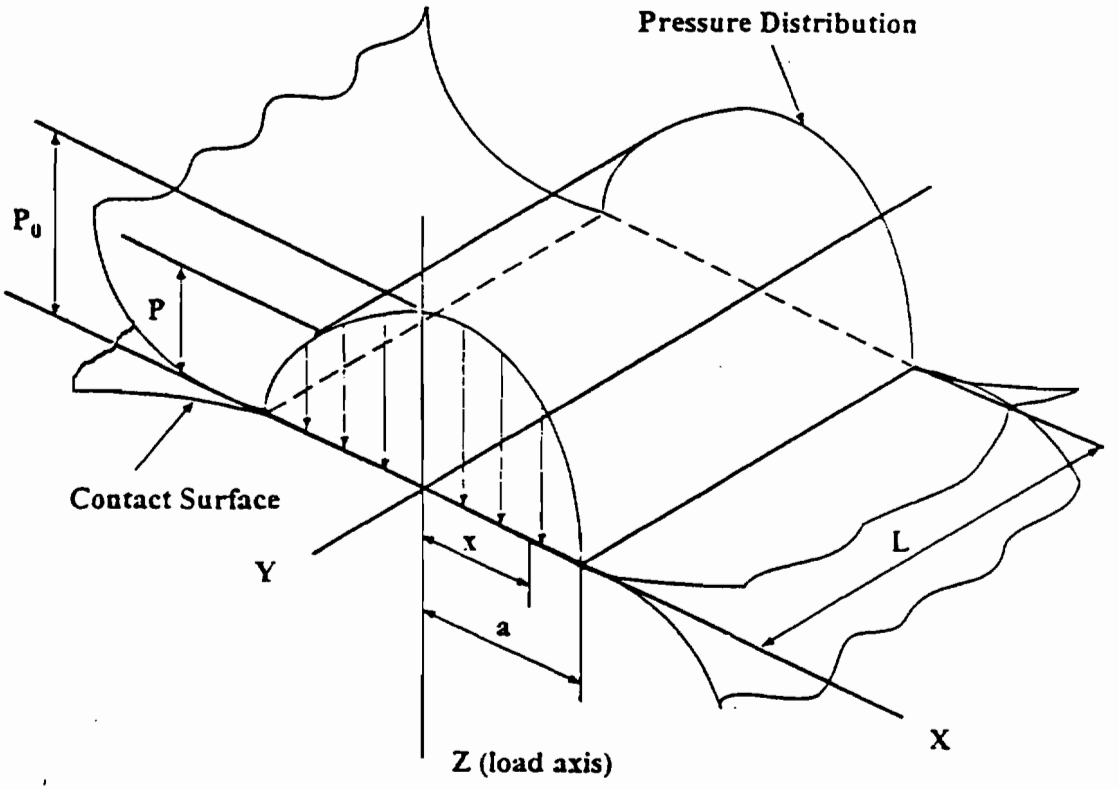

Figure 5.1 Contact pressure distribution for two elastic cylinders.

CHAPTER 6

CONCLUSION & FUTURE WORK

Several conclusions have been drawn from this investigation. The modulus of rupture of BG is about 2-3 times the value of the ultimate tensile strength [111]. The estimated ultimate tensile strength of BG was lower than the experimental bond strength of the plasma-sprayed tensile coupons.

The bond strength tests also showed a relationship between BG coating thickness to the bond strength. The results of both porous and smooth bond strength test specimens imply that the thinner coating thickness has a stronger adherence to its substrate. Although the bond strength values coincide with trends observed from other studies, improvements must be made in the test configuration where mechanical interlocking between glue and test surface can be eliminated.

While taking area fraction measurements, the fields showed that the glue closed many of the pores, covering the underlying layer of beads and only revealing the small portions of the tops of the upper layer of beads. For a more accurate area fraction measurement of the porous specimens, taking fields along successive cross-sections is recommended. The specimen could be potted then cross-sectioned at every 5μm with fields taken after each cut.

The amorphous BG material appears to be a homogeneous substance. However, when fractured, the surface showed particles of a different chemical composition when viewed using backscattered electron imaging. Within the confines of the scope of this

work, EDS was not performed on the BG to decipher the composition of the particulate matter. This, however, would be a good future study task.

The conclusion drawn from the contact theory study was that it was only valid for models simulating compressive or impact loads. The 2D rigid contact model confirmed the existence of singular stress fields at the free edge interface as seen in previous studies [122]. The 2D model results showed crack initiation occurring at the free edge interface followed by propagation along the interface. The 3D model showed potential spontaneous delamination of the interface. The FEA models analyzed in this study assumed BG to be isotropic and homogeneous. While results from this study were quite reasonable, they could be improved by using material property data that more closely represents BG, namely orthotropic and heterogeneous.

Recommended future studies include *in vivo* investigations into the bioactivity of 40μm and 75μm BG coated implants. Now that a pattern has been identified between coating thickness and mechanical bond strength; the obvious follow-up question is whether there is a relationship between coating thickness and bioactivity. A slightly weaker bond (75μm) may be tolerated for a higher initiation rate of new bone. Push-out tests could follow with both experimental and numerical components, maybe with an axisymmetric model for brevity.

Experimental bond strength tests should be run with plasma-sprayed coated specimens versus dipped specimens. The porous specimens could be tested with only one layer of sintered beads. This may cut back on the porosity typically seen in clinical prosthetics, however, it would also reduce the effects of mechanical interlocking between the glue and the beads.

High speed photography could be used to monitor the crack initiation site on the experimental bond strength samples. This test may confirm the method of failure advanced by either the 2D or 3D FEA models of this study. In addition, an axisymmetric model should be analyzed in order to lead more credibility to the delamination modes suggested by the 2D and 3D models.

Crystalline HA has been noted previously as having a stronger bond strength than

more amorphous HA [117]. Therefore, a comparison between amorphous BG and crystalline BG bond strengths could potentially lead to the optimum BG coating.

Bibliography

1. Dietrich, D.E.. *User's Manual for Revision 5.0*. Philadelphia: Swanson Analysis Systems, Inc., 1992.

2. Park, J.B.. "Orthopedic Prosthesis Fixation." *The Biomedical Engineering Handbook*. Ed. J.D. Bronzino. Boca Raton: CRC Press, 1995. p. 704-723.

3. Faker, A.C.. "Corrosion of Metallic Implants and Prosthetic Devices." *Metals Handbook*. Eds. J.R. Davis, J.D. Destefani, H.J. Frissell, and G.M. Crankovic. 9th ed. Vol. 13. Metals Park: ASM International, 1987. p. 1324-1335.

4. Shackelford, J.F.. "Major Mechanical Properties." *Introduction to Materials Science for Engineers*. 2nd ed. New York: Macmillan Publishing Company, 1980. p. 99-124.

5. Shackelford, J.F. and W. Alexander. *The CRC Materials Science and Engineering Handbook*. Boca Raton: CRC Press, 1992.

6. Chern Lin, J.H., M.L. Liu, and C.P. Ju. "Structure and properties of hydroxyapatite-bioactive glass composites plasma sprayed on Ti6Al4V." *J Mater Sci Mater Med* 5(1994): 279-283.

7. Cubberly, W.H., P.M. Unterweiser, D. Benjamin, C.W. Kirkpatrick. "Properties of Titanium and Titanium Alloys." *Metals Handbook Properties and Selections: Stainless Steels, Tool Materials and Special-Purpose Metals*. 9th ed. Vol. 3. Metals Park: ASM Society for Metals, 1980. p. 372-406.

8. Davis, J.R., P. Allen, S.R. Lampman, T.B. Zorc, S.D. Henry, J.L. Daquila, and A.W. Ronke. "Introduction to Titanium and Titanium Alloys." *Metals Handbook: Properties and Selection: Nonferrous Alloys and Special-Purpose Materials*. 10th ed. Vol. 2. Metals Park: ASM International, 1990. p. 586-591.

9. Davis, J.R., P. Allen, S.R. Lampman, T.B. Zorc, S.D. Henry, J.L. Daquila, and A.W. Ronke. "Properties of Pure Metals." *Metals Handbook: Properties and Selection: Nonferrous Alloys and Special-Purpose Materials*. 10th ed. Vol. 2. Metals Park: ASM International, 1990. p. 1099-1177.

10. Dieter, G.E.. *Mechanical Metallurgy*. New York: McGraw Hill, 1986.

11. Askeland, D.R.. *The Science and Engineering of Materials*. Alternate ed. Boston: PWS Publishers, 1985.

12. Marieb, E.N. and J. Mallatt. *Human Anatomy*. California: The Benjamin/Cummings Publishing Company, Inc., 1992.

13. Gray, H. and J.A. Crocco. *The Classic Collector's Edition Gray's Anatomy*. 11th ed. New York: Crown Publisher's, Inc., 1977.

14. Lewis, J.L. and W.D. Lew. "Bioengineering of Total Joint Replacement." *Handbook of Bioengineering*. Eds. R. Skalak and S. Chien. New York: McGraw-Hill Book Company, 1987. p. 406-411.

15. Wheeler, D.. *The Use of Holographic Interferometry to Measure Surface Deformations of the Femur Due to a Cementless Prosthesis*. Master of Science. Gainesville: University of Florida, 1987.

16. Park, S.H., A. Llinas, V.K. Goel, and J.C. Keller. "Hard Tissue Replacements." *The Biomedical Engineering Handbook*. Ed. J.D. Bronzino. Boca Raton: CRC Press, 1995. p. 672-691.

17. Geesink, R.G., K. De Groot, and C.P. Klein. "Chemical Implant Fixation Using Hydroxyl-Apatite Coatings." *Clin Orthop* **225** (1987): 147-170.

18. Hench, L.L.. "Biomaterials." *Science*. Eds. P.H. Abelson and M. Dorfman. Vol. 208. Washington DC: America Association for the Advancement of Science, 1980.

19. Brown, S.R., I.G. Turner, H. Reiter. "Residual stress measurement in thermal sprayed hydroxyapatite coatings." *J Mater Sci Mater Med* 5 (1994): 756-759.

20. Charnley, J.. "Anchorage of Femoral Head Prosthesis to Shaft of Femur." *J Bone Joint Surg* **42B** (1960): 28-34.

21. Oka, M., Y.S. Chang, T. Nakamura, M. Kobayashi, and T. Kitsugi. " Bone Remodeling Around Implanted Ceramics." *Bioceramics* **8** (1995): 103-106.

22. Walenciak, M.T., M.C. Zimmerman, and r.D. Harten. "CPTI vs. HA coated Canine Hip Stems: A Biomechanical and Histological Study." *21st Annual Meeting, Society for Biomaterials*. San Francisco: 1995. p. 320.

23. Wolfarth, D., M. Filiaggi, and P. Ducheyne. "Parameters Analysis of Interfacial Stress Concentrations in Porous Coated Implants." *J Appl Biomed* **1** (1990): 3-12.

24. Dzidzic, M. and J.E. Davies. "Porous Coated Surfaces and Osteoconduction." *21st Annual Meeting, Society for Biomaterials*. San Francisco: 1995. p. 203.

25. Lord, G. and P. Bancel. " The Madreporic Cementless Total Hip Arthroplasty." *Clin Orthop* **176** (1983): 67-76.

26. Chen, P.Q., T.M. Turner, H. Ronnigen, J. Galante, R. Urban, W. Rostoker. "A Canine Cementless Total Hip Prosthesis Model." *Clin Orthop* **176** (1983): 24-33.

27. Morscher, E.W.. "Cementless Total Hip Arthroplasty." *Clin Orthop* **181** (1983): 76-91.

28. Ritter, M.A. and E.D. Campbell. "Direct Comparison Between Bilaterally Implanted Cemented and Uncemented Total Hip Replacements in Six Patients." *Clin Orthop* **207**(1986): 77-82.

29. Engh, C.A.. "Hip Arthroplasty with a Moore Prosthesis with Porous Coating." *Clin Orthop* **176** (1983): 52-66.

30. Brown, I.W. and P.A. Ring. "Osteolytic Changes in the Upper Femoral Shaft Following Porous-Coated Hip Replacement." *J Bone Joint Surg* **67-B** (1985): 218-221.

31. Bobyn, J.D., R.M. Pilliar, H.U. Cameron, and G.C. Weatherly. "The Optimum Pore Size for the Fixation of Porous-Surfaced Metal Implants by the Ingrowth of Bone." Clin Orthop **150** (1980): 263-270.

32. Bryan, W.J., B.L. McCaskill, and H.S. Tullos. "Hip Endoprothesis Stabilization with a Porous Low Modulus Stem Coating: Factors Influencing Stabilization." *Clin Orthop* **157** (1981): 125-132.

33. Shaw, J.H., S.M. Best, W. Bonfield. "Characterization and Mechanical Properties of Synthetic Porous Hydroxyapatite." *21st Annual Meeting, Society for Biomaterials*. San Francisco: 1995. p. 391.

34. Müller-Mai, C., H.J. Schmitz, V. Strunz, G. Fuhrmann, T. Fritz, U.M. Gross. "Tissues at the surface of the new composite material titanium/glass-ceramic for replacement of bone and teeth." *J Biomed Mater Res* **23** (1989): 1149-1168.

35. Hench, L.L. and J. Wilson. "Glasses in Medical Applications." *Encyclopedia of Materials Science and Engineering*. Ed. M.B. Bever. Vol. 3. New York: Pergamon Press, 1986. p. 2014-2019.

36. Ducheyne, P.. "Bioglass coatings and bioglass composites as implant materials." *J Biomed Mater Res* **19** (1985): 273-291.

37. Klein, C.P.A.T., J.G.C. Wolke, R.C. Vriesde, and J.M.A. De Blieck-Hogervorst. "Cortical bone ingrowth in grooved implants with calcium phosphate coatings: a gap model study." *J Mater Sci Mater Med* **5** (1994): 569-574.

38. Yang, C.Y., B.C. Wang, W.J. Chang, and E. Chang. "Mechanical and histological evaluations of cobalt-chromium alloy and hydroxyapatite plasma-sprayed coatings in bone." *J Mater Sci Mater Med* **7** (1996): 167-174.

39. Wolfarth, D. and P. Ducheyne. "Porous Coating Geometry and the Relationship to Fatigue Strength." *Fourth World Biomaterials Congress*. Berlin: 1992. p. 53.

40. Lenz, J., S. Schwartz, H. Schwickerath, f. Sperner, and A. Schäfer. "Bond Strength of Metal-Ceramic Systems in Three-Point Flexure Bond Test. "*J Appl Biomed* **6** (1995): 55-64.

41. Lenz, J., G. Franz, M. Kreitschik, K. Schulze-Luckow, and H. Wegner. "Der Torsionstest zur Bestimmung der Scher-Verbundfestigkeit von Metal and Keramik." *Phillip Journal* **1** (1990): 31-38.

42. Tam, L.E. and R.M. Pilliar. "Fracture Surface Characterization of Dentin-bonded Interfacial Fracture Toughness Specimens." *J Dent Res* 73. **3** (1994): 607-619.

43. Tam, L.E. and R.M. Pilliar. "Fracture Toughness of Dentin/Resin-composite Adhesive Interfaces." *J Dent Res* 72. **5** (1993): 953-959.

44. De Groot, R., H.C. Van Elst, M.C.R.B. Peter. "Fracture-mechanics Parameters of the Composite-Enamel Bond." *J Dent Res* 69. **1** (1990): 31-35.

45. Ritter Jr., J.E., D.C. Greenspan, R.A. Palmer, and L.L. Hench. "Use of Fracture Mechanics Theory in Lifetime Predictions for Alumina and Bioglass-Coated Alumina." *J Biomed Mate Res* **13** (1979): 251-263.

46. Kohn, D.H., C.C. Ko, and S.J. Hollister. "Global/Local Finite Element Analysis Of Porous Coated Total Hip Replacements." *Advances in Bioengineering* **26** (1993): 231-234.

47. Mann, K.A., F.W. Werner, and D.C. Ayers. "Modeling Tensile Failure At The Cement Bone Interface Using Non-Linear Fracture Mechanics." *42nd Annual Meeting, Orthopedic Research Society*. Atlanta: 1996. p. 519.

48. Guyton, A.C.. *Human Physiology and Mechanisms of Disease*. 5th ed. Philadelphia: W.B. Saunders Company, 1992.

49. Toni, A., B. Mcnamara, M. Viceconti, A. Sudanese, F. Baruffaldi, and A. Giuniti. "Bone remodelling after total hip arthroplasty." *J Mater Sci Mater Med* 7 (1996):149-152.

50. McDougall, I., P.J. Gregson, and J.C. Shelton. "Multiaxial Fatigue Testing of Medical Grade Titanium Alloy." *Fifth World Biomaterials Congress*. Toronto: 1996. p. 556.

51. Forrest, K.J., J.C. Shelton, and P.J. Gregson. "Fatigue Failure in a Plasma Sprayed Hydroxyapatite Coated Titanium Alloy." *Fifth World Biomaterials Congress*. Toronto: 1996. p. 324.

52. Filho, O.P., L.L. Hench, E.D. Zanotto, G. LaTorre. "Strength of Bioactive Glass-Ceramics in the System P_2O_5-Na_2O-CaO-SiO_2." Patent Pending. Gainesville: 1996.

53. Lapedes, D.N.. *Dictionary of Scientific and Technical Terms*. New York: McGraw-Hill Book Company, 1974.

54. Jones, J.T. and M.R. Berard, eds. *Ceramics Industrial Processing and Testing*. 1st ed. Ames: The Iowa State University Press, 1972.

55. Van Vlack, L.H.. *Physical Ceramics for Engineers*. Massachusetts: Addison-Wesley Publishing Company, Inc., 1964.

56. Bajpai, P.K. and W.G. Billotte. "Ceramic Biomaterials." *The Biomedical Engineering Handbook*. Ed. J.D. Bronzino. Boca Raton: CRC Press, 1995.

57. Storer, R.A.. dir. ed. "Standard Test Method for Dynamic Young's Modulus, Shear Modulus, and Poisson's Ratio for Advanced Ceramics by Sonic Resonance." *Annual Book of ASTM Standards* **15.02** (1991): 351-357.

58. Zienkiewicz, O.C.. *The Finite Element Method*. 3rd ed. New York: McGraw-Hill Company, 1977.

59. Daculsi, G. N. Passuti, S. Martin, C. Deudon, R.Z. Legeros, S. Raher. "Macroporous calcium phosphate ceramic for long bone surgery in humans and dogs. Clinical and histological study." *J Biomed Mater Res* **24** (1990): 379-396.

60. Gross, K.A. and C.C. Berndt. "*In Vitro* testing of plasma-sprayed hydroxyapatite coatings." *J Mater Sci Mater Med* **5** (1994): 219-224.

61. Liu, D.M., H.M. Chou, and J.D. Wu. "Plasma-sprayed hydroxyapatite coating: effect of different calcium phosphate ceramics." *J Mater Sci Mater Med* **5** (1994): 147-153.

62. Lugscheider, E., G. Berger, M. Knepper, R. Sicking, and A. Nyland. "Plasma Sprayed Coatings of Calcium Titanium Phosphate: A New Generation of Bioactive Coatings." *Bioceramics*. Ponte Vedra: Pergamon Press, 1995. p. 317-322.

63. Knowles, J.C., K. Gross, C.C. Berndt, and W. Bonfield. "Structural Changes Induced During Thermal Spraying of Hydroxyapatite. A Comparison of Three Different Spraying Methods." *Bioceramics*. Ponte Vedra: Pergamon Press, 1995. p. 311-316.

64. Ohgushi, H., M. Okumura, K. Inoue, S. Tamai, Y. Dohi, M. Murata, Y. Kubok. "Bone Induction on the Surface of Hydroxyapatite Ceramics." *Bioceramics*. Ponte Vedra: Pergamon Press, 1995. p. 61-67.

65. Spector, M., R. Prabhakar, A. Bignami, P.A. Lalor, J. Bearcroft, N. Beals, and G.H. Nancollas. "Early Bone-Bonding Response to Plasma-Sprayed Hydroxyapatite Coatings of Different Composition in the Canine." *21st Annual Meeting, Society for Biomaterials*. San Francisco: 1995. p. 122.

66. Soballe, K., E.S. Hansen, H. Brockstedt-Rasmussen, V.E. Hjortdal, G. Juhl, C.M. Pedersen, I. Hvid, and C. Bunger. " Gap healing enhanced by hydroxyapatite coating in dogs." *Clin Orthop* **272** (1991): 300-307.

67. Clark, A.. "Bioglass Implant Materials." *J Oral Implantology* **12** (1986): 477-484.

68. Hench, L.L. and J. Wilson. "Surface-Active Biomaterials." *Engineering Applications of Ceramic Materials*. Ed. M.M. Schwartz. Metals Park: American Society for Metals, 1984.

69. Heikkilä, J.T., K.T. Mattila, Ö.H. Andersson, J. Knuuti, A. Uli-Urpo, and A.J. Aho. "Behavior of Bioactive Glass in Human Bone." *Bioceramics*. Ponte Vedra: Pergamon Press, 1995. p. 35-40.

70. Hench, L.L., Ö.H. Andersson, and G. LaTorre. "The Kinetics of Bioactive Ceramics Part III: Surface Reactions for Bioactive Glasses Compared with an Inactive Glass." *Bioceramics*. London: Oxford Press, 1991. p. 155-162.

71. Weinstein, A., J.J. Klawitter, and S.D. Cook. "Implant-bone interface characteristics of bioglass dental implants." *J Biomed Mater Res* **14** (1980): 23-29.

72. Piotrowski, G., L.L. Hench, W.C. Allen, and G.J. Miller. "Mechanical Studies of the Bone Bioglass Interfacial Bond." *J Biomed Mater Res* **6** (1975): 47-61.

73. Glass, L.. *Plasma Spray Advantage*. ASP/CAM Biomedical, Dayton, 1994.

74. Wahlmann, U., M. Knepper, E. Lugscheider, and W. Wagner. "Spraying Conditions and Performance of Apatite-Coatings." *Fifth World Biomaterials Congress*. Toronto: 1996. p. 330.

75. Herman, H.. "Plasma-sprayed Coatings." *Sci Amer* (1988): 112-117.

76. Gross, K.A. and C.C. Berndt. "The Amorphous Phase in Plasma Sprayed Hydroxyapatite Coatings." *Bioceramics*. Ponte Vedra: Pergamon Press, 1995. p. 361-366.

77. Helsen, J.A., E. Schepers, J. Schrooten, and E. Brauns. "Histological Evaluation of Plasma Sprayed Bioactive Glass Coatings on Titanium." *Fifth World Biomaterials Congress*. Toronto: 1996. p. 51.

78. McPherson, R., N. Gane, T.J. Bastow. "Structural characterization of plasma-sprayed hydroxylapatite coatings." *J Mater Sci Mater Med* **6** (1995): 327-334.

79. Yang, C.Y., B.C. Wang, E. Chang, and J.D. Wu. "The influences of plasma spraying parameters on the characteristics of hydroxyapatite coatings: a quantitative study." *J Mater Sci Mater Med* **6** (1995): 249-257.

80. Campbell, A.A., G.L. Graff, G.E. Fryxell, L. Song, K.W. Sump, G.J.Miller, and D.L. Wheeler. "Bioactive and Porous Metal Calcium Phosphate Coatings for Improved Bone Regeneration." *Fifth World Biomaterials Congress*. Toronto: 1996. p. 629.

81. Benezra, V., L. Hoang, and L.W. Hobbs. "Ultrastructural and Immuno-histochemical Studies of the Early Response of Bone to HA-coated Ti-6Al-4V In Vitro." *Fifth World Biomaterials Congress*. Toronto: 1996. p. 69.

82. Filgueiras, M.R., G. LaTorre, and L.L. Hench. "Solution effects on the surface reactions of a bioactive glass." *J Biomed Mater Res* **27** (1993): 445-453.

83. Hench, L.L and G. LaTorre. "Reaction Kinetics of Bioactive Ceramics Part IV: Effect of Glass and Solution Composition." *Bioceramics*. Philadelphia: Pergamon Press, 1993. p. 67-74.

84. Greenspan, D.C., J.P. Zhong, and K.D. Lobel. "In-Vitro Hydroxyapatite Formation on Bioactive Glasses." *Fifth World Biomaterials Congress*. Toronto: 1996. p. 6.

85. Hench, L.L.. "Theory of Bioactive Glasses." *21st Annual Meeting, Society for Biomaterials*. San Francisco: 1995. p. 366.

86. Schwartz, Z. and B.D. Boyan. "Underlying Mechanisms at the Bone-Biomaterial Interface." *J Cellular Biochemistry* **56** (1994): 340-347.

87. Shors, E.C. and R.E. Homes. "Histometry of Human Biopsies Show Bone Ingrowth and Implant Biodegradation of Porous Hydroxyapatite." *40th Annual Meeting, Orthopedic Research Society*. New Orleans: 1994. p. 546.

88. Brink, M., S. Yli-Urpo, and A. Yli-Urpo. "The Resorption of a Bioactive Glass Implanted into a Rat Soft Tissue." *Fifth World Biomaterials Congress*. Toronto: 1996. p. 48.

89. Huebner, K.H., E.A. Thornton, and T.G. Byrom. *The Finite Element Method For Engineers*. 3rd ed. New York: A Wiley-Interscience Publication, 1995.

90. Zienkiewicz, O.C. and R.L. Taylor. *The Finite Element Method: Basic Formulation and Linear Problems*. 4th ed. Vol. 1. New York: McGraw-Hill Company, 1989.

91. Hinton, E. and D.R.J. Owen. *An Introduction to Finite Element Computations*. Swansea, UK: Pineridge Press Limited, 1979.

92. Anand, S.C., K.R. St.John, D.D. Moyle, and D.F. Williams. "Stress Distribution in Porous Surfaced Medullary Implants." *Annals Biomed Eng* **5** (1977): 410-420.

93. Fisher, D.W. and J.L. Murray. "Solid Modeling and Finite Element Analysis of the Proximal Tibia Using Computed Tomography Data." *Advances in Bioengineering* **26** (1993): 195-198.

94. Schwardt, J.D., T.E. Dufresne, G.J. Gross, and D.D. Cody. "Predicting Failure With Finite Element Models Of The Proximal Femur In Elderly Females And Younger." *J Bone and Mineral Res* **1**, 10 (1995): S377.

95. Norman, T.L., K. Hustosky, J.D. Blaha, and J. Anderson. "2D Axisymmetric Finite Element Analysis Of A Debonded Total Hip Stem With An Unsupported Distal Tip." *Advances in Bioengineering* **26** (1993): 243-246.

96. Matsushita, Y., M. Kitoh, K. Mizuta, H. Ikeda, and T. Suetsugu. "Two-dimensional FEM Analysis of Hydroxyapatite Implants: Diameter Effects on Stress Distribution." *J Oral Implantology* (1990): 6-11.

97. Rohlmann, A., U. Mossner, and G. Bergmann. "Finite-Element-Analysis and Experimental Investigation in a Femur with Hip Endoprosthesis." *J Biomechanics* **9**, 16 (1983): 727-742.

98. Evans, S.L. and P.J. Gregson. "Numerical optimization of the design of a coated, cementless hip prosthesis." *J Mater Sci Mater Med* **5** (1994): 507-510.

99. Arramon, Y.P, S.C. Cowin, and A.M. Sadegh. "Axisymmetric Computational Models of Bone Ingrowth in to a Cylindrical Orifice." *Advances in Bioengineering* **26** (1993): 149-152.

100. Jacobs, C.R., M.E. Levenston, G.S. Beaupré, J.C. Simo, and D.R. Carter. "Numerical Instabilities in Bone Remodeling Simulations: The Advantages of Node-Based Finite Element Approach." *J Biomechanics* **4**, 28 (1995): 449-459.

101. Tensi, H.M., S. Ortloff, H. Gese, H. Hooputra, H. Mayr, and E. Klotz. "Application of FEM to Improve the Design and Performance of Endoprostheses." *Computer Methods in Biomechanics and Biomedical Engineering. 2nd International Symposium*. Swansee: 1994. p. 56-67.

102. Ortloff, S., H.M. Tensi, H. Gese, and P. Stütz. "Deformation of the Human Pelvic During Walking by Means of 3D-FEM-Consequences for Pelvic-Reconstruction with Implants." *Computer Methods in Biomechanics and Biomedical Engineering. 2nd International Symposium*. Swansee: 1994. p. 100-109.

103. Goldstein, S.A.. "The Mechanical Properties of Trabecular Bone: Dependence On Anatomic Location And Function." *J Biomechanics* **11**, 20 (1987): 1055-1061.

104. Vaillancourt, H., R.M. Pilliar, and D. McCammond. "Finite Element Analysis of Crestal Bone Loss Around Porous-Coated Dental Implants." *J Appl Biomed* **6** (1995): 267-282.

105. Huiskes, R. and E.Y.S. Chao. "A Survey of Finite Element Analysis in Orthopedic Biomechanics: The First Decade." *Eng Fract Mech* **6**, 16 (1983): 385-409.

106. Keaveny, T.M. and D.L. Bartel. "Fundamental Load Transfer Patterns for Press-Fit, Surface-Treated Intramedullary Fixation Stems." *J Biomechanics* **9**, 27 (1994): 1147-1157.

107. Tensi, H.M., S. Ortloff, and H. Hooputra. "Festkörperphysikalische Möglichkeiten Und Grenzen Der Implantatverankerung." *Symposiums SHEP Spongiosa Hüftsystem*. 1993. p. 13.

108. Tensi, H.M., S. Ortloff, H. Gese, and H. Hooputra. "Überlegungen zur Optimierung von Gelenkimplantaten--Considerations on the Optimization of Joint Implants." *Biomedizinische Technik* **39** (1994): 227-234.

109. Pillar, R.M., H. Vaillancourt, D.C. McCammond, D.A. Deporter, and P.A. Watson. "Short Term (10w) Bone Remodeling Around Porous-Coated Dental Implants Experimental And Finite Element Analysis." *21st Annual Meeting. Society for Biomaterials*. San Francisco: 1995. p. 286.

110. Pereira, D.S., J.L. Ricci, D. Scott, R.S. Casar, W. Jaffe, M. Hawkins, Y.H. Oh, and H. Alexander. "Effects of macroroughness and Hydroxyapatite Coating on Osteointegration and Osteoconduction." *21st Annual Meeting, Society for Biomaterials*. San Francisco: 1995. p. 424.

111. Avallone, E.A. and T. Baumeister III. eds. *Mechanics of Materials. Mark's Standard Handbook for Mechanical Engineers*. 9th ed. New York: McGraw-Hill Book Company, 1987.

112. La Torre, G. Telephone Interview. 4 March 1996.

113. Storer, R.A.. dir. ed. "Standard Test Method for Transverse Rupture Strength of Cemented Carbides." *Annual Book of ASTM Standards* **02.05** (1990): 138-139.

114. Storer, R.A.. dir. ed. "Standard Test Methods for Tension Testing of Porous Metal Coatings." *Annual Book of ASTM Standards* **03.01** (1988): 434-436.

115. Storer, R.A.. dir. ed. "Standard Test Method for Adhesion or Cohesive Strength of Flame-Sprayed Coatings." *Annual Book of ASTM Standards* **02.05** (1979): 656-660.

116. Lemons, J.E.. "Keynote Address: Biomaterials for Total Joint Replacement. Biological, Material, And Mechanical Considerations of Joint Replacement." Ed. B.F. Morrey. New York: Raven Press, 1993. p. 13-21.

117. Yang, C.Y., B.C. Wang, E. Chang, and B.C. Wu. "Bond degradation at the plasma-sprayed HA coating/Ti-6Al-4V alloy interface: an *in vitro* study." *J Mater Sci Mater Med* **6** (1995): 258-265.

118. Filiaggi, M.J., N.A. Coombs, and R.M. Pilliar. "Characterization of the interface in the plasma-sprayed HA coating/Ti-6Al-4V implant system." *J Biomed Mater Res* **25** (1991): 1211-1229.

119. Helms, H.E. and S.R. Thrasher. "Ceramic Applications in Turbine Engines (CATE) Development Testing." *Engineering Applications of Ceramic Materials*. Ed. M.M. Schwartz. Metals Park: America Society for Metals, 1985. p. 25-31.

120. North, B.. "Substitution of Ceramics for Conventional Cutting Tools." *Engineering Applications of Ceramic Materials*. Ed. M.M. Schwartz. Metals Park: American Society for Metals, 1985. p. 154-166.

121. Hayakawa, S.. "Ceramics Fulfill Special Roles in Electronics Designs." *Engineering Application of Ceramic Materials*. Ed. M.M. Schwartz. Metals Park: America Society for Metals, 1985. p. 238-246.

122. Ding, S., L. Meekisho, and M. Kumosa. "Analysis of Stress Singular Fields at a Bimaterial Wedge Corner." *Engineering Fracture Mechanics* 49. **4** (1994): 569-585.

123. Scholl, M., P. Clayton, E. Elmore, J. Wooten. "Spray Forming By High Power High-Velocity Spraying." *Thermal Spray Coatings: Properties, Processes and Applications, Proceedings of the 4th National Spray Conf*. Ed. T.F. Berneki. Metals Park: ASM International, 1992. p. 281-288.

Biographical Sketch

Mia Park was born on November 13, 1971 in Houston, TX. She completed a Bachelor's Degree from the Engineering Science Department at the University of Florida on April 30, 1994. In September of 1994, she began attending the Oregon Graduate Institute of Science & Technology. Her major area of interest is the field of Biomaterials in orthopaedic applications.